# 3D Printing for the Development of Complex *In Vitro* Models to Investigate Nanoantibiotics against Bacterial Infections

Dissertation zur Erlangung des Grades des Doktors der Naturwissenschaften der Naturwissenschaftlich-Technischen Fakultät

der Universität des Saarlandes

von

**Samy Aliyazdi**

Saarbrücken 2024

Die dieser Dissertation zugrundeliegenden experimentellen Arbeiten wurden von April 2019 bis September 2023 unter der Leitung von Prof. Dr. Claus-Michael Lehr, zusätzlich unterstützt durch Prof. Dr. Thomas Vogt, Brigitta Loretz und Ulrich F. Schäfer, am Helmholtz-Institut für Pharmazeutische Forschung Saarland (HIPS) in der Abteilung Wirkstofftransport (DDEL) durchgeführt.

| | |
|---|---|
| Tag des Kolloquiums: | 31.01.2025 |
| Dekan: | Prof. Dr.-Ing. Dirk Bähre |
| Vorsitz: | Prof. Dr. Alexandra Kiemer |
| Betreuer (Gutachter 1): | Prof. Dr. Claus-Michael Lehr |
| Gutachter 2: | Prof. Dr. Marc Schneider |
| Gutachter 3: | Prof. Dr. Peter Loskill |
| Akademischer Mitarbeiter: | Dr. Jörg Haupenthal |
| Berichterstatter: | Sarah Frisch |

“Science is a self-correcting process. To be accepted, new ideas must survive the most rigorous standards of evidence and scrutiny.”

*Carl Sagan*

“Die Welt, wie wir sie geschaffen haben, ist ein Prozess unseres Denkens. Sie kann nicht verändert werden, ohne unser Denken zu ändern.”

*Albert Einstein*

These quotes from two eminent figures underscore the transformative power of science and the open-mindedness essential for progress. This dissertation introduces innovative human *in vitro* models designed to offer crucial alternatives to traditional animal models. By exemplifying the necessary evolution and advancement in infection research, these models aim to enhance the fight against chronic infections through novel anti-infectives tested on systems with reliable predictive capabilities.

# Table of Contents

## Summary

3D (Bio)printing is a cutting-edge technology offering precision in developing *in vitro* models. These models can serve as alternatives to animal experiments, particularly in infection research, where options are limited. By mimicking *in vivo* conditions, they can improve the predictability of drug efficacy for clinical applications.

This thesis explores 3D bioprinting to create innovative approaches in biomedical research. The primary goal was to develop a model of chronically infected lungs. Previous work involved an *in vitro* model of epithelial lung cells combined with *Pseudomonas aeruginosa* biofilms, revealing limitations of manual pipetting. 3D bioprinting was identified as a solution to position biofilms accurately on lung cell monolayers. *Escherichia coli* was chosen for its ease of handling, and a gelatin-alginate bioink was developed to support biofilm growth.

The second project applied 3D printing to hair follicle research. Initially aimed at studying hair loss, the model was adapted to investigate bacterial infections like acne inversa. Using 3D printing to create a collagen matrix, hair follicles were sustained in their growth phase, infected with *Staphylococcus aureus*, and treated with nanoantibiotics.

These approaches highlight the potential of 3D bioprinting. They reduce reliance on animal testing and accelerate the development of treatments for chronic infections, representing progress toward effective drug testing and clinical applications.

# Zusammenfassung

3D(Bio)printing ist eine innovative Technologie zur Entwicklung präziser *in vitro* Modelle, die Tierversuche in der Infektionsforschung ersetzen können, wo Alternativen begrenzt sind. Durch die Nachahmung von *in vivo* Bedingungen verbessert diese Methode die Vorhersagbarkeit der Arzneimittelwirksamkeit.

Diese Dissertation untersucht den Einsatz von 3D (Bio)printing für biomedizinische Forschungsansätze und die Entwicklung eines Modells für chronisch infizierte Lungen. Ein Vorläufermodell bestand aus epithelialen Lungenzellen und *Pseudomonas aeruginosa* Biofilmen und zeigte die Grenzen manueller Pipettierung. 3D Bioprinting erwies sich als geeignet, Biofilme präzise auf Lungenzell-Monolayer zu platzieren. *Escherichia coli* wurde aufgrund seiner einfachen Handhabung gewählt, und eine Gelatine-Alginat Biotinte wurde entwickelt, um das Biofilmwachstum zu fördern.

Das zweite Projekt befasste sich mit der Anwendung des 3D-Drucks auf die Haarfollikelforschung. Ursprünglich zur Untersuchung von Haarausfall entwickelt, wurde das Modell zur Erforschung bakterieller Infektionen wie Acne inversa angepasst. Mithilfe von 3D Druck und einer Kollagenmatrix konnten Haarfollikel in ihrer Wachstumsphase gehalten und mit *Staphylococcus aureus* infiziert werden.

Diese Ansätze zeigen das Potenzial des 3D (Bio)printings: Es reduziert die Abhängigkeit von Tierversuchen und beschleunigt die Entwicklung neuer Behandlungen für chronische Infektionen sowie die Arzneimittelprüfung und klinische Anwendungen.

## Introductory Remarks and Scientific Output

The data and concepts from the following two publications form the core of the subsequent cumulative thesis.

1. **Samy Aliyazdi**, Sarah Frisch, Alberto Hidalgo, Nicolas Frank, Daniel Krug, Rolf Müller, Ulrich F Schaefer, Thomas Vogt, Brigitta Loretz and Claus-Michael Lehr (2023): **3D bioprinting of *E. coli* MG1655 biofilms on human lung epithelial cells for building complex *in vitro* infection models**. In Biofabrication, Volume 15, Number 3.
   DOI 10.1088/1758-5090/acd95e
2. **Samy Aliyazdi,** Sarah Frisch, Tobias Neu, Barbara Veldung, Pankaj Karande, Ulrich F Schaefer, Brigitta Loretz, Thomas Vogt, Claus-Michael Lehr (2024)**. A Novel 3D Printed Model of Infected Human Hair Follicles to Demonstrate Targeted Delivery of Nanoantibiotics**. In ACS Biomaterials Science & Engineering; Volume 10, Issue 8; August 12, 2024 Pages 4645-5408.
   https://doi.org/10.1021/acsbiomaterials.4c00570

   Other publications research activity related to this thesis
3. Sarah Frisch, Samy Aliyazdi, Jacqueline Rehner, Georges Schmartz, Caroline Gevaerd, Lorenz Latta, Barbara Veldung, Sören Becker, Andreas Keller, Ulrich F Schäfer, Brigitta Loretz, Thomas Vogt, Claus Michael-Lehr. **Staphylococcal proliferation on skin models to investigate novel anti-infective treatments against dysbiosis in Acne inversa.** In submitting process in ACS Infectious Diseases (2024-2025).
4. Aghiad Bali *et al*., worked on follow up project of publication 1. Manuscript yet to be prepared (2025).

## Awards

1. Best elevator pitch award – Controlled Release Society (CRS) Germany Local Chapter 2021
2. Fan favorite poster award – CRS Virtual Annual Meeting 2021
3. Best flash talk award – CRS Germany Local Chapter 2022
4. Young investigator award – Microphysiological Systems (MPS) World Summit 2023

# 1. Introduction

## 1.1 3D (Bio)printing

### 1.1.1 Definition and application in biomedical research

The core technology and primary method utilized in this thesis is 3D printing, an additive manufacturing process developed in the 1980s that creates three-dimensional objects by layering materials. This versatile technology has found widespread applications across various industries, including aviation, geoscience, education, clothing, medical, and pharmaceuticals (*1*). 3D printing can be classified according to different layering methods and the selected materials and their physical state. Metal, ceramic, composite and polymeric materials can all be utilized in 3D printing (*2*). Various 3D printing methods are employed in the biomedical field, each tailored to specific applications and materials. Fused deposition modeling (FDM), for instance, uses thermoplastic filaments like Polylactid (PLA) or Polyetheretherketon (PEEK). In FDM, the filament is heated, melted, and extruded through a nozzle, which moves layer by layer to build the object. PLA is biocompatible and biodegradable, making it suitable for temporary medical models, while PEEK is known for its durability and is often used in permanent implants (*3*). Stereolithography, on the other hand, utilizes liquid photopolymers that are cured layer by layer using UV light, producing highly detailed structures. This method is frequently applied in dental applications, such as creating crowns, surgical guides, other prosthetic constructs, as well as in the fabrication of microfluidic devices for research purposes (*4, 2*). Another method is selective laser sintering, which uses a laser to sinter powdered materials, such as polymers like nylon and metals like titanium and cobalt-chromium alloys. This technique produces robust and precise implants, also commonly used in orthopedics and dentistry. (*5*). Within each of these methods, there are further classifications and variations, and the materials used can often be adapted or combined across different techniques, demonstrating the versatility and overlap of 3D printing technologies in biomedical applications.

A specialized application of 3D printing is 3D bioprinting[1], a revolutionary technique that enables the layer-by-layer deposition of bioinks, comprising biomaterials and living cells. This state-of-the-art technology facilitates the creation of three-

[1] For clarification, the term 3D (bio)printing with brackets is used when referring to 3D printing and bioprinting.

dimensional structures that closely mimic natural tissues and organs. There are several distinct bioprinting techniques, broadly categorized as droplet-based bioprinting, extrusion-based bioprinting, and laser-assisted bioprinting. Droplet-based bioprinting involves generating drops of low-viscosity materials using piezoelectric, thermal, or electrostatic forces to construct a spatially heterogeneous tissue structure (*6*). Extrusion-based bioprinting, on the other hand, utilizes pneumatic pistons or screw drive approaches to deposit continuous filaments of hydrogels. In photocuring-based bioprinting, a laser-assisted printing system incorporates a pulsed laser source, laser focusing tool, metallic ribbon film with an upper energy-absorbing layer, and a receiving substrate. During the printing process, the pulsed laser focuses on the upper layer, inducing film evaporation and the formation of a high-pressure bubble that propels suspended bioink onto the receiving substrate (*7*). To date, 3D (bio)printing has been successfully applied to fabricate a diverse array of tissues, organs, and disease models (*8*). These applications span a wide range, encompassing cardiac tissues (*9, 10*), liver tissues (*11, 12*), bone (*13, 14*), lung, skin, various cancer models, and beyond (*8*).

### 1.1.2 Application of 3D (bio)printing for *in vitro* models

The potential applications of 3D (bio)printing extend prominently to regenerative medicine, tissue engineering, and drug testing, as evidenced by its growing adoption in these fields (*15*). This versatile method has spurred increased interest in designing advanced 3D *in vitro* models, positioning itself as a bridge between traditional cell culture and *in vivo* modelling. Nowadays, such models led to an advanced understanding of pharmacological and toxicological processes of all kind of treatments and chemicals (*8*). Over the past decade, manual construction of 3D *in vitro* models using natural polymers (collagen, ECM, gelatin, polyacrylamide) and various natural and synthetic scaffolds has been a prevailing approach (*16*). However, these methods have been limited in their ability to create intricate architectures and exerting precise control over cell placement, thereby constraining their ability to simulate *in vivo* conditions accurately. 3D (bio)printing significantly increases the complexity of *in vitro* models, enabling the creation of structures that closely mimic tissues, organs, and diseases by incorporating heterogeneous cell populations, extracellular matrix components, and vascular networks (*17*). Moreover, the tailored microenvironment, supported by suitable bioinks and matrices, promotes

more natural cell-cell interactions, leading to a better replication of *in vivo* conditions (*18*). While it is difficult to provide an exact number of publications addressing 3D (bio)printing and *in vitro* models, the emergence of 3D (bio)printing, along with other advanced manufacturing techniques like electrospinning, has undoubtedly revolutionized the field. These technologies offer unprecedented control over model architecture by enabling precise placement of cells and biomaterials with high resolution and reproducibility, marking a new era in tissue engineering and model development (*16, 19*). Consequently, the development of all types of printed *in vitro*-, tissues and disease model rose tremendously in the past decade.

According to the world health organization cardiovascular diseases are the leading cause of death globally, taking an estimated 17.9 million lives each year (*20*). Hence, there is a great focus on *in vitro* models addressing this issue, designed to be applied for drug and toxin testing. To advance previous 2D or manually prepared 3D heart models/tissue and overcome a wide range of limitations, 3D bioprinting was a key application in the past decade. For instance, it was demonstrated that iPSC-CMs exhibit enhanced maturity and can more accurately mimic adult heart tissue during drug testing when bioprinted as small strands stretched between two pillars (*21*). Recently, milestones were achieved when 3D (bio)printing was utilized to design full heart and chamber models (*22, 9, 10*).

Recent advancements in 3D bioprinting have also improved liver *in vitro* models for drug screening and disease studies. Vascularized liver models with spatially organized hepatic and endothelial cells, as well as perfusion-enabled models with microchannels, are outcomes of this progress, demonstrating enhanced liver function and the expression of key liver markers (*12, 23*). Interestingly, Gori *et al.* (2020) demonstrated significantly increased sensitivity of the drug acetaminophen in 3D printed liver models than in 2D counterparts, suggesting that spatial organization might play a key role for drug screening (*24, 8*). Hiller *et al*. (2018) presented a platform of a bioprinted liver model, applied to study adeno-associated virus infection (*11*). These advancements have made bioprinted liver models increasingly valuable in the pharmaceutical industry, offering enhanced sensitivity in drug testing and effective platforms for viral research.

A key disease of great interest for *in vitro* modelling is cancer, still a significant global health issue. A wide range of different cancer types with different complexities were already designed for drug screening by (bio)printing, including brain, liver, lung, breast, colorectal, pancreas and ovarian cancer (*25*). Like other *in vitro* models, 2D and manually constructed 3D cancer models are limited by their inability to accurately emulate the disease's pathophysiology and by the reduced functionality of the cells (*26*). Specifically, they lack perfusable vasculature, pathological architecture, extracellular matrix environment (ECM) and multiple cell type inclusions. 3D (bio)printing, as previously described, can spatially pattern different cell types to more accurately mimic the *in vivo* microarchitecture (*25*). In combination with suitable bioinks, composed of ECM components and growth factors, this approach can further enhance cellular functionality and promote more physiologically relevant behaviour within the constructs. That microenvironment has a great impact on cells and the relevance of the model was shown again and again in different cancer model types, showing generally, more *in vivo* pathology via increased resistance towards chemotherapeutic agents, gene expression, altered drug reaction, cell proliferation and function (*27*). Although cancer is not the primary focus of this thesis, it is worth noting that with over 500 publications on cancer and 3D (bio)printing (*28*), this field holds significant potential for advancing pharmaceutical development, potentially leading to more effective and efficient therapies in the near future.

In the realm of lung *in vitro* models, Horvath *et al*. 2015, pioneered the bioprinting of an air-blood tissue barrier, utilizing a layer-by-layer approach to fabricate A549 alveolar epithelial cells and EA.hy926 endothelial cells, separated by a basement membrane mimic with Matrigel (*29*). This innovative method showcased the capability of 3D bioprinting to design thinner and more homogeneous cell layers, creating a closer mimic of the air-blood barrier. Recent advancements have extended to the bioprinting of 3D lung tissues for investigating viral infections such as Covid-19 or influenza A, aiming to portray a more natural infection profile, a limitation in conventional 2D models (*30, 31*). Compared to other tissues and organs however, the application of 3D (bio)printing is rather less investigated for the lung.

Over the past decade, 3D (bio)printing has made significant strides in the field of skin and cutaneous tissue. 3D printed skin grafts have been employed for various

applications, notably in wound healing and skin regeneration (*32*). 3D full-thickness skin equivalents (36, 6), extensively used for drug efficacy testing, involve multiple cell types (fibroblasts, keratinocytes) incorporated into bioinks composed of biomaterials such as collagen (*33, 34*), gelatin or fibrin (*35*). Synthetic materials have also been integrated to enhance these models. Kim *et al*. (2017) and Ramasamy *et al.* (2021) utilized a full-thickness collagen-based skin equivalent within a printed PCL mesh to mitigate the effects of collagen contraction, a phenomenon often induced by fibroblasts under air-liquid conditions (*36, 37*). Although 3D (bio)printing of skin models has seen significant advancements, several aspects remain underexplored. One such aspect is the inclusion of hair follicles, which play a critical role in the skin's function as a biological barrier. A notable effort to integrate hair follicles into 3D-printed skin constructs was made by Abaci *et al.* (2018). In their study, human dermal papilla cells (DPCs) were incorporated into a 3D-printed mold to form hair follicles within a skin construct, achieving physiological 3D organization for drug screening purposes (*38*). Similarly, Catarino *et al.* (2023) bioprinted DPCs and human umbilical vein endothelial cells within a pre-gelled dermal layer containing fibroblasts (*39*). However, challenges and limitations of such cultures, as well as a more detailed analysis of existing methods, will be discussed in section 2.1.2. As of now, no publication has reported a fully 3D-printed model of mature human hair follicles. The current approaches mainly involve traditional *in vitro* models, where isolated human hair follicles are maintained in suspension, as described in Chapter 2.

One area where 3D (bio)printing has yet to be extensively applied in research is the modelling of infections. However, bacteria have been 3D bioprinted before for various applications. A recent innovative approach involves the bioprinting of bacteria for diverse biotechnological and biomedical purposes, functioning as biofactories when embedded in specialized bioinks (*40, 41*). Another approach was the bioprinting of bacterial biofilms for antimicrobial testing within controlled and shaped models. Biofilms have been successfully printed using alginate-based bioinks. Spiesz *et al*. and Balasubramanian *et al*. bioprinted planktonic *E. coli* MG1655 in an alginate solution on $CaCl_2$-Luria-Bertani (LB)-agar plates, allowing them to incubate for 3–6 days to form a biofilm within the designated shape (*42, 43*). Additionally, Ning *et al*. bioprinted biofilms of *E. coli*, *S. aureus*, and *Pseudomonas aeruginosa* (*P.*

*aeruginosa*) for *in vitro* antimicrobial testing within a partially crosslinked alginate bioink, with biofilms forming within the printed construct after 5–14 days (*44*). Notably, in these approaches, biofilms were always formed post-printing. However, the integration of this concept with human cells to mimic an *in vitro* infection has not been explored thus far. The importance of this gap is discussed in more detail in the next chapter. Nevertheless, this represents an intriguing chance, taken in this thesis to offer the potential to create more realistic *in vitro* infection models by combining bacterial biofilms with human cells using advanced bioprinting techniques.

The ability of 3D (bio)printing to mimic the complexity of human tissues and diseases holds promise for advancing both basic research and translational applications in medicine and biology. Nevertheless, several key areas remain unexplored by traditional *in vitro* models, potentially could greatly benefit from this technology.

## 1.2 The importance of *in vitro* models

### 1.2.1 In the context of lung and lung infections

Bacterial biofilm associated infections are estimated to cause over half a million deaths each year in the US alone, including 171,000 respiratory cases, with a huge economic burden (*45, 46*). Bacterial biofilms are communities of bacteria, aggregating in a self-produced protective extracellular matrix, which consists of protein, polysaccharides and nucleic acids (*47*). In this state, bacteria can exhibit crucial antibiotic resistance due to penetration barrier or an altered chemical microenvironment (*48–51*). In patients suffering from cystic fibrosis, mucociliary clearance is impaired due to a mutation in the CFTR gen (*52*). These are optimal conditions for microbes to colonize the lung and cause chronic biofilm infections. *Pseudomonas aeruginosa* (PA) is the major pathogen, involved in such infections (*53, 54*). When the pathogens resist the therapy, lung destructive inflammation can occur, deteriorating the respiratory system (*55*). Considering the global medical challenge, novel and innovative anti-infective therapies are required. Taking this into account, every discovered active drug compound needs to be tested preclinically on robust and standardized models. Drug development is a time-extensive and costly process, especially the clinical studies. Recent estimates of costs are ranging from $314 million to $2.8 billion (*56*). Therefore, it is essential that novel drugs undergo preclinical studies to investigate efficacy and safety. Ultimately, preclinical studies aim to predict treatment/efficacy outcome and adverse effects (toxicity assessment)

in patients. To conduct preclinical studies, models mimicking the human physiology and disease mechanism are required. The gold-standard is still animal models, where rats, mice, cats and many more are infected intratracheally or intranasally with bacteria loaded agar beads to emulate the lung infection (*57, 58*). However, these approaches are questionable, because the bead embedded bacteria are not in contact with lung epithelium *in vivo*. Additionally, differences in genetics or immunology elucidate the issues in comparability to human pathology. To improve clinical translation and predictivity of drug efficacy *in vitro* alternatives, ideally with co-cultures of human epithelial cells and bacterial biofilms, are required. Although, such models exist, they are still limited in flexibility and cultivability.

A timeline, depicting the development of such *in vitro* models is shown in figure 1, beginning with biofilms growing on abiotic surfaces without host cells. Although such simple models allow for preliminary assessment of treatment efficacy, they seem to stay unable to reproduce the complexity found *in vivo* and lack any host cell response (*59*). A decade later, when biofilms in combination with host cells were approached, complex difficulties emerged. When PA was cultivated on epithelial lung cell layer, Anderson *et al.* showed rapid cell death within 4-6 h before a biofilm was even formed (*60*). Similar studies correlated the biofilm formation process with accelerated cell death (*61*). In a study from 2014, it was reported that *in vitro* lung cells are more prone to planktonic bacteria, compared to the cultivation with pre-established biofilms (*62*). The driving force of cell death seem to be the shear overgrowth process when bacteria are planktonic, while biofilm bacteria exhibit a reduced metabolism and growth (*63*). An approach to still establish such a culture with planktonic bacteria was to treat the infection promptly after infection with anti-infectives (*64*). However, still no chronic biofilm infection could be emulated by that approach. To overcome that, Juntke *et al.* and Horstmann *et al.* conducted these cultures with pre-established biofilms (*65, 66*). This was conducted by transferring (pipetted) separately grown biofilms onto human lung cell monolayers at air-liquid interface. With repeated antibiotic administration, the cultures were viable for 72 h. Although successful, a limitation of that approach is the lack of control of the deposited biofilms and the reproducibility. During the biofilm preparation process, biofilm mass is lost due to washing steps. Additionally, the transferring method via pipetting requires more standardization and flexibility to adapt the approach to any

requirements. In the context of this work, the promising technology of bioprinting and shaping biofilms were approached to overcome these challenges.

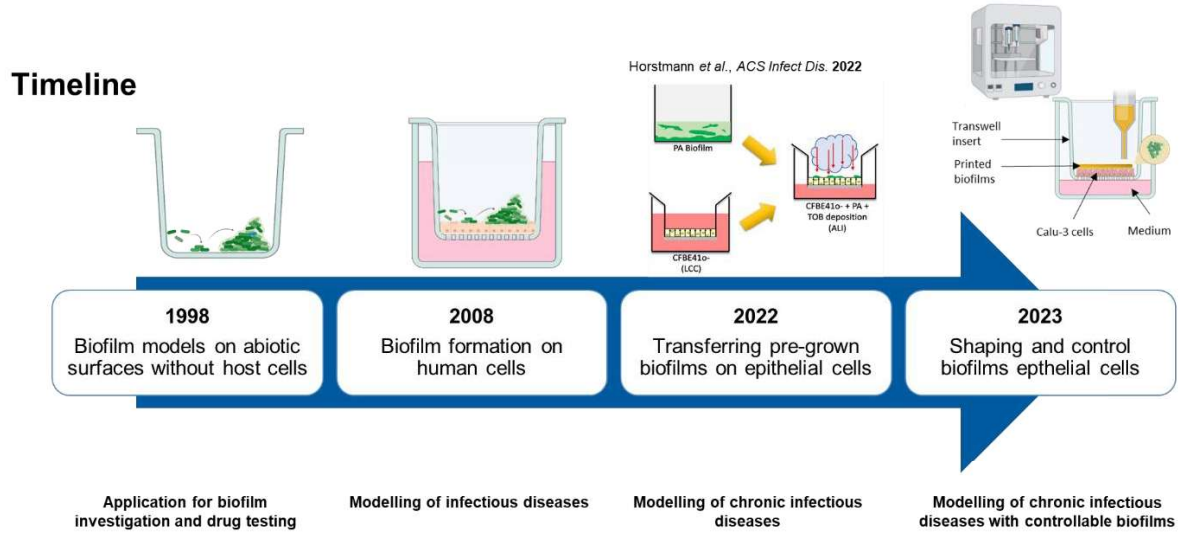


*Figure 1: Timeline of in vitro Biofilm models*

### 1.2.2 In the context of hair follicle infections

Beyond the respiratory system, hair follicles (HFs) are highly exposed to the external environment and potential pathogens. Globally, there have been over 200 million recorded incidences of bacterial skin diseases (*67*). Two examples of bacterial-related skin and HF diseases are acne inversa and folliculitis decalvans. Folliculitis decalvans, characterized by follicular pustules, manifests as an inflammatory scalp ailment with *Staphylococcus aureus* (*S. aureus*) playing a pivotal role in its pathogenesis (*68, 69*). Acne inversa, also known as hidradenitis suppurativa, is a painful inflammatory disorder typically found in regions like the axillary, genital, or inguinal areas (*70, 71*). The global prevalence varies significantly from 0.03-4%, likely influenced by geographical location and/or gender (*72*). Ongoing research seeks to unravel the precise role of bacteria and the microbiome in these diseases, with *S. aureus* appearing to be implicated alongside other microbes (*73*). Despite the clinical significance of these diseases (*74, 75*), our understanding of the mechanisms underlying treatment strategies remains incomplete. The primary goal often revolves around eliminating *S. aureus*, typically pursued through antibiotic administration, such as Rifampicin (*76, 77*). However, challenges like antibiotic resistance and the formation of biofilms by pathogens, such as *S. aureus*, have been linked to treatment failures and the development of chronic conditions (*78, 79*). Since the establishment that nanosystems in the submicrometer size range can penetrate and accumulate

within HFs (*80–83*), advanced nanocarriers have been a focus of research to effectively target these infections. Robust models are crucial to studying such anti-infective loaded nanocarriers against HF infections.

The *ex vivo* pig ear model stands as the prevailing method for studying nanoparticle uptake by HFs. For instance, Lademann *et al*. (2007) showcased the effective penetration of dye-loaded nanoparticles (320 nm) into the HF of pig ears (*84*). Another study by Raber *et al*. (2014) demonstrated the uptake of poly(D,L lactide-co-glycolide) (PLGA) nanoparticles into HF of pig ears (*85*). While the pig ear model effectively illustrates HF penetration due to its high similarity (*86*), it is a non-culturable tissue, limiting the assessment of biological efficacy and the study of tissue or immune responses over extended periods. Furthermore, interspecies differences may yield unique immune responses. An alternative *ex vivo* model involves human skin biopsies for studying nanocarrier penetration. In a study by Christmann *et al.* (2020), the penetration of PLGA nanoparticles (150 nm) into skin biopsies from human body donors, specifically targeting HF, was demonstrated (*87*). Investigations into diseases related to hair loss, such as alopecia areata, have been a focus in these studies. However, the challenge lies in the limited accessibility to intact HFs, hindering a comprehensive analysis of biological effects. Both models effectively illustrate HF penetration using dye-loaded nanocarriers but may not be optimal for testing the efficacy of drug-loaded systems. Additionally, these *ex vivo* models have yet to explore bacterial infections, as non-intact HFs may not elicit a reliable immune response. Nevertheless, the presence of a functional HF holds immense potential, offering opportunities to assess the follicle's condition in relation to various hair-related diseases.

The sole existing *in vitro* alternative comprises isolated HFs cultured in a liquid medium. In 1990, Philpott *et al.* introduced a HF organ culture system utilizing isolated human scalp skin, a model subsequently applied in studies pertaining to both hair growth and hair loss diseases (*88, 89*). A notable strength of this model lies in its capacity to explore biological effects over an extended period, spanning several days. However, its application for diverse purposes, such as nanoparticle treatment and bacterial infections, has not been thoroughly investigated. A limitation stems from the fact that HFs, naturally enveloped by a three-dimensional matrix *in vivo*, cannot be effectively exposed to topical nanocarrier formulations or bacteria in this

floating state. Recent methodologies have incorporated tissue engineering approaches, seeding dermal papilla cells within a 3D human skin construct to establish a more comprehensive HF model (*38*). While these advanced models better approximate *in vivo* conditions, they remain intricate, expensive, and time intensive. Despite these strides, the investigation of HF infection diseases still encounters challenges when approached either *ex vivo* or *in vitro*.

## 1.3 Nanoantibiotics

Nanosystems, characterized as particles within the size range of 1-100 nm, have undergone extensive exploration over the past decades across diverse applications (*90*). Situated at the intersection of chemistry, medicine, physics, and engineering, nanotechnology has found utility in a multitude of fields such as electronics, energy, materials science, the cosmetic industry, food industry, and biomedicine. In recent years, thorough investigations in biomedicine have explored nanoparticles derived from both natural and synthetic compounds, showcasing their potential as promising drug delivery systems. (*91*). The primary objective is to target drug delivery to specific sites of action, thereby enhancing bioavailability, optimizing biodistribution, and augmenting drug accumulation (*92*). This strategic use of nanoparticles not only improves therapeutic efficiency but also mitigates toxicity and minimizes side effects. Furthermore, nanoparticles offer protection to the drug against biological degradation, enabling temporal and spatial control of therapeutics (*93*). The diverse applications and physiological conditions necessitate various nanoparticle base compositions of inorganic, organic or carbon-based materials (Figure 2). Transition metals (Ag, Au, Pt, Zn etc), metal oxides NPs (ZnO,$TiO_2$, $Fe_3O_4$ etc), mesoporous silica NPs and quantum dots are examples for inorganic systems, while lipid-based NPs (e.g. liposomes) dendrimers, synthetic and natural polymers (polylactic-acid-co-glycolic acid (PLGA), polycaprolactone (PCL), chitosan, gelatin etc.) are assigned to organic materials (*94*). Carbon-based nanostructures are made of graphene and its derivatives. This dynamic range of nanoparticle formulations underscores their versatility in addressing specific needs across a spectrum of biomedical applications.

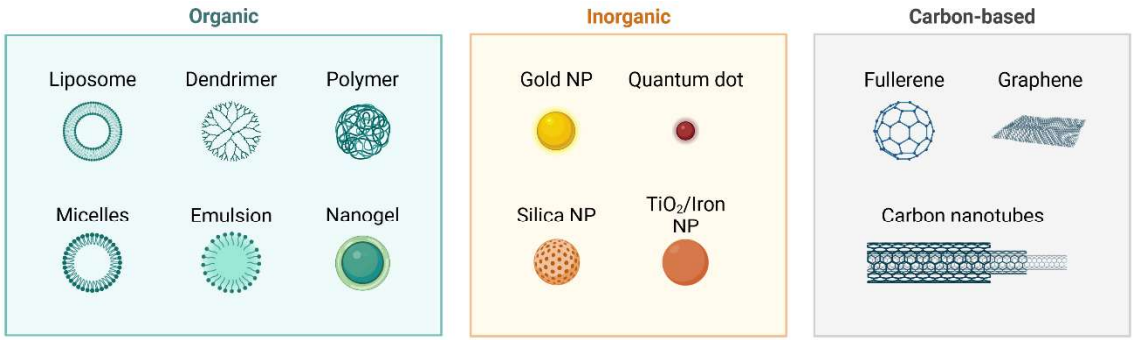


*Figure 2: Scheme of different types of nanoparticles. Created using www.biorender.com.*

In the context of combating bacterial infections, nanoparticles emerge as a promising tool for addressing several crucial aspects. Initially, the administration of antibiotics in their pure form faces multiple transport barriers, encompassing both human tissue and intra-bacterial obstacles. Notably, many bacterial infections are localized in specific tissues rather than the bloodstream, thereby restricting the effective dosage of antibiotics due to drug loss after systemic administration (*95*). Moreover, the presence of biofilms, as highlighted earlier, poses a significant impediment to antibiotic penetration, as numerous bacteria thrive within these structured communities. Additionally, reaching intracellular infections with antibiotics proves to be a formidable challenge (*96*). Secondly, bacteria manifest diverse antimicrobial resistance mechanisms, as discussed previously. These mechanisms include the capacity to impede the interaction of drug compounds with their intended sites of action through enzymatic modifications, hinder membrane penetration by reducing transporters, and express efflux pumps to expel antibiotics (*95*). These complexities underscore the imperative to explore innovative antibiotic delivery platforms that can surmount these challenges and enhance the therapeutic efficacy of antibiotics.

The unique properties of nanoparticles are an attractive tool either by exhibiting bactericidal effects by themselves or as carriers when packaged or tailored with antibiotics. A crucial aspect of nanomaterials is their high surface area to volume ratio, enabling diverse interactions with bacteria cells (*97*). Bactericidal nanomaterials exhibit antibacterial actions via a variety of mechanisms. One strategy is the disruption of the negatively charged bacterial cell wall and membrane with cationic nanomaterials. These NPs anchor to the bacterial surface via electrostatic interactions, causing loss of membrane integrity and cell lysis (*98*). Typical NP types used, are carbon-based NPs, metal-based NPs or polymeric NPs (*99*). Another

strategy is the generation or reactive oxygen species (ROS). ROS are byproducts of oxidative metabolic process causing lethal oxidative stress and cell damage when accumulated excessively (*100*). Specially metal-based NPs, like copper iodide NPs, AgNPs, AuNPs and other nanocomposites are associated with the generation of ROS and high antibacterial activity (*101*). Other bactericidal effects of nanomaterials include disruption of protein synthesis, DNA damage or gene regulation (*99*). As delivery systems, NPs can also be loaded with antibiotics. Aiming for improved therapeutic efficiency, antibiotic loaded NPs result in lower dosage requirements, enhanced stability, solubility, pharmacokinetics and barrier penetration (*98, 102, 103*). A crucial benefit is the targeted and sustained antibiotic delivery, preventing the bacteria to exposure of subinhibitory antibiotic concentrations/doses (*104*). These features are induced by the so called Trojan Horse effect which included the following aspects (*105*): Nanoscale drug delivery enhances efficacy by shielding antibiotics during cellular entry, reducing bacterial expulsion, and enabling selective release at infection sites. Lower doses of nano-enabled antibiotics are more effective due to differential release kinetics. Some polymeric nanoparticles biodegrade in infected cells, crossing membranes and selectively binding to infected components. Nanoparticles accumulate inside cells, trapping microbes and blocking bacterial entry into macrophages. Responsive nanoparticles can modulate based on factors like temperature or pH, activating multiple antimicrobial mechanisms.

In the context of bacteria biofilms, NPs appear to be a promising tool also. All kind of different nanosystems were already applied to fight bacterial biofilms. For instance, metallic NPs like AgNPs or AuNPs showed antibiofilm properties. AuNPs exhibited biofilm disruption or inhibition features in *S. aureus*, *P. aeruginosa*, *Escherichia coli (E. coli)* and many more biofilm forming strains (*106, 107*). This ability is apparently mediated by the binding of the particles to the surface of those bacteria, interfering the interactions between the pathogens during biofilm formation (*107*). Similarly, AgNPs showed antibiofilmic properties but also synergistic effects when combined with antibiotics (*108, 109*). As nanocarriers, NPs can facilitate the effective delivery of antibiotics trough the biofilms. Lipid-based NPs like liposomes loaded with anti-infectives can be cationic, facilitating the penetration of anionic biofilms. They also can be modified with molecules or antibodies, recognized by the biofilm, enhancing the targeting, interaction, and retention (*110, 111, 107*). Polymeric nanoparticles are

made of polymeric materials prepared via methods like nanoprecipitation, emulsion, or solvent evaporation. Loaded with antibiotics, they can mediate enhanced drug stability, solubility, bioavailability and sustained release (*112*). The choice of polymer and method are crucial for the shape, size and surface properties and eventually for the antimicrobial and antibiofilm activity (*113*). Common materials for polymeric NPs are PEG, chitosan and PLGA, which also exhibit antimicrobial and antibiofilm activity by themselves and in synergy with antibiotics (*114–116, 113*). Instead of encapsulation, antibiotics can also be covalently linked to polymeric carrier as polymer-drug conjugates. Accordingly, they can exhibit improved biofilm matrix penetration and sustained release of antibiotics as well as synergistic effects by their own antimicrobial potential (*117*). Other nanoparticle systems with similar antibiofilm activity are cyclodextrin-based NPs, dendrimer and solid lipid NPs (*118–120*). The ability to add surface modification of these nanomaterials by attaching molecules like antibodies, surfactants, polymers or peptides can additionally enhance their antimicrobial and antibiofilm potential as well as their stability, biocompatibility and delivery ability (*121*).

# 2. Aims of the thesis and essential results

At the outset of this thesis, I aimed to explore the promising possibilities of 3D (bio)printing for our application areas. For that purpose, a new 3D (bio)printer was purchased. Building on our lab's expertise in *in vitro* modelling for drug testing and development, limitations were identified in two key areas of research, which could potentially be addressed through the application of 3D (bio)printing technology.

## 2.1 Bioprinting of *E. coli* MG1655 biofilms on human lung epithelial cells

### 2.1.1 Aims

The story began with the recognition of an opportunity to overcome challenges and limitations of a previous work with the help of 3D bioprinting. Recently, our research group achieved a significant milestone by successfully cultivating *P. aeruginosa* biofilms atop human lung epithelial cell monolayers for an uninterrupted 72 hours (*66, 65*). Overcoming a longstanding challenge, where rapid overgrowth of bacteria led to the swift demise of host cells before biofilm formation, we devised a two-step process. Initially, the biofilm and host cells were cultured separately, and in the

subsequent step, the preformed biofilm was applied to the cells. While this approach, coupled with repeated antibiotic administration, enabled successful culture, we identified a drawback, where some biofilm was lost during washing steps prior to transfer. This, combined with the rheological nature of biofilms, influenced the control and reproducibility of both the transfer step and the overall culture process.

In a bid to enhance control and reproducibility, the innovative idea of bioprinting biofilms directly onto the cells emerged. While bioprinting of bacteria had been reported in literature for various applications, our unique challenge required a departure from existing methods. Previous studies, such as the work by Ning *et al. (122)*, involved printing planktonic bacteria in alginate bioink, forming biofilm post-printing. However, this approach was unsuitable for our application due to the inability to transfer intricately printed shapes onto cells and stability issues over time. Consequently, we opted to combine the bioprinting method with our previous achieved approach.

My objective was to bioprint a preformed biofilm onto human epithelial lung cells. Further, the hypothesis was, that bioprinted biofilms, still exhibit biofilmic properties post-printing process. *E. coli* MG1655 was selected as the strain, given its biofilm-forming capability and ease of handling. To make the biofilm printable, rheopromotive polymers were required. After a year of research, a gelatin-alginate hydrogel was identified as the optimal bioink base. It was hypothesized that with optimal bioprinting parameters, the biofilm properties could be retained post-printing and be shaped stable onto human lung epithelial cells. After consequent adjusting bioprinting parameters, this was demonstrated successfully. To showcase the feasibility of the concept, I bioprinted the biofilm onto human bronchial epithelial cells (Calu-3).

### 2.1.2 Essential results

Starting from scratch, I optimized a gelatin-alginate bioink, experimenting with different ratios to achieve ideal printability with minimal extrusion pressure. By combining rheological analysis with practical printability tests using a 3D (bio-)printer, a bioink composition of 3% gelatin and 1% alginate was identified as ideal for supporting *E. coli* MG1655 biofilms. Confocal microscopy and antibiotic susceptibility assays confirmed that printed biofilms retained essential biofilm characteristics. Using a live/dead stain kit, printed *E. coli* biofilms exhibited characteristic biofilm

morphology when compared to planktonic controls. Antibiotic susceptibility testing showed a high similarity in response between printed biofilms and native biofilms grown in well plates, as did metabolic profiling.

With the printed biofilm properties validated, I took the next step: printing *E. coli* MG1655 biofilms directly onto Calu-3 cell monolayers., with one set crosslinked and the other was left non-crosslinked. After 24 hours, an LDH assay indicated that neither setup caused cytotoxicity, and confocal microscopy revealed direct contact between the biofilms and Calu-3 cells. The crosslinked biofilms retained their shape at 37°C after 24 h, while even the non-crosslinked biofilms held their bacterial form, despite the bioink hydrogel dissolved.

Published in the journal Biofabrication, these findings constitute the initial research contribution to this thesis and is included in chapter 4.1.

## 2.2 A 3D-printed human hair follicle model

### 2.2.1 Aims

While the first goal was on progress, we were looking for more applications and ideas for our 3D (bio)printer. The second project of this work arose from an idea in the course of Alopecia Areata research from a colleague. Previously, the goal was to develop a 3D model with living, anagen, upright hair follicles to test topical nanoparticle delivery. Inspired by this idea, the aim became to adapt this approach for infection research. As described before, HF infections are a critical health issue and so far, not addressed by *in vitro* models. Primarily, the goal was to build such a model with viable, anagen human HFs. Preliminary we tried to culture human isolated HFs, inserted simply into a collagen matrix inside a transwell system. As it turned, the HFs die rapidly with this approach, supposedly due to insufficient nutrition supply. Inspired by the idea of such a model, I hypothesized that creating channel structures via 3D printing, could overcome this issue.

Living human HFs were transplanted into a collagen matrix within a 3D printed polymer scaffold to replicate the follicle's microenvironment. Hair growth kinetics over seven days confirmed viability inside the collagen matrix. To demonstrate the model's suitability for nanoparticle testing, it was hypothesized that nanoparticles of 200 nm size enter the follicular cleft when applied on top of the model. This was confirmed to some extent. Building on this success, I was eager to take the next step

and set a second goal, focusing on HF infections, which remain my primary area of interest.

The objective was to infect the created model with a bacterial pathogen to mimic a HF infection like in acne inversa or folliculitis decalvans. Then the infection was supposed to be treated with a nanoantibiotic as a proof of concept. I hypothesized, that the nanoantibiotic may penetrate bacteria within the follicular cleft more effectively than free the drug. *S. aureus* was selected to infect the 3D model as well as the traditional floating culture as control, because the strain is a common pathogen in such hair follicle infections. To treat the infection, rifampicin-loaded lipid nanocapsules were selected, because lipid-based nanosystems have already shown promising outcomes for follicle-targeted drug delivery applications on *ex vivo* human and porcine skin (*123–125*).

### 2.2.2 Essential results

After developing a reliable isolation method, I successfully transplanted hair follicles (HFs) into the 3D collagen construct. Within just seven days, the HFs in this model grew over 1 mm, closely mimicking the growth observed in traditional floating cultures in well plates. Given the hypothesis that nanoparticles sized at 200 nm could penetrate the HF openings, FluoSpheres® of this size were introduced onto the 3D model as well as into conventional floating cultures. Fluorescence imaging confirmed that in the 3D model, particles indeed entered the HFs, accumulating at the tip, whereas in floating cultures, they tended to cluster around the follicle structures.

With the HFs remaining viable in this system, I proceeded to the next step: establishing a controlled HF infection. My colleague Sarah Frisch was responsible for all bacterial handling, including the necessary CFU determinations and conducting the cytokine measurements. The HFs were drop-infected with *S. aureus* (NEWMAN GFP), and confocal microscopy revealed that the bacteria colonized both the outer HF surfaces and the follicle openings. To assess the HF response to this infection, I measured cytokine release using a cytometric bead assay and compared infected models with healthy, non-infected controls. After 24 hours, levels of interleukins 6 and 8 were significantly higher in infected models, indicating a strong immune response.

Encouraged by these results, I then moved to treat the infection with lipid nanocarriers (LNCs) loaded with rifampicin. Using micromixing, rifampicin-loaded LNCs were prepared, achieving a size of 142.4 ± 3.4 nm and a polydispersity index of 0.13 ± 0.02. After thorough characterization, these LNCs were applied to the infected 3D HF model and to floating cultures, and their effectiveness was compared to that of free rifampicin. While both treatments showed similar efficacy in floating cultures, only the nanoencapsulated rifampicin achieved a significantly greater reduction in bacterial count (CFU/mL) in the 3D HF model.

This pioneering work, published in ACS Biomaterials Science and Engineering, represents the second key research contribution of this thesis, and is included in chapter 4.2.

## 3. Discussion and Impact

The publication by Noor *et al.*, where vascularized heart tissue was created through 3D bioprinting (*9*), demonstrates the aspirations of this technology regarding drug testing and organ transplantation. While it is possible to create structures that are anatomically very similar to those *in vivo*, there is still a lack of reproduction of the necessary physiological complexity observed in humans. Thus, an appropriate clinical translation will likely take a considerable amount of time. However, as shown in this thesis, 3D biofabrication technologies can already complement and support limited *in vitro* models. It improves the development process and offers more accurate predictions about the effectiveness of new therapeutics. When we look at my first project, we realised that culturing human lungs cells and bacterial biofilms together is not trivial. However, we showed how the technology of 3D bioprinting can be used to overcome existing limitations of our previously published infectious lung *in vitro* model (*66*). Ideally, we want to mimic the *in vivo* disease environment closer with every step. Unlike animal models, our approach places biofilms in direct contact with the epithelium, more closely mimicking *in vivo* pathology compared to bacteria encapsulated in alginate, as used in previous described animal studies. Bioprinting mature preformed bacterial biofilms was the key premise for this achievement, demonstrated here for the first time. The hypothesis that the biofilm properties would be retained after printing was feasible when we designed a bioink composed of gelatin and alginate, optimized to extrude filaments at minimal pressure while

remaining printable. This was confirmed by confocal microscopy as well as antibiotic susceptibility assays. After printing the biofilm on human bronchial epithelial cells (Calu-3) the formulated objective was successfully achieved. The shape of the printed biofilms was stabilized by crosslinking with $CaCl_2$ and remained intact even after the dissolution of non-crosslinked bioink, with no cytotoxicity observed over 24 hours. An observation, which could be highly beneficial when shaping the pure biofilm is required.

This groundbreaking study represents the first instance, to our knowledge, of bioprinting preformed biofilms directly onto human cells. Importantly, the results represent a significant milestone in using such models to predict the effectiveness of new anti-infective agents against chronic biofilm infections. My approach holds the potential to serve as a platform for constructing intricate *in vitro* chronic infection models, incorporating both bacterial biofilms and human host cells.

I am especially proud to highlight the impact of this thesis progress towards clinical translation. The reason why animal models are still the gold standard, is due to the lack of reliable *in vitro* models. We showed how the technology of 3D bioprinting can overcome limitations of *in vitro* models hindering them to take the step towards clinics. Reproducibility, standardization, precision and flexibility are key features required for that step and can get achieved by 3D bioprinting. Nevertheless, further work is needed, as the approach described here must be applied to other strains, like *P. aeruginosa* that are clinically relevant for cystic fibrosis. This work was already initiated by my colleague Aghiad Bali (manuscript yet to be prepared) and was based on the contribution of this project. A last key step is a complete entirely characterized model, preferably cultured for many days or weeks like in *in vivo* chronic infections to monitor the disease process after a treatment. Such model must be tested rigorously for known and novel anti-infectives to evaluate its full prediction capability.

Similarly, our second project was inspired by the observation of prior model limitations, where we saw opportunities for 3D printing technology. Traditional HF models, which have primarily been used to study hair growth disorders or to test nanoparticle penetration exhibited decisive limitations, described before. While skin biopsies of animals do not allow any HF growth experiments nor drug efficacy evaluation, the floating isolated human HF organ culture do not allow topical particle

testing due to unreliable microenvironments. With these given limitations, HF infections were also never a part of *ex vivo* or *in vitro* investigations. By using 3D printing we were able to combine advantages of different traditional models and overcome some of the prior limitations. For the first time isolated human HFs were kept viable inside a 3D matrix, allowing topical drug administration. Over seven days, follicle growth resemble those of traditional simple floating cultures (used for comparison), growing more than 1 mm in that time. When fluorescent nanoparticles of 200 nm were applied on top of the model, follicular transport was observed to some extent, which was not the case for the floating cultures. Additionally, we designed an infection model for anti-infective drug testing, which was never addressed before. While rifampicin-loaded lipid nanocapsules were as effective as free rifampicin in floating cultures, only nanoencapsulated rifampicin achieved the higher reduction of CFU/mL in the 3D model. This finding underscores the critical role of the HF microenvironment in limiting the efficacy of conventional antibiotic treatments.

Once again, I am proud to emphasize the importance of these results, which will set significant developments in motion. Since such an approach was so far not described, this study could serve as platform to initiate conducting urgently required nanoantibiotic testing for HF infections. Additionally, the non-infected model could also be used for other fields like hair growth diseases or cosmetic applications. Nonetheless, further work is required to make these approaches more robust, ensuring their broader applicability and effectiveness. For instance, adding an epidermal layer on top of the collagen matrix could make the model more physiological, as well as incorporating other cell types (fibroblasts, keratinocytes, immune cells). Automatizing and increase precision of HF insert could highly improve the standardization and robustness of the model. A remaining limitation of the approach is the isolated method of the HFs, where upper part of the HF opening must be removed in order to access it. As this upper region of the opening is also an important part of the follicular cleft and thus for nanoparticle accumulation/penetration, new innovative techniques are required to remove the entire follicle.

Evaluating the overall impact of this thesis, I could underscore that we significantly contributed to set a new state-of-the-art of how 3D (bio)printing can be applied to

advance *in vitro* models. In the realm of 3D (bio)printing great progress was made in the last decade for man tissue engineering and *in vitro* models. However, infection *in vitro* models are a field with high potential for this technology, so far not in the spotlight of research. In the era of the silent pandemic however, facing antibiotic resistances and chronic biofilm infections, this focus on infection model is crucial to predict the efficacy of innovative anti-invectives. Our contribution paves the way essentially closer to reliable infectious lung and HF *in vitro* models.

In addition to the two publications, the scientific content of this thesis is already linked to two additional projects, with publications currently in preparation. Firstly, as previously mentioned, Aghiad Bali *et al.* built on the contributions of this thesis to adapt the bioprinting approach for *P. aeruginosa* biofilms. This could mark another milestone in advancing the concept, bringing us closer to a clinically relevant model for chronic infections in cystic fibrosis and providing a robust platform for testing anti-infective treatments against biofilm infections. Secondly, Sarah Frisch *et al.* utilized a similar gelatin-alginate base from this thesis as a substrate to cultivate bacterial pathogens, aiming to investigate the influence of dysbiosis related to acne inversa. During that collaboration the hydrogel/substrate was also 3D printed to achieve optimal thickness, making the application of imaging methods feasible. This approach is another example of the unlimited 3D (bio)printing possibilities. Furthermore, the findings of this thesis were presented at several prestigious conferences, where they garnered multiple awards. Among these, I am especially proud on the Young Investigator Award at the MPS World Summit in 2023.

To keep improving such *in vitro* models faster with greater validity, more research, dedication and funding are required. This was demonstrated once via the EC regulation 1223/2009 on cosmetics initiated by the European union. Guided by such an ethical consideration, the cosmetic industry has developed *in vitro* assays, which nowadays are accepted for safety and toxicity predictions of cosmetic products (*126*). Great advances were achieved for skin *in vitro* models in the past decade with increasing complexity for all kind of applications (*127*). This status is not achieved yet *in vitro* modelling of other organs and diseases. Recently, the FDA Modernization Act 2.0 was signed by President Biden, permitting the usage of *in vitro* assays for drug testing during preclinical phases. However, it is questionable whether this act will have the required drive to initiate significant investments into novel models.

# 4. Original Publications

## 4.1 3D bioprinting of *E. coli* MG1655 biofilms on human lung epithelial cells for building complex *in vitro* infection models

**Samy Aliyazdi**, Sarah Frisch, Alberto Hidalgo, Nicolas Frank, Daniel Krug, Rolf Müller, Ulrich F Schaefer, Thomas Vogt, Brigitta Loretz and Claus-Michael Lehr

Published 6 June 2023 • © 2023 The Author(s). Published by IOP Publishing Ltd

Biofabrication, Volume 15, Number 3

DOI 10.1088/1758-5090/acd95e

**Author contributions**

Conceptualization, S A, A H, B L and C-M L; Data curation, S A, S F, and N F; Supervision, A H, U F S, T V, B L and C-M L; Writing original Draft, S A; Writing-review and editing, S A, A H, S F, N F, D K, R M, U F S, T V, B L, and C-M L.

Biofabrication

PAPER

# 3D bioprinting of *E. coli* MG1655 biofilms on human lung epithelial cells for building complex *in vitro* infection models

Samy Aliyazdi[1,3], Sarah Frisch[1,3], Alberto Hidalgo[1,4], Nicolas Frank[2], Daniel Krug[2,3], Rolf Müller[2,3], Ulrich F Schaefer[3], Thomas Vogt[5], Brigitta Loretz[1,3] and Claus-Michael Lehr[1,3,*]

[1] Department of Drug Delivery, Helmholtz Center for Infection Research, Helmholtz-Institute for Pharmaceutical Research Saarland, Campus E8 1, 66123 Saarbrücken, Germany
[2] Department of Microbial Natural Products, Helmholtz Center for Infection Research, Helmholtz-Institute for Pharmaceutical Research Saarland, Campus E8 1, 66123 Saarbrücken, Germany
[3] Saarland University, 66123 Saarbrücken, Germany
[4] Charite-Universitätsmedizin Berlin, Institute of Functional Anatomy, Philippstraße 12, 10115 Berlin, Germany
[5] University Clinic Homburg, Clinic for Dermatology, Kirrberger Str., 66424 Homburg, Germany
[*] Author to whom any correspondence should be addressed.

**E-mail:** claus-michael.lehr@helmholtz-hips.de

**Keywords:** 3D printing, hydrogel, antimicrobial resistance, alternatives to animal experiments, chronic lung infections

Supplementary material for this article is available online

OPEN ACCESS

RECEIVED
18 January 2023

REVISED
25 April 2023

ACCEPTED FOR PUBLICATION
26 May 2023

PUBLISHED
6 June 2023



## Abstract

Biofilm-associated infections are causing over half a million deaths each year, raising the requirement for innovative therapeutic approaches. For developing novel therapeutics against bacterial biofilm infections, complex *in vitro* models that allow to study drug effects on both pathogens and host cells as well as their interaction under controlled, physiologically relevant conditions appear as highly desirable. Nonetheless, building such models is quite challenging because (1) rapid bacterial growth and release of virulence factors may lead to premature host cell death and (2) maintaining the biofilm status under suitable co-culture requires a highly controlled environment. To approach that problem, we chose 3D bioprinting. However, printing living bacterial biofilms in defined shapes on human cell models, requires bioinks with very specific properties. Hence, this work aims to develop a 3D bioprinting biofilm method to build robust *in vitro* infection models. Based on rheology, printability and bacterial growth, a bioink containing 3% gelatin and 1% alginate in Luria-Bertani-medium was found optimal for *Escherichia coli* MG1655 biofilms. Biofilm properties were maintained after printing, as shown visually via microscopy techniques as well as in antibiotic susceptibility assays. Metabolic profile analysis of bioprinted biofilms showed high similarity to native biofilms. After printing on human bronchial epithelial cells (Calu-3), the shape of printed biofilms was maintained even after dissolution of non-crosslinked bioink, while no cytotoxicity was observed over 24 h. Therefore, the approach presented here may provide a platform for building complex *in vitro* infection models comprising bacterial biofilms and human host cells.

## 1. Introduction

It is estimated that biofilm associated infections are causing half a million deaths each year in the US alone, with an economic burden of annually $94 billion [1, 2]. This raises the requirement for novel therapeutic approaches against biofilm infections. Bacterial biofilms are populations of bacteria that live in self-produced protective extracellular matrices (ECMs) composed of proteins, polysaccharides and nucleic acids [3]. The ability of many bacteria to produce biofilms is associated with chronic infections and antibiotic resistance, thus causing a serious health burden via a variety of mechanisms [4–6]. Key aspects include the creation of a penetration barrier against many antibiotic molecules, an altered chemical microenvironment or subpopulation of microorganisms, leading to therapy failures [4, 7]. Biofilms can form on many different surfaces and tissues [8]. For example, biofilm related lung infection, mediated

by *Pseudomonas aeruginosa* (*P. aeruginosa*) in patients suffering from cystic fibrosis, is one of the most common associated diseases [9, 10]. There, the pathogen forms biofilms on lung epithelium due to impaired mucociliary clearance [10].

The discovery of novel anti-infective compounds as well as their subsequent preclinical development requires robust biofilm models for fast testing purposes. The gold-standard approach is still animal models, including rats, mice, cats and many more, which are infected intratracheally or intranasally with bacteria loaded agar-beads [11]. However, interspecies differences in anatomy, genetics and immunology show suboptimal properties of animal models with human pathogenic bacteria in representation of comparable pathology. *In vitro* alternatives, ideally with co-cultures of human epithelial cells and bacterial biofilms, exist but are still limited in flexibility and cultivability.

Anderson *et al* attempted to cultivate *P. aeruginosa* biofilms on epithelial lung cells. However, the cells died rapidly during the biofilm formation process after 4–6 h [12]. Similar observations were made by Woodworth *et al*, who associated accelerated cell death with biofilm production [13]. Another study indicated that human *in vitro* cell systems were more prone to rapid cell death in the presence of planktonic bacteria due to massive overgrowth, than in the presence of a pre-established biofilm with reduced metabolism [14]. Montefusco-Pereira *et al* established a model with planktonic bacteria for anti-infective testing, which was treated 1 h after cell infection to prevent prompt cell death [15]. More recent approaches, such as those by Horstmann *et al* and Juntke *et al* involved transferring separately pre-grown biofilms onto human cell monolayers [16, 17]. By administering antibiotics repeatedly, such mixed cultures of bacteria and human cells could remain viable for 72 h under air–liquid conditions.

However, a major drawback of the aforementioned approaches is the poor control of the transferred biofilms.

A method to shape and transfer biofilms in a controllable manner could be the emerging technology of 3D bioprinting, a technique to fabricate and shape living materials like cells inside of hydrogels. This led to innovations in tissue engineering and regenerative medicine. Bone tissue [18], cardiac tissue [19, 20], liver tissue [21], skin tissue [22] and many other tissues [23] were already bioprinted successfully. Recently, the approach was applied to bioprint also living bacteria for different biotechnological and biomedical purposes [24, 25], including fabrication of bacterial biofilms. Spiesz *et al* and Balasubramanian *et al* bioprinted planktonic *Escherichia coli MG1655* (*E. coli MG1655*) in an alginate solution on $CaCl_2$-Luria-Bertani (LB)-agar plates, which were incubated for 3–6 d to form a biofilm within the shape [26, 27]. Similarly, Ning *et al* bioprinted *E. coli, Staphylococcus aureus* (*S. aureus*) and *P. aeruginosa* biofilms for antimicrobial testing. They mixed the planktonic bacteria with partially crosslinked alginate and printed them on plastic surfaces. The biofilm was then formed within the printed construct after 5–14 d, depicted via fluorescence imaging [28]. However, their approach would not be suitable to print bacterial biofilms on human epithelial cells, e.g. to mimic a biofilm related infection model, because if printed on cells directly, the biofilms are not formed yet and the transfer of the 5–14 d old crosslinked constructs are not optimal for any fine shapes.

In this work, we demonstrate a novel method to print biofilms, using *E. coli* as a model strain. For that, we tested and characterized gelatin-alginate hydrogels with different polymer concentrations to find the optimal bioink base for printing bacteria on epithelial cells. For this purpose, biofilms were firstly grown in the selected hydrogels and subsequently printed in different shapes. To assure that biofilm properties are maintained after bioprinting antibiotic susceptibility assays, metabolic profile analysis and microscopy techniques were performed and compared to native biofilms and planktonic bacteria. To check cell biocompatibility and whether biofilms can be shaped on human *in vitro* systems, biofilms were printed on top of confluent human bronchial epithelial (Calu-3) cell monolayers.

## 2. Material and methods

### 2.1. Bacterial and human cell culture

*E. coli* MG1655 was selected as a model strain, due to its ability to form biofilms and its ease of culturing as a S1 strain. *E. coli* MG1655 was cultured on LB-agar plates, streaked from frozen glycerol stocks. An overnight (O/N) culture was initiated by inoculating a single colony into an Erlenmeyer flask containing 25 ml LB-medium (Sigma-Aldrich, Germany) and incubating it shaking (180 rpm) at 37 °C.

Calu-3 cells (HTB-55, ATCC, LGC Germany) were chosen as an epithelium lung cell model. They were cultured in minimum essesntial medium (Gibco, UK) in cell culture flasks (Greiner, Germany), supplemented with 10% fetal bovine serum (Gibco, UK), 1% sodium pyruvate (Gibco, USA) and 1% Non-Essential Amino Acids (NEAA, Gibco, UK). Cells were kept at 37 °C at 5% $CO_2$ and medium was exchanged every 2–3 d. Passaging was performed once per week.

### 2.2. Bioink preparation

Gelatin (Bloom 300, Type A, Sigma-Aldrich, Germany) and sodium alginate (W202503, Sigma-Aldrich, Germany) were weighed at different concentrations in 12 ml of LB medium and stirred at 60 °C–70 °C for solvation. Immediately, the solutions were

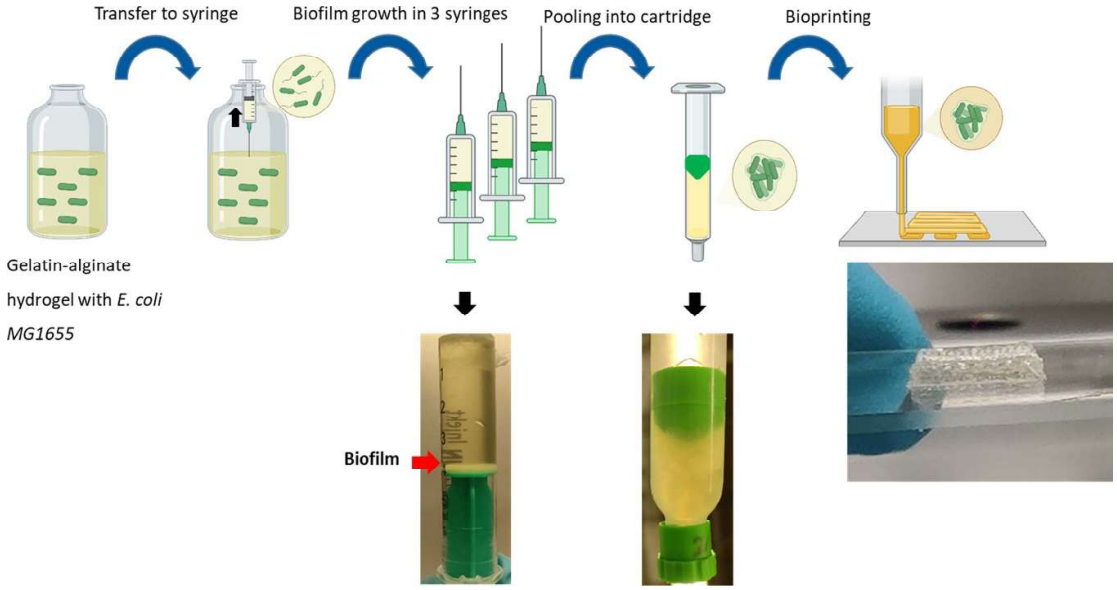


**Figure 1.** Schematic workflow of bioink preparation and bioprinting process of *E. coli* MG1655 biofilms. An inoculated gelatin-alginate based hydrogel was pulled into a syringe. Biofilm was grown on piston while being incubated upside down. Three syringes were pooled and transferred into a cartridge for bioprinting. If required, prints can be crosslinked post-printing with $CaCl_2$.

sterile filtered (0.45 $\mu$m pore size) in 50 ml falcons and stored at 4 °C. For inoculation, the hydrogel was liquefied at 37 °C and 10 ml was transferred to two sterile vials. The following steps are generalized in figure 1. An aliquot of *E. coli* MG1655 O/N culture was measured for the $OD_{600}$ and diluted to contain $10^6$ CFU ml$^{-1}$. A 100 $\mu$l of the aliquot was added to each 10 ml bioink sample. The suspension was briefly stirred and then 5 ml plus ~1 ml air were pulled up into three syringes. Syringes were covered with sterile parafilm and then incubated upside down in Erlenmeyer flasks at 37 °C for 3 d. During this incubation period, the biofilm primarily forms on the surface of the syringe plunger. Then, 4 ml of all three suspensions above the grown biofilms were discarded carefully by a second empty syringe, pushing the supernatant up via a female luer lock adapter. The remaining 1 ml of those three suspensions were pooled carefully from syringe to syringe, with the biofilm detaching from the plungers when pushed out. Then, the bioink was transferred gently to a sterile cartridge. Subsequently, the bioink was slowly rotated (3 rpm, Multi-Rotator PTR-35, Grant, UK) for 3–4 h to prevent sedimentation until the hydrogel solidifies at exactly 21 °C.

As controls, native biofilms and the bioink with dispersed planktonic bacteria were used. Native biofilms were prepared by growing $10^5$ CFU ml$^{-1}$ bacteria in 5 ml LB medium in polystyrene 6-well plates for 3 d at 37 °C, covered with parafilm. In the case of bioink with planktonic bacteria, the cell amount was maintained equal by determining the CFU of the biofilm bioink before. For that, 85 mg of the bioink was solved in 1 ml PBS, vortexed for 10 min (to detach clumps) and plated on LB-agar plates via serial dilution in PBS. A CFU ml$^{-1}$ of $10^{10}$ was then calculated by the bioinks density (957.3 $\pm$ 0.9 mg ml$^{-1}$ via weighing). Then, an *E. coli* MG1655 O/N culture (O/N stirred $\rightarrow$ avoids biofilm aggregations) was concentrated twice by centrifugation at 5000 rpm and the pellet was resuspended first in 2 ml and then in 200 $\mu$l ($10^{12}$ CFU ml$^{-1}$). Then 100 $\mu$l was added into two vials filled with 10 ml of the hydrogel at a final concentration of $10^{10}$ CFU ml$^{-1}$. Thereafter, 5 ml of the bioink was pulled up into a syringe and transferred to a cartridge via a female luer lock adapter. The cartridge was then rotated.

Native planktonic bacteria were also dispersed in LB medium as stated in methods section 2.7.

### 2.3. Rheological analysis

For rheological characterization ~100 $\mu$l of either bioink dispersions was transferred from the cartridge to a syringe via a Luer lock adapter and extruded on a 20 mm parallel Peltier steel plate of a rheometer (Discovery Hybrid, Waters/TA Instruments, Germany). All measurements were conducted at 21 °C. Oscillation amplitude analysis was performed at 1 Hz with a range of 0.01%–1000% strain. Oscillation frequency was performed with 1% strain from 0.1 to 10 Hz. Flow Sweep was performed with shear rate ranging from 1 1 s$^{-1}$ to 100 1 s$^{-1}$.

### 2.4. Printability

Printability of bioinks was characterized via a 3D bioprinter (3D Discovery, RegenHu, Villaz ST-Pierre, Switzerland). A 25 G needle was mounted to the cartridges, which were then connected to an air

pressure source for filament extrusion. To evaluate printability, a solid construct with five layers was printed and weighed. For each bioink, the air pressure was adjusted to achieve a construct weight of 85 mg. This procedure was repeated for all experiments to ensure consistent bioink volume extrusion. All pressure measurements were performed in biological triplicates. Additionally, different shapes and dimensions of prints were fabricated with the selected bioink, designed via the bioprinter's specific software (BIOCAD$^{TM}$), to show bioprinting versatility. To obtain a rapid assessment of viability, we printed bioinks onto LB-agar plates and incubated them O/N at 37 °C.

### 2.5. Fluorescent microscopy of bacteria

Constructs (two layers to avoid signal reduction in higher depths) were printed in a 12 well plate and crosslinked with 2 ml 100 mM $CaCl_2$ for 15 min. Crosslinking was necessary to prevent shape disruption during the staining protocol. Afterwards, the solutions were discarded, and 1 ml of PBS was added. Then, 3 $\mu$l BacLight$^{TM}$ staining solution, consisting of a 1:1 mixture of SYTO 9 (488 nm excitation, green emission) and propidium iodide (490 nm excitation, red emission) was added. Bacteria were stained for 15–20 min in the dark. As controls, native biofilms were prepared as described and stained accordingly with 15 $\mu$l BacLight$^{TM}$ staining solution in the medium to avoid biofilm disruption. Native planktonic bacteria were prepared as previously described, with 90 $\mu$l of the $10^{10}$ CFU ml$^{-1}$ suspension added to 1 ml of PBS in a 12 well plate. Next, bacteria were stained with 3 $\mu$l BacLight$^{TM}$. Bacteria were then imaged at a fluorescence microscope (confocal laser scanning microscope (CLSM), Leica DMi8, Germany), using a 10× objective (HC PL Fluotar 10×/0.3 Dry, Leica, Germany) and the LAS X software. Triplicates of all samples were imaged, each at 2–3 different and random *xyz* positions, providing a strong fluorescent signal. All images were collected, using equal parameters, including gain and laser intensity to ensure comparability.

### 2.6. Scanning electron microscope (SEM) analysis of printed bacteria

Three percent glutaraldehyde were added to cover printed and crosslinked (as stated in section 2.5) biofilms and planktonic bacteria for 90 min. Then, an ethanol dilution series ranging from 30% to 100% (10 min incubation time for each concentration) was added to the prints. Finally, hexamethyldisilazane was added to the prints for another 10 min. The solution was removed, and constructs were kept at room temperature (RT) O/N. Prints were attached to SEM sample holder via adhesive carbon tabs (Plano, Germany) and then gold sputtered for 100 s and analyzed at a SEM (EVO HD15, Zeiss, Germany). Native counterparts were not included, due to transferability issues to the SEM samples holders.

### 2.7. Antibiotic susceptibility

Five layers of non-porous 8 × 8 mm squares of biofilm and planktonic bioink were printed in triplicates into 12 well plates. As control samples native biofilms and native planktonic bacteria were prepared as described previously. Bioprinted bioinks were crosslinked for 15 min at RT with 100 mM $CaCl_2$ solution. Crosslinking agents were removed and 2 ml LB-medium (untreated control) or antibiotic solution in LB medium was added. The antibiotics used were ampicillin (128 $\mu$g ml$^{-1}$; Roth, Germany), tetracycline hydrochloride (4 $\mu$g ml$^{-1}$; Chemodex, Switzerland), colistin sulfate (16 $\mu$g ml$^{-1}$; Adipogen, Switzerland) and ciprofloxacin hydrochloride (0.5 $\mu$g ml$^{-1}$; Sigma-Aldrich, Germany). Same antibiotic treatments were applied for native biofilms and printed planktonic bacteria. For native planktonic bacteria, an O/N culture was set to $10^{10}$ CFU ml$^{-1}$ and 90 $\mu$l (equaled weight of printed constructs) was added to 2 ml of antibiotic solution. After an O/N incubation, printed constructs were washed twice with PBS and then solved in 1 ml ethylenediaminetetraacetic acid (EDTA, 110 mM, Roth, Germany). For CFU determination, serial dilution was prepared in PBS and then plated on LB-agar plates (3 × 20 $\mu$l drops per dilution). Log CFU ml$^{-1}$ was set to 1 when no colonies were grown.

Native biofilms were quickly vortexed in falcons and then 90 $\mu$l were diluted in 1 ml of PBS. After serial dilution in PBS, suspensions were plated accordingly.

For native planktonic bacteria, suspensions were vortexed quickly and diluted 1:10 in 1 ml PBS accordingly. After serial dilution in PBS, suspensions were plated.

### 2.8. Metabolic profile comparison

Bioink with planktonic and biofilm bacteria, respectively, were printed and dissolved in 1 ml LB medium at 37 °C. Accordingly, native biofilm bacteria and planktonic bacteria were prepared and collected into 15 ml falcons. Then, 90 $\mu$l was transferred into 1 ml of LB medium. All bacterial suspensions were transferred into Eppendorf tubes and centrifuged at 5000 rpm. Supernatants were discarded. For medium control subtraction, 1 ml of LB medium and plain hydrogel (for native samples and for printed samples respectively) were centrifuged accordingly, and supernatants were discarded. Since these samples yielded no pellet, the tiny remaining liquids after supernatants' discarding were used. Afterwards, sample preparation and LC-TOF measurements were performed following the protocol of Montefusco-Pereira *et al* [15]. Briefly, 1 ml of methanol was added plus 25 ng sulfadimidine as an internal standard, which was then vortexed for

10 min. The 100 $\mu$l methanol was added to the pellets. LC-TOF measurements were then conducted on a Thermo Dionex Ultimate 3000 RSLC system coupled to a Bruker maXis 4G UHR-Q-TOF-MS. The separation process was performed via an 18 min linear 5%–95% gradient of acetonitrile with 0.1% formic acid (B) in dd$H_2O$ with 0.1% formic acid (A) on a Waters Acquity BEH C18 column (100 × 2.1 mm, 1.7 $\mu$m dp) at a flow rate of 0.6 ml $min^{-1}$ and 45 °C. The LC flow was split to 75 $\mu$l $min^{-1}$ before entering the mass spectrometer. Mass spectra were acquired in centroid mode ranging from 150 to 2500 *m/z* at a 2 Hz scan rate. Statistical non-targeted metabolomics analysis was performed with MetaboScape 9.0.1 (Bruker Daltonics). The minimal intensity threshold for peak detection was set to 2.5 × $10^3$ with a maximum charge state of 3. Retention time alignment to match features between different samples was automatically performed by the feature extraction algorithm. For every condition, 9 replicates were generated and measured twice, resulting in a total number of 18 replicates. Features were only reported if they appeared in at least 18 samples in total and at least 1 replicate of the same condition. After generating a feature table in MetaboScape, all blank features were subtracted from the analysis resulting in a data reduction of 87%. The final data are depicted in feature tables representing the metabolites. Samples can then be compared via their own measured profile.

### 2.9. Cytotoxicity (LDH-assay)

Calu-3 cells were seeded on transwell inserts (3460 Corning Costar, USA) with a cell count of $10^5$ per well. Cells were cultured with 500 $\mu$l medium apically and 1500 $\mu$l basolaterally for 3 d. Then, cells were set up to air–liquid conditions with 500 $\mu$l medium basolateral only for one week. Cell medium was exchanged every second day and quality control and confluence was monitored using bright field microscopy. LDH assay was performed after one week of culture under air–liquid conditions. Prior to the experiment, medium was exchanged. Biofilm bioinks prepared as described were used to directly print two layers of a 6 × 6 mm non-porous structure on cells. Half of the samples were crosslinked for 15 min with 300 $\mu$l 100 mM $CaCl_2$ and then washed twice with PBS. The plain hydrogel without bacteria was printed equally on cells as control. TritonX treated cells served as a dead control and untreated cells as live control. After 6 and 24 h, 200 $\mu$l of basolateral medium was transferred to an Eppendorf tube. LDH solution (Roche, Germany) was prepared according to manufacturer's protocol and 100 $\mu$l of the collected medium were added quickly to 100 $\mu$l of the solution in a 96-well plate. Absorbance was measured at 492 nm, from which toxicity was calculated.

To complement the LDH assay we also performed a Casy® cell counter (OMNI LIFE Science, Germany) analysis to evaluate the viability accordingly, as further described in supporting information 3.5.

### 2.10. Fluorescent staining of printed biofilms and Calu-3 cells

To visualize that biofilms could be formed and controlled on human *in vitro* systems, they were printed thinly (<300 $\mu$m) in different shapes on Calu-3 cells. Calu-3 cells were grown to confluent monolayers on transwell inserts for one week under air–liquid conditions and stained just before the biofilm printing procedure. This was necessary, because the staining dyes are non-specific and could also stain the biofilms after printing, making it difficult to differentiate mammalian and bacterial cell structures. Therefore, cells were fixed with 300 $\mu$l paraformaldehyde apically and basolaterally with 600 $\mu$l for 1 h. Then, 300 $\mu$l blocking buffer was added apically for 20 min. Fluorescence stains were added apically and incubation was performed at RT in the dark. The 300 $\mu$l of 66 $\mu$M rhodamine-phalloidin (540 nm excitation, red emission; Invitrogen™, USA), diluted 1:200 in blocking buffer (1% bovine serum albumin heat shock fraction and 0.05% Saponin (both Sigma Aldrich, Germany), in PBS) was added apically. Cells were stained for 1 h at RT in the dark. Cells were then washed twice with 300 $\mu$l PBS. Next, 200 $\mu$l of 5 $\mu$g $ml^{-1}$ DAPI (364 nm excitation, blue emission; Sigma-Aldrich, Germany) was added apically for 1 h in the dark. Dye solution was removed and 500 $\mu$l PBS was added basolaterally to avoid cell drying.

In parallel, biofilms were stained. For that, 1.5 $\mu$l of SYTO-9 dye from BacLight™ was added into each of the 3 syringes after upper 4 ml were removed. Syringes were kept at 37 °C in the dark for 1 h. Then, the syringes were accordingly pooled and prepared for printing as described previously. Biofilms were then printed (1 layer) on top of stained cells in different shapes and immediately analyzed at the CLSM, using a 10× objective (HC PL Fluotar 10×/0.3 Dry, Leica, Germany) and the LAS X software. Z-stacks were collected of entire thickness from the cell layer and biofilms.

To assess shape retention, stained biofilms were also printed on unstained Calu-3 cell layers. Biofilms were then either crosslinked with 300 $\mu$l $CaCl_2$ for 10 min with two PBS washing steps or not. Cells with biofilms were then cultured O/N in cell culture incubator and subsequently analyzed at the CLSM, using a 10× objective (HC PL Fluotar 10×/0.3 Dry, Leica, Germany) and the LAS X software.

For all images, triplicates were collected, each at 2–3 different and random *xyz* positions, providing a strong fluorescent signal.

### 2.11. Statistics

All experiments were performed in independent biological triplicates, each with technical triplicates

($N = 3$; $n = 9$), unless otherwise stated. Significance was checked for antibiotic susceptibility assays via one-way ANOVA with Tukey's multiple comparison tests. Statistical significance was defined as $^{*}p < 0.05$, $^{**}p < 0.01$, $^{***}p < 0.001$. Error bars indicate standard deviation.

## 3. Results

### 3.1. Optimization of bioink

Firstly, we have developed a method for printing a pre-grown *E. coli* MG1655 biofilms, using a gelatin-alginate based bioink (figure 1). To determine the optimal gelatin-alginate (Gel;Alg) concentrations for the bioink, six different formulations (gelatin[% (w/v)];alginate[% (w/v)]: 2;1–4;2 as final concentration for bioink) were prepared equally. After testing bacterial growth in each candidate bioink, we observed comparable growth rates across all formulations (see supplement figure 1).

#### *3.1.1. Rheological properties and printability*

All bioink candidates were analyzed rheologically and for their printing suitability. The results are summarized in figure 2 (gelatin[% (w/v)];alginate[% (w/v)]: 2;1, 3;1, 4;1) and supplement figure 2 (further tested gelatin-alginate concentrations showing same behavior provided in supplement). All samples showed viscoelastic solid behavior with $G' > G''$ during frequency oscillation (figure 2(A), supplement figure 2(A)). Increasing polymer concentration showed higher $G'$, suggesting more mechanical strength/stiffness. Flow analysis showed shear-thinning behavior for all samples, demonstrated by decreasing viscosity with increasing shear rate (figure 2(B), supplement figure 2(B)). Higher polymer concentrations resulted in higher viscosity, suggesting again higher stiffness. Rheological properties were then complemented with printability properties. Filaments of all bioink candidates were extruded via air pressure. Visual observation of the droplet or filament extrusion process showed higher stiffness and gelation behavior for samples with higher polymer concentration. While 2;1 samples showed still droplet formation, the sample with 3;1 or higher polymer concentration former proper filaments (figure 2(C)). Accordingly, higher concentrations required more pressure to print the same constructs (figure 2(D), supplement table 1). To keep the air pressure as low as possible while still achieving proper filament extrusion, the 3;1 bioink was chosen for all further experiments. In addition, we also investigated the rheological properties and required extrusion pressure of the plain hydrogel (no bacteria) and with planktonic bacteria, which we used as controls. Rheological comparison showed higher mechanical stiffness of the plain hydrogel compared to both bioinks. Planktonic and biofilm bioink revealed also some differences, with planktonic bacteria showing higher mechanical stiffness during frequency oscillation as well as higher required extrusion pressure (figures 2(E) and (F)).

#### *3.1.2. Printing variability: size and shape*

To exemplify design possibilities of bioprinting different constructs with varying shapes and dimensions were printed. Figure 3(A) shows printed biofilm samples of different thickness obtained by increasing the number of layers. Shape design for printing seems unlimited. We have chosen a grid and a star (figure 3(B)). As simplest proof of bacterial viability after printing, their growth was observed. We printed our institutes abbreviation HIPS with biofilm bioink on an agar plate. After incubating at 37 °C for one day, bacterial growth in the printed letters was visible, observed by appeared turbidity (figure 3(C)).

### 3.2. CLSM and SEM analysis of printed biofilm

To visualize bacteria and biofilm structures in the printed constructs, samples printed with planktonic bacteria and biofilm bacteria were subjected to CLSM and SEM. Two layered grids were printed and stained with the live/dead kit BacLight$^{TM}$ (SYTO9/propidium iodide) for CLSM analysis or dried for SEM analysis. The low propidium iodide staining in the printed planktonic construct confirms the macroscopic observation of high bacterial survival after printing (figure 4(A), left). Bioprinted planktonic bacteria showed homogeneously distributed single bacterial cells throughout the construct. The bioprinted biofilms showed as expected a morphology with different sizes of bacterial aggregations (figure 4(A), right). Clearly, the red signal from nucleic acid stain increased when comparing planktonic and biofilm bacteria. Similar observations were made when native biofilms were compared to native planktonic bacteria (supplement figure 3). The propidium iodide stains the nucleic acid inside of dead bacteria or dormant biofilms leaky membranes as well as extracellular DNA, which is a typical component of biofilm matrix. The three days growth in the bioink before printing allow biofilm production and natural cell death. Therefore, the higher red signal in the printed biofilm sample (figure 4(A)) might be rather attributed to the biofilm formation than the higher sensitivity to the printing process. SEM images confirmed the difference in bacterial cell distribution within the construct containing planktonic bacteria and biofilm. While planktonic bacteria were mostly single cells, the biofilm sample showed bacterial aggregates (figure 4(B)).

### 3.3. Antibiotic susceptibility of printed biofilms

A key feature for biofilm models in drug testing is their susceptibility against antibiotics. Therefore, we selected this property as readout to confirm maintenance of biofilm features after printing. Printed planktonic bacteria as well as native biofilms and native planktonic bacteria served as control. Comparability

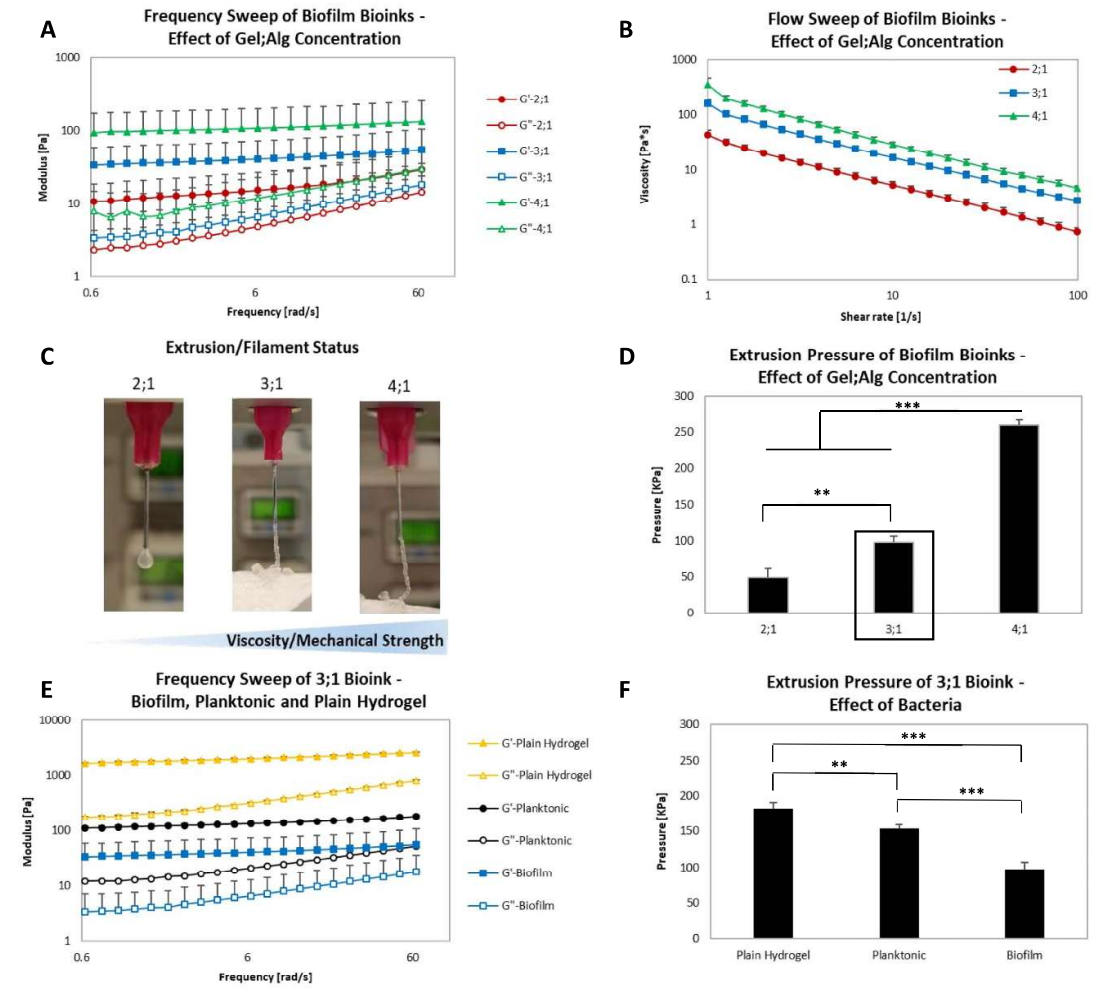


**Figure 2.** Bioink candidates' characterization and selection based on their rheology and filament extrusion with moderate air pressure. Rheological characterization by (A) frequency oscillation. Higher polymer concentrations [%;%] increase $G'$ (storage moduli). All samples show elastic-dominant behavior ($G' > G''$). (B) Flow sweep for determination of shear thinning. All formulations show decreasing viscosity with increasing shear rate. Higher polymer concentrations [%;%] increase viscosity. (C) Observation of filament extrusion. (D) Experimentally determined required extrusion pressure for printing. Bioinks with higher polymer concentrations require higher extrusion pressure. (E) Rheological comparison of 3;1 bioink with biofilm vs planktonic bacteria and plain hydrogel with no bacteria inside. Bioink with planktonic bacteria show higher $G'$ than bioink with biofilm. (F) Printability. The plain hydrogel and the bioink with planktonic bacteria require slightly higher air pressure for printing than the biofilm bioinks. All error bars indicate standard deviation. Single factor ANOVA with Tukey's multiple comparisons was performed; $^{**}p < 0.01$, $^{***}p < 0.001$. Error bars indicate standard deviation.

of the models concerning their bacterial count was shown for untreated samples in each growth condition (supplement figure 3). Susceptibility against the four selected antibiotics is depicted as $\Delta \mathrm{Log}_{10}\mathrm{CFU\ ml}^{-1}$, calculated from the respective untreated controls (figure 5). Overall, susceptibility towards antibiotic treatment was more influenced by the planktonic or biofilm growth, than by the printing procedure. However, bioprinting requires the use of a bioink, which for some antibiotics seem to have an effect as well. For ampicillin, bioprinted biofilms and native biofilms showed no difference and were significantly more resistant than printed and native planktonics, which were completely eradicated. The selected tetracycline concentrations had rather moderate effects under all conditions. Both planktonic conditions as well as native biofilms showed no significant differences. Bioprinted biofilms were significantly more resistant than the other conditions. Against colistin, bioprinted and native biofilms showed similar resistance and were significantly less sensitive than native planktonic bacteria. Although, no significant difference was seen towards biofilms, printed planktonic bacteria showed a more sensitive trend. The sample size n was increased from 9 to 15 for printed planktonic bacteria, but standard deviation was still quite high. A further increase of colistin concentration would have eradicated the biofilms (supplement figure 4). Finally, ciprofloxacin showed similar trends. However, biofilm conditions as well as printed planktonic bacteria were significantly more resistant than native planktonic bacteria. Printed and native biofilms showed again no significant difference. A trend to be more sensitive towards biofilms was shown again by printed planktonic bacteria, which was not significant.

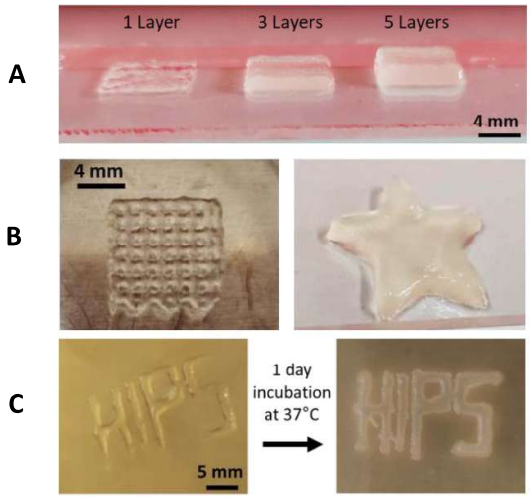


**Figure 3.** Printability options. (A) Solid, square shaped construct with increasing layers resulting in thicker prints. (B) Examples for various printable shapes. (C) Bacterial growth test. Printed biofilms show bacterial growth in shape after one day, observed by appeared turbidity.

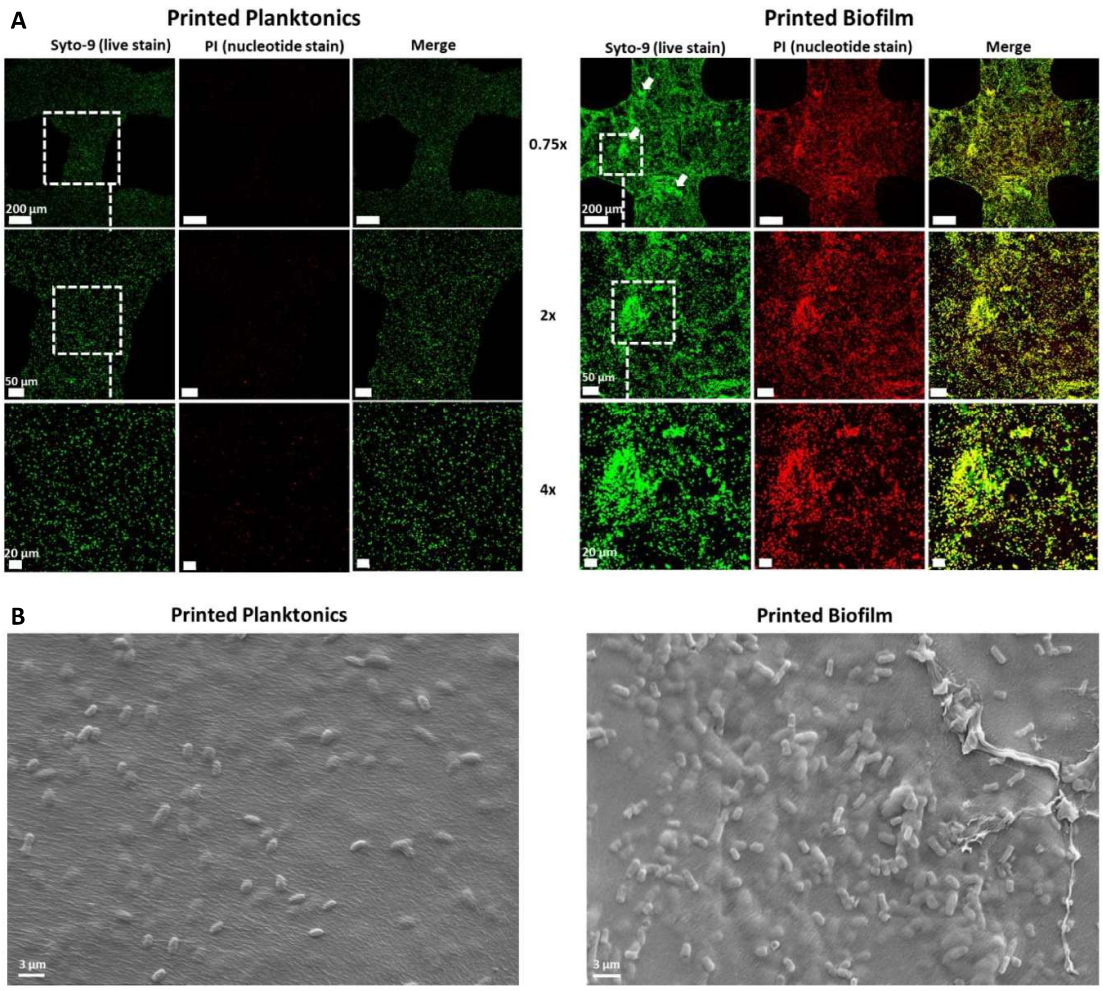


**Figure 4.** Microscopic observation of printed grid constructs. (A) Fluorescence microscopy image ten-fold magnification; Zoom 0.75×, 2× and 4×. Comparison of bacterial distribution and matrix morphology between constructs printed with biofilm vs planktonic bioink. Planktonic bacteria show uniform distribution of mostly single cells. Printed biofilms show bacterial aggregations/clusters distributed within the construct (arrows). The red PI signal is much stronger, indicating more extracellular nucleic acid and dead bacteria. The yellow signal indicates areas of overlap from live and death/nucleic acid stain. (B) SEM images of printed planktonic bacteria and biofilms show distributed single cells or bacterial aggregations, respectively.

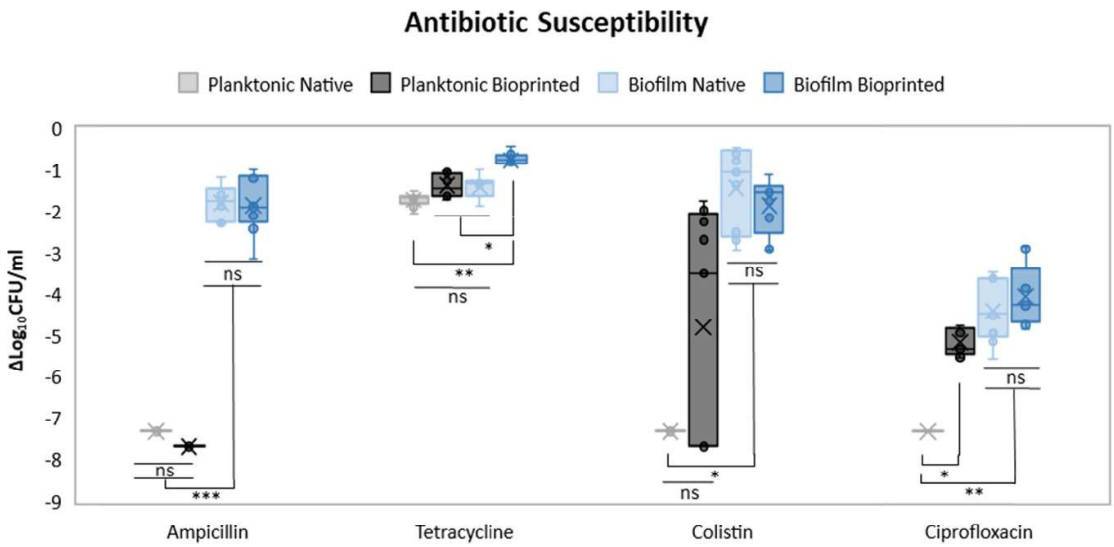


**Figure 5.** Antibiotic susceptibility. Conventional grown planktonic and biofilm cultures were compared to printed planktonic and biofilm constructs in their sensitivity towards ampicillin (128 $\mu$g ml$^{-1}$); tetracycline (4 $\mu$g ml$^{-1}$); colistin (16 $\mu$g ml$^{-1}$); ciprofloxacin (0.5 $\mu$g ml$^{-1}$) by CFU determination and plotting the difference in logarithmic CFU ml$^{-1}$. Printed biofilms show similar susceptibility to native biofilms for all antibiotics except for tetracycline. Planktonic bacteria tend to be more sensitive towards the antibiotics. With $N = 3$ and $n = 9$, except for Colistin-planktonic bioprinted $n = 15$. Single factor ANOVA with Tukey's multiple comparisons was performed; $^{*}p < 0.05$, $^{**}p < 0.01$, $^{***}p < 0.001$. Error bars indicate standard deviation.

**Table 1.** Metabolic profile comparison of printed and native conditions.

| Comparison | Specific features printed | Specific features native | Common features | Total feature | Similarity (%) |
|---|---|---|---|---|---|
| Planktonic printed—planktonic native | 392 | 160 | 2104 | 2656 | 79.2 ± 3.6 |
| Biofilm printed—biofilm native | 629 | 289 | 2113 | 3031 | 69.7 ± 4.4 |

### 3.4. Metabolic profile analysis

A broader indicator for biofilm behavior of bacteria is their metabolism, which we analyzed by LC-TOF measurements for the same four conditions, as described in the previous antibiotic susceptibility testing. To investigate the effect of printed bioinks to native conditions, we compared the entirety of all metabolic features from printed bacteria to their native counterpart (table 1). Specific features are metabolites present only in one condition, whereas common features show metabolites present in both compared conditions. Printed planktonic bacteria and planktonic native bacteria showed similarity of 79.2%, determined by the common and specific feature counts. A high similarity of 69.7% was found for printed and native biofilms too, indicating low impact on native metabolic state by bioprinting.

### 3.5. Bioprinting biofilms on Calu-3 cells

Calu-3 cells were selected as model human epithelial cell line to show that biofilms can be shaped by bioprinting directly on cell layers. Cells were grown at air–liquid conditions, which is quite common in such systems to mimic fundamental respiratory epithelium aspects, but enables us also to deposit our bioinks on a substrate via bioprinting. Cytotoxicity analysis indicated that cells survive the printing process (figure 6(A)). The plain hydrogel without bacteria had no cytotoxic effects. Increased LDH release was measured for bioprinted biofilms crosslinked and non-crosslinked after 6 and 24 h (mean cytotoxicity carrying from 0% to 13%). However, there were no significant differences between the tested groups, indicating that the printing process has no relevant effect on cell integrity. To complement the LDH assay, a viability evaluation was performed with a Casy® cell counter, observing the same trend (supplement table 2). However, a slightly lower viability was shown for samples with printed bacteria on top.

Fluorescence microscopy images showed that biofilms could be printed in various shapes on cells (figure 6(B), supplement figure 5). The 3D image view and orthogonal slices showed direct contact of biofilm with the epithelial surface (figure 6(C)). Shape retention could be maintained when the bioink was crosslinked, whereas non-crosslinked bioink melted at 37 °C during the 1 day incubation (figure 6(D)). However, no n-crosslinked biofilms

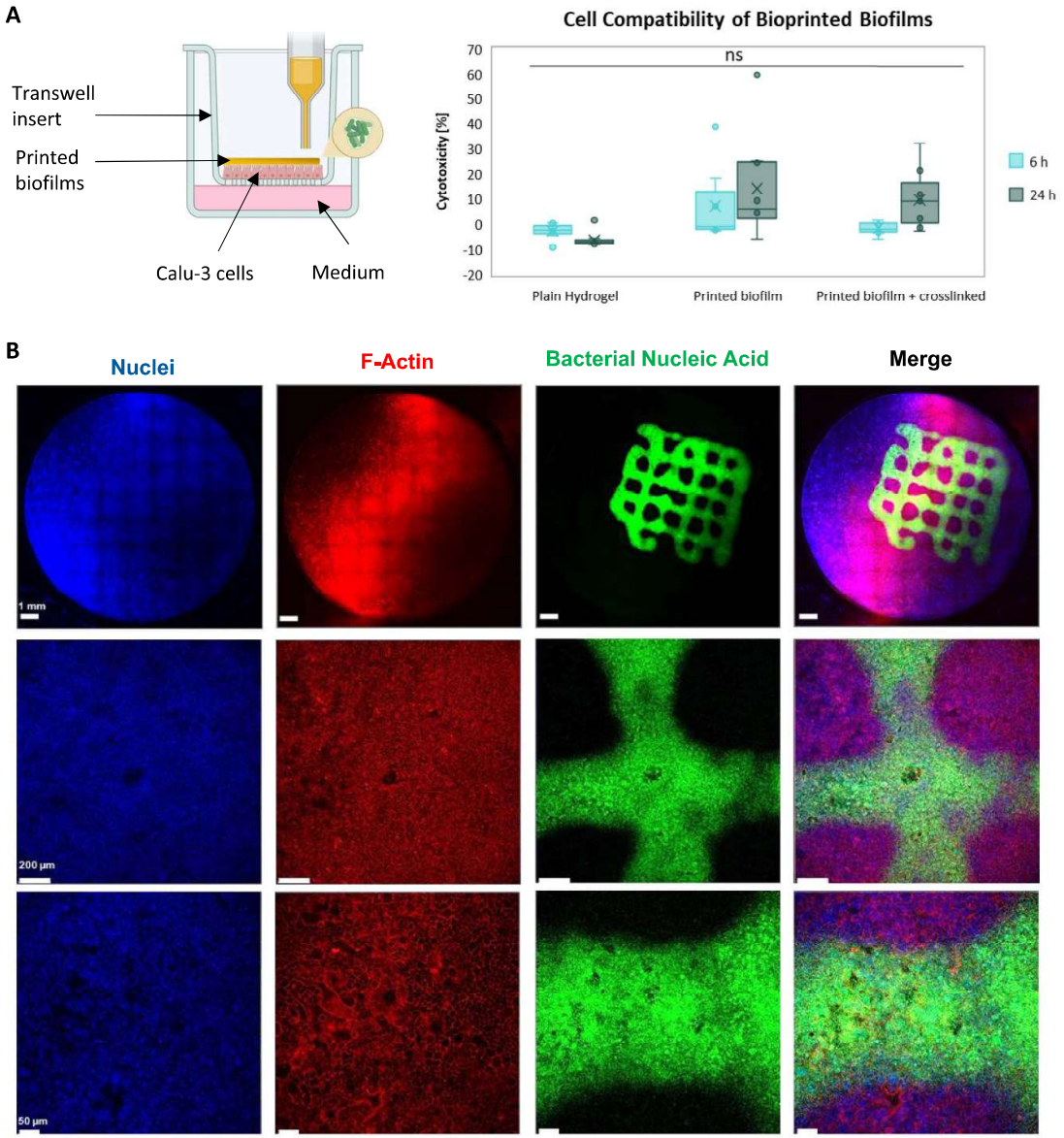


**Figure 6.** Printed E. coli MG1655 biofilms on Calu-3 cells. (A) Scheme of co-culture and LDH assay measured cell membrane damage 6 h and 24 h after printing. No significant differences between the samples and no severe cytotoxic effects were detected. (B) Fluorescence microscopic image of biofilms grid structure printed directly on Calu-3 cells. Blue: DAPI stained nuclei of Calu-3 cells; red: F-Actin stain of Calu-3 cells; green: nucleotide-stain of bacteria. (C) 3D and orthogonal slice views show biofilm on top of cells with cell biofilm interface. (D) Shape retention of printed biofilms. Microscopy image with biofilm stained in green and Calu-3 cells visualized by bright field. Crosslinked bioinks keep their shape after incubation at 37 °C for one day, whereas non-crosslinked bioink melts. However, bacteria/biofilm matrix stay at printed position, even when bioink melts.

showed bacterial shape retention, which means that the bacterial biofilm matrix stayed at the printed position even when the bioink hydrogel melted. The letters of the crosslinked construct showed incomplete fluorescence signal, although visible in bright-field. This might be a result of different *Z*-planes of the letters due to the crosslinking procedure with inhomogeneous swelling and shrinking effects.

## 4. Discussion

Here we report a novel approach for 3D printing of bacterial biofilms on human epithelial cell monolayers which is necessary for modeling biofilm related infectious diseases under controlled conditions *in vitro*. Previous approaches for bioprinting biofilms relied on bioprinting of planktonic bacteria, converting slowly into biofilms after printing [15, 22]. However, this process could lead to premature death of the intended mammalian cell substrate. Therefore, we chose to print *E. coli* MG1655 that had already converted from the planktonic to the biofilm state after dispersion in a suitable gelatin-alginate bioink. The selected polymer concentrations of the bioink showed different rheology when printed with biofilms or planktonic bacteria, respectively. Upon conversion into biofilms, the bioinks showed less mechanical stiffness and required less

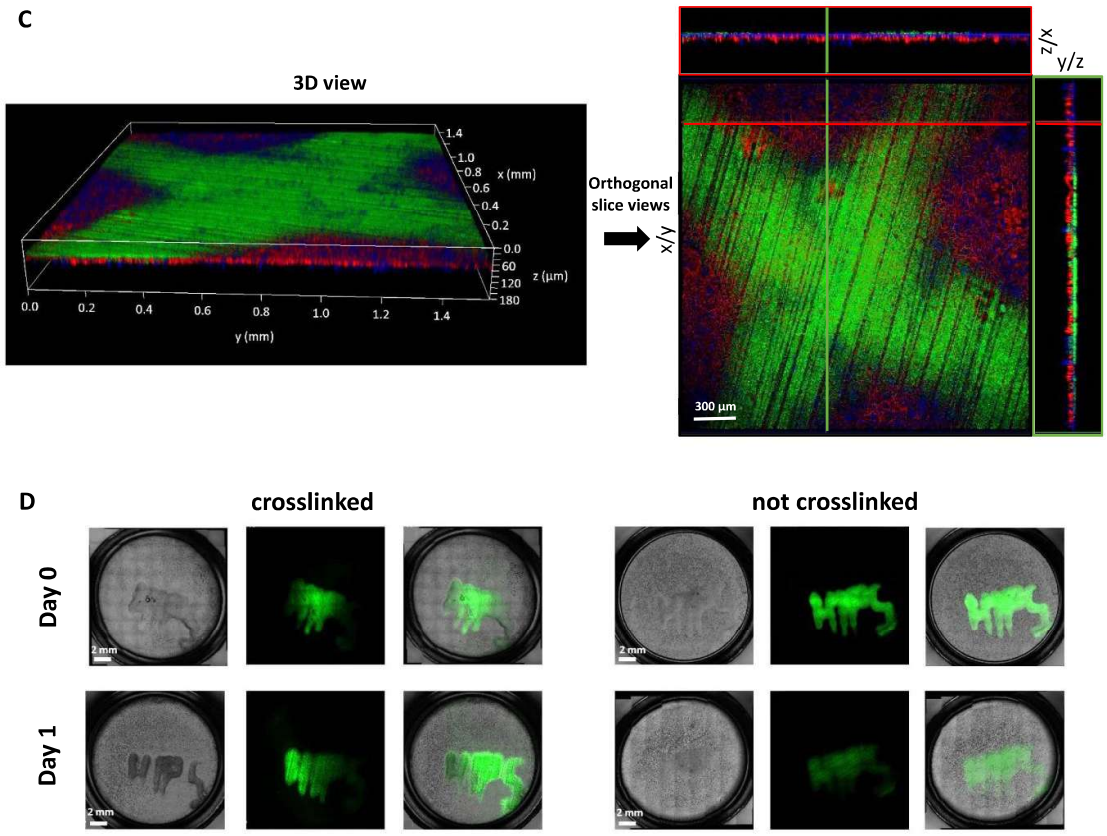


**Figure 6.** (Continued.)

printing pressure, which can be explained either by commencing polymer digestion after 3 d or by a release of rheodestructive components during biofilm formation [12]. Similarly, compared to the plain hydrogel, the planktonic bacteria also showed mechanical strength reduction, indicating an early induction of these processes. While no longer in planktonic, but already in biofilm state, the bacteria could now be printed in a wide range of dimensions and shapes. Flexibility of this approach is highly required for a variety of applications. Varying biofilm thickness could be applied to systematically study biofilm related infections. For example thicker biofilms up to 1000 $\mu$m and beyond are found on implants, catheters or shunts. For skin wounds, lung infections or other tissues the upper size limit is around 200 $\mu$m [29]. These ranges can be achieved by our approach, which might also be a suitable method to test anti-infectives on biofilms with different thicknesses. Shape flexibility might be of great interest to mimic specific biofilm forms, because *in vitro* native biofilms form mushroom shaped-structures, which are not common in *in vivo* biofilm infections [11, 30].

Biofilm morphology could be differentiated from printed planktonic bacteria as biofilms exhibited typical bacterial aggregations, spread in the prints [24]. The increased red signal due to increased presence of nucleic acid was expected, because the longer incubation time can result in more dead bacteria. Another aspect is the option of dormant biofilms with leaky membranes potentially leading to double staining without cells actually being dead [31, 32]. But also, the release of nucleic acid during biofilm formation could enhance the stain. Extracellular DNA is a typical component of biofilm matrix. A differentiation of dead bacteria or nucleic acid release in ECM was not possible with our method. The merge image of the printed biofilm sample, however, shows co-localization of the green signal from the live-stain with red nucleic acid stain resulting in yellow dense clusters as they are anticipated for living bacteria shielding in biofilm matrix. SEM analyzed prints had to be gold-sputtered, which compromises the visibility of the hydrogel structures of the bioink, or bacteria produced ECM. Nevertheless, bacterial aggregates are still observed and are typical for the presence of a biofilm matrix [16, 33].

Antibiotic susceptibility assays indicated that printed biofilms behave similar as native biofilms. The four antibiotics operated differently. Ampicillin had the strongest effect under planktonic conditions, whereas printed and native biofilms showed higher resistance, which was expected, based on previous studies by Ito *et al* [34]. Tetracycline, known to be a bacteriostatic anti-infective, had a comparably low overall effect, but showed significantly higher

effects against printed planktonic and native planktonic bacteria as well as native biofilms than on printed biofilms. This difference of native and printed biofilms was rather unexpected, since it has been reported that tetracycline act more effectively on native biofilms than on planktonic bacteria [35, 36]. Colistin showed no significant difference between printed and native biofilms, but also did no exhibit significant difference towards printed planktonic bacteria. As a molecule with higher molecular weight, colistin may encounter difficulties in penetrating crosslinked hydrogels. Colistin had a stronger effect on native planktonic bacteria, which supports that hypothesis. Ciprofloxacin had a strong effect on all conditions. Again, no significant difference was found between printed and native biofilms. However, higher resistance of printed planktonic bacteria towards native planktonic bacteria was unexpected and could be attributed to the presence of calcium ions in the crosslinked prints. Ciprofloxacin is known to form chelate complexes with calcium and other metal ions [37], leading perhaps to lower effectivity in the printed planktonic bacteria. Overall, the printed biofilms showed high similarity of antibiotic resistance compared to native biofilms, indicating minimal influence on the ECM by printing.

Metabolic profile analysis showed close similarity of printed planktonic and biofilms towards their native counterpart. This suggests that the bioprinting process has only a minor impact on the metabolic state of bacteria. Although, the nutrition base was equal in all conditions, the polymer presence in the bioink could also influence the metabolism and should be considered. Since a metabolic reprogramming does occur in biofilms [38], a closer look into specific metabolic markers with suitable standards could be the subject of metabolomics-based follow-up studies, to compare the planktonic conditions to the biofilms. Genomic and proteomic technologies could give additional insight in this regard.

As a proof of concept, we printed bacterial biofilms on transwell-grown monolayers of human bronchial epithelial cells (Calu-3). We demonstrated cell compatibility of the bioink. Although, crosslinking of bioinks had no direct cytotoxic effects, the addition of $CaCl_2$ could activate undesired signal cascades of cells, which needs to be considered. The slight increase of LDH from 6 h to 24 h indicates that the cause is more likely bacterial rather than the printing procedure. Moreover, other strains and pathogens might harm the cells in a much greater magnitude. As shape retention is also an important aspect for this approach, we demonstrated, that crosslinking printed biofilms on cells can keep their shape at least for one day at 37 °C. Ning *et al* showed that stability of crosslinked prints could be controlled via crosslinking time, $CaCl_2$ concentration or via $BaCl_2$ [28]. Nevertheless, the ECM as produced by the bacteria seems to keep the shape at air–liquid condition also when not crosslinked, even when the bioink melts. This indicates that crosslinking is maybe not necessary to maintain biofilm shape, which could be beneficial when shaping the pure biofilm is required. Furthermore, the direct contact of biofilms with epithelial cells showed more similarities to what actually occurs *in vivo* compared to animal models, using bacteria loaded agar beads [22].

As mentioned previously, current approaches of biofilm infected human *in vitro* model still lack in controllability and reproducibility of biofilm transfer. We showed that 3D bioprinting of biofilms on epithelial cell layer can overcome these limitations. Taking the benefits of our method into account, the approach may be further adapted to other clinically relevant strains like *P. aeruginosa* or *S. aureus*, which might however need a tailored approach for bioinks to satisfy nutritional demands and withstand catalytic bacterial enzymes. However, such strains could potentially be more harmful to the host cells when leaving the printed biofilm matrix, which needs to be considered. Finally, the goal is to develop human-relevant *in vitro* infection models comprising biofilms of defined shape and metabolic status, which can be reproducibly produced and controlled over a longer period of time. This implies that the model should enable repeated drug administration and have the potential to sustain these 'co-cultures' not just for a few days, but for over a week. Complex models like these would allow to generate readouts for both the pathogens and the host cells to better predict the efficacy as well as the safety of tested drugs against biofilm infections.

## 5. Conclusion

We have successfully developed an innovative approach to bioprint biofilms on human epithelial cell layers. A gelatin-alginate based bioink was optimized to print *E. coli* MG1655 biofilm in various shapes and sizes, while retaining biofilm properties. Our method can be applied for multiple analytic options to characterize and evaluate biofilm status, including morphology, antibiotic susceptibility or metabolism. We showed a novel application of directly shaped biofilms on top of Calu-3 cell layer to demonstrate the control potential of *in vitro* biofilm infections. This method could pave the way to establish more robust human based *in vitro* models to test and optimize anti-infective strategies against biofilm related diseases.

## Data availability statement

The data cannot be made publicly available upon publication because they are not available in a format that is sufficiently accessible or reusable by other researchers. The data that support the findings of this

study are available upon reasonable request from the authors.

## Acknowledgments

This project received funding by the SET (Stiftung zur Förderung der Erforschung von Ersatz- und Ergänzungsmethoden zur Einschränkung von Tierversuchen, Frankfurt, Germany) and the Saarland University TANDEM graduate school. Pascal Paul and Annette Boese are thanked for technical support. The graph in figure 1 was created using www.biorender.com.

## Author contributions

Conceptualization, S A, A H, B L and C-M L; Data curation, S A, S F, and N F; Supervision, A H, U F S, T V, B L and C-M L; Writing original Draft, S A; Writing-review and editing, S A, A H, S F, N F, D K, R M, U F S, T V, B L, and C-M L.

All authors have read and agreed to the published version of the manuscript.

## Conflict of interest

The authors declare no conflicts of interest.

## ORCID iDs

Samy Aliyazdi https://orcid.org/0009-0007-4141-5623
Sarah Frisch https://orcid.org/0000-0003-2149-580X
Alberto Hidalgo https://orcid.org/0000-0003-2090-7817
Nicolas Frank https://orcid.org/0000-0001-7170-2366
Daniel Krug https://orcid.org/0000-0002-3664-1884
Rolf Müller https://orcid.org/0000-0002-1042-5665
Ulrich F Schaefer https://orcid.org/0000-0002-2470-2168
Thomas Vogt https://orcid.org/0000-0002-2824-5005
Brigitta Loretz https://orcid.org/0000-0003-0057-5181
Claus-Michael Lehr https://orcid.org/0000-0002-5864-8462

## References

[1] Brinkman C L, Schmidt-Malan S M, Karau M J, Greenwood-Quaintance K, Hassett D J, Mandrekar J N and Patel R 2016 Exposure of bacterial biofilms to electrical current leads to cell death mediated in part by reactive oxygen species *PLoS One* **11** e0168595
[2] Wolcott R D, Rhoads D D, Bennett M E, Wolcott B M, Gogokhia L, Costerton J W and Dowd S E 2010 Chronic wounds and the medical biofilm paradigm *J. Wound Care* **19** 45–53
[3] Bjarnsholt T 2013 The role of bacterial biofilms in chronic infections *APMIS Suppl.* **121** 1–51
[4] Sharma D, Misba L and Khan A U 2019 Antibiotics versus biofilm: an emerging battleground in microbial communities *Antimicrob. Resist. Infect. Control* **8** 76
[5] Singh A, Amod A, Pandey P, Bose P, Pingali M S, Shivalkar S, Varadwaj P K, Sahoo A K and Samanta S K 2022 Bacterial biofilm infections, their resistance to antibiotics therapy and current treatment strategies *Biomed. Mater.* **17** 022003
[6] Kolpen M *et al* 2022 Bacterial biofilms predominate in both acute and chronic human lung infections *Thorax* **77** 1015–22
[7] Singh R, Sahore S, Kaur P, Rani A and Ray P 2016 Penetration barrier contributes to bacterial biofilm-associated resistance against only select antibiotics, and exhibits genus-, strain- and antibiotic-specific differences *Pathog. Dis.* **74** ftw056
[8] Guzmán-Soto I, McTiernan C, Gonzalez-Gomez M, Ross A, Gupta K, Suuronen E J, Mah T-F, Griffith M and Alarcon E I 2021 Mimicking biofilm formation and development: recent progress in *in vitro* and *in vivo* biofilm models *iScience* **24** 102443
[9] Folkesson A, Jelsbak L, Yang L, Johansen H K, Ciofu O, Høiby N and Molin S 2012 Adaptation of Pseudomonas aeruginosa to the cystic fibrosis airway: an evolutionary perspective *Nat. Rev. Microbiol.* **10** 841–51
[10] Høiby N, Ciofu O and Bjarnsholt T 2010 Pseudomonas aeruginosa biofilms in cystic fibrosis *Future Microbiol.* **5** 1663–74
[11] Lebeaux D, Chauhan A, Rendueles O and Beloin C 2013 From *in vitro* to *in vivo* models of bacterial biofilm-related infections *Pathogens* **2** 288–356
[12] Anderson G G, Moreau-Marquis S, Stanton B A and O'Toole G A 2008 *In vitro* analysis of tobramycin-treated Pseudomonas aeruginosa biofilms on cystic fibrosis-derived airway epithelial cells *Infect. Immun.* **76** 1423–33
[13] Woodworth B A, Tamashiro E, Bhargave G, Cohen N A and Palmer J N 2008 An *in vitro* model of Pseudomonas aeruginosa biofilms on viable airway epithelial cell monolayers *Am. J. Rhinol.* **22** 235–8
[14] Bowler L L, Ball T B and Saward L L 2014 A novel *in vitro* co-culture system allows the concurrent analysis of mature biofilm and planktonic bacteria with human lung epithelia *J. Microbiol. Methods* **101** 49–55
[15] Montefusco-Pereira C V, Horstmann J C, Ebensen T, Beisswenger C, Bals R, Guzmán C A, Schneider-Daum N, Carvalho-Wodarz C D S and Lehr C-M 2020 P. aeruginosa infected 3D co-culture of bronchial epithelial cells and macrophages at air-liquid interface for preclinical evaluation of anti-infectives *J. Vis. Exp.* **160**
[16] Horstmann J C *et al* 2022 Transferring microclusters of P. aeruginosa biofilms to the air-liquid interface of bronchial epithelial cells for repeated deposition of aerosolized tobramycin *ACS Infect. Dis.* **8** 137–49
[17] Juntke J, Murgia X, Günday Türeli N, Türeli A E, Thorn C R, Schneider M, Schneider-Daum N, de Souza Carvalho-wodarz C and Lehr C M 2021 Testing of aerosolized ciprofloxacin nanocarriers on cystic fibrosis airway cells infected with P. aeruginosa biofilms *Drug Deliv. Transl. Res.* **11** 1752–65
[18] Gao G, Schilling A F, Yonezawa T, Wang J, Dai G and Cui X 2014 Bioactive nanoparticles stimulate bone tissue formation in bioprinted three-dimensional scaffold and human mesenchymal stem cells *Biotechnol. J.* **9** 1304–11
[19] Noor N, Shapira A, Edri R, Gal I, Wertheim L and Dvir T 2019 3D printing of personalized thick and perfusable cardiac patches and hearts *Adv. Sci.* **6** 1900344
[20] Mirdamadi E, Tashman J W, Shiwarski D J, Palchesko R N and Feinberg A W 2020 FRESH 3D bioprinting a full-size model of the human heart *ACS Biomater. Sci. Eng.* **6** 6453–9
[21] Taymour R, Kilian D, Ahlfeld T, Gelinsky M and Lode A 2021 3D bioprinting of hepatocytes: core-shell structured

co-cultures with fibroblasts for enhanced functionality *Sci. Rep.* **11** 5130
[22] Baltazar T *et al* 2020 Three dimensional bioprinting of a vascularized and perfusable skin graft using human keratinocytes, fibroblasts, pericytes, and endothelial cells *Tissue Eng.* A **26** 227–38
[23] Ozbolat I T, Peng W and Ozbolat V 2016 Application areas of 3D bioprinting *Drug Discov. Today* **21** 1257–71
[24] Schaffner M, Rühs P A, Coulter F, Kilcher S and Studart A R 2017 3D printing of bacteria into functional complex materials *Sci. Adv.* **3** eaao6804
[25] Dubbin K *et al* 2021 Projection microstereolithographic microbial bioprinting for engineered biofilms *Nano Lett.* **21** 1352–9
[26] Spiesz E M, Yu K, Lehner B A E, Schmieden D T, Aubin-Tam M-E and Meyer A S 2019 Three-dimensional patterning of engineered biofilms with a do-it-yourself bioprinter *J. Vis. Exp.* **147**
[27] Balasubramanian S, Yu K, Cardenas D V, Aubin-Tam M-E and Meyer A S 2021 Emergent biological endurance depends on extracellular matrix composition of three-dimensionally printed Escherichia coli biofilms *ACS Synth. Biol.* **10** 2997–3008
[28] Ning E, Turnbull G, Clarke J, Picard F, Riches P, Vendrell M, Graham D, Wark A W, Faulds K and Shu W 2019 3D bioprinting of mature bacterial biofilms for antimicrobial resistance drug testing *Biofabrication* **11** 045018
[29] Bjarnsholt T, Alhede M, Alhede M, Eickhardt-Sørensen S R, Moser C, Kühl M, Jensen P Ø and Høiby N 2013 The *in vivo* biofilm *Trends Microbiol.* **21** 466–74
[30] Ghanbari A, Dehghany J, Schwebs T, Müsken M, Häussler S and Meyer-Hermann M 2016 Inoculation density and nutrient level determine the formation of mushroom-shaped structures in Pseudomonas aeruginosa biofilms *Sci. Rep.* **6** 32097
[31] Chihara K, Matsumoto S, Kagawa Y and Tsuneda S 2015 Mathematical modeling of dormant cell formation in growing biofilm *Front. Microbiol.* **6** 534
[32] Zou J, Peng B, Qu J and Zheng J 2021 Are bacterial persisters dormant cells only? *Front. Microbiol.* **12** 708580
[33] Ansari M A, Khan H M, Khan A A, Cameotra S S and Pal R 2014 Antibiofilm efficacy of silver nanoparticles against biofilm of extended spectrum β-lactamase isolates of Escherichia coli and Klebsiella pneumoniae *Appl. Nanosci.* **4** 859–68
[34] Ito A, Taniuchi A, May T, Kawata K and Okabe S 2009 Increased antibiotic resistance of Escherichia coli in mature biofilms *Appl. Environ. Microbiol.* **75** 4093–100
[35] Stone G, Wood P, Dixon L, Keyhan M and Matin A 2002 Tetracycline rapidly reaches all the constituent cells of uropathogenic Escherichia coli biofilms *Antimicrob. Agents Chemother.* **46** 2458–61
[36] Hu X, Zhang Y, Chen Z, Gao Y, Teppen B, Boyd S A, Zhang W, Tiedje J M and Li H 2023 Tetracycline accumulation in biofilms enhances the selection pressure on Escherichia coli for expression of antibiotic resistance *Sci. Total Environ.* **857** 159441
[37] El-Sabawi D, Abu-Dahab R, Zalloum W A, Ijbara F and Hamdan I I 2019 The effect of ferrous ions, calcium ions and citric acid on absorption of ciprofloxacin across CaCo-2 cells: practical and structural approach *Drug Dev. Ind. Pharm.* **45** 292–303
[38] Guo R, Luo X, Liu J and Lu H 2021 Mass spectrometry based targeted metabolomics precisely characterized new functional metabolites that regulate biofilm formation in Escherichia coli *Anal. Chim. Acta* **1145** 26–36

## 4.2 A Novel 3D Printed Model of Infected Human Hair Follicles to Demonstrate Targeted Delivery of Nanoantibiotics

**Samy Aliyazdi,** Sarah Frisch, Tobias Neu, Barbara Veldung, Pankaj Karande, Ulrich F Schaefer, Brigitta Loretz, Thomas Vogt, Claus-Michael Lehr

ACS Biomaterials Science & Engineering; Volume 10, Issue 8; August 12, 2024
Pages 4645-5408

https://doi.org/10.1021/acsbiomaterials.4c00570

**Author Contributions**

S.A. and S.F. contributed equally. S.A., S.F., C.-M.L., B.L., U.F.S., T.V., and P.K. performed conceptualization; S.A., S.F., and T.N. performed data curation; C.-M.L., B.L., U.F.S., and T.V. performed supervision; B.V. and P.K. performed resources acquisition; S.A. performed writing of the original draft; S.A., S.F., C.-M.L., B.L., U.F.S., T.V., T.N., B.V., and P.K. performed review and editing of the manuscript. The manuscript was written through contributions of all authors.

ACS Biomaterials SCIENCE & ENGINEERING



pubs.acs.org/journal/abseba
Article

# A Novel 3D Printed Model of Infected Human Hair Follicles to Demonstrate Targeted Delivery of Nanoantibiotics

Samy Aliyazdi,[#] Sarah Frisch,[#] Tobias Neu, Barbara Veldung, Pankaj Karande, Ulrich F Schaefer, Brigitta Loretz, Thomas Vogt, and Claus-Michael Lehr*

Cite This: *ACS Biomater. Sci. Eng.* 2024, 10, 4947−4957



**ABSTRACT:** Hair follicle-penetrating nanoparticles offer a promising avenue for targeted antibiotic delivery, especially in challenging infections like acne inversa or folliculitis decalvans. However, demonstrating their efficacy with existing preclinical models remains difficult. This study presents an innovative approach using a 3D *in vitro* organ culture system with human hair follicles to investigate the hypothesis that antibiotic nanocarriers may reach bacteria within the follicular cleft more effectively than free drugs. Living human hair follicles were transplanted into a collagen matrix within a 3D printed polymer scaffold to replicate the follicle's microenvironment. Hair growth kinetics over 7 days resembled those of simple floating cultures. In the 3D model, fluorescent nanoparticles exhibited some penetration into the follicle, not observed in floating cultures. *Staphylococcus aureus* bacteria displayed similar distribution profiles postinfection of follicles. While rifampicin-loaded lipid nanocapsules were as effective as free rifampicin in floating cultures, only nanoencapsulated rifampicin achieved the same reduction of CFU/mL in the 3D model. This underscores the hair follicle microenvironment's critical role in limiting conventional antibiotic treatment efficacy. By mimicking this microenvironment, the 3D model demonstrates the advantage of topically administered nanocarriers for targeted antibiotic therapy against follicular infections.

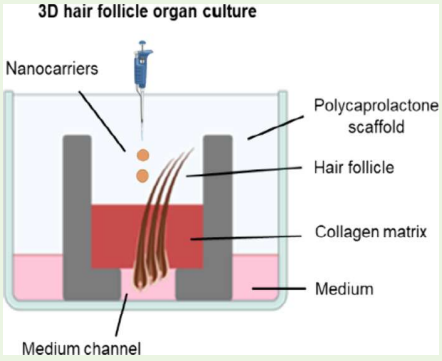


**KEYWORDS:** *in vitro model, hair follicle infection, follicular transport, 3D fabrication, tissue engineering*



## 1. INTRODUCTION

Hair follicles (HFs) are intricate structures comprising diverse cell types that fulfill vital roles in hair growth, cycling, and regeneration. Understandably, it is a complex task to mimic the physiological conditions *in vitro* for targeted drug testing. The various available models have specific applications and limitations. The pig ear model has been the most used for performing nanoparticle uptake studies as it has been established that nanosystems in the submicrometer size range can penetrate and accumulate within HFs.[1−4] For instance, Lademann et al. showed how dye-loaded nanoparticles (320 nm) can effectively penetrate into HFs of pig ears.[5] Another example by Raber et al. showed the uptake of poly(DL-lactide-*co*-glycolide) (PLGA) nanoparticles into pig ear HFs.[6] Recently, follicular uptake was also shown for lipid-based nanoparticles on the pig ear model. While the pig ear model is suitable to demonstrate HF penetration due to high similarity,[7] it is a tissue that cannot be cultured over a longer time. The lack of cultivability limits the use of biological efficacy and tissue or immune response. Additionally, the interspecies difference could lead to a distinct immune response. Human skin biopsies are another model for such nanocarrier penetration studies. Christmann et al. showed HF penetration of PLGA nanoparticles (150 nm) into skin biopsies of human body donors.[8] Hair loss diseases, like alopecia areata, have been a major interest of such studies. However, once again, the lack of accessibility to intact HFs makes it difficult to analyze biological effects. Both models are suitable to be applied for demonstration of HF penetration with dye-loaded nanocarriers, but not for efficacy testing of drug-loaded systems. The presence of a functional HF holds the potential to unlock a multitude of applications, offering the possibility to assess the follicle's condition in relation to various hair-related diseases.

Another approach uses isolated HFs cultured floating in a liquid medium. In 1990, Philpott et al. reported their HF organ culture from isolated human scalp skin, which was also applied for hair growth studies and hair loss diseases.[9] This model's strength is its suitability for biological effect investigation over several days. However, using such cultures for other applications, like drug delivery systems and bacterial infections, remains uninvestigated. A limitation arises from the fact that HFs, which are naturally enveloped by a three-dimensional

Received: March 26, 2024
Revised: June 7, 2024
Accepted: June 26, 2024
Published: July 4, 2024





https://doi.org/10.1021/acsbiomaterials.4c00570
*ACS Biomater. Sci. Eng.* 2024, 10, 4947−4957

matrix *in vivo*, cannot be effectively exposed to topical nanocarrier formulations or bacteria in this floating state.[9,10] More recent methodologies incorporate tissue engineering, wherein dermal papilla cells are seeded within a 3D human skin construct to generate a complete HF model.[11] While these models approximate *in vivo* conditions, they remain intricate, costly, and time-intensive.

Given these limitations, HF infection diseases have still not been approached *ex vivo* or *in vitro* for investigations. Acne inversa and folliculitis decalvans are two examples of such HF infections. Folliculitis decalvans manifests as an inflammatory scalp ailment, presenting lesions characterized by follicular pustules.[12,13] In the pathogenesis of this disease, *Staphylococcus aureus* (*S. aureus*) emerges as a predominant microbe.[12,13] Acne inversa, also termed hidradenitis suppurativa, represents another inflammatory disorder affecting the skin and HFs in regions like the axillary, genital, inframammary, or inguinal areas.[14] Although the exact involvement of bacteria and the microbiome in the disease is still being investigated, *S. aureus* seems to play a role alongside other bacteria.[15] Despite the clinical significance of such diseases,[16,17] the mechanisms underpinning the treatment strategies remain inadequately comprehended. Typically, eradicating *S. aureus* is a primary objective aimed for but not always achieved through systemic or topical administration of antibiotics such as rifampicin.[18,19] However, potential side effects of systemic approaches are a concern. In addition, antibiotic resistance and the development of biofilms by pathogens like *S. aureus* have been linked to treatment failures and the establishment of chronic conditions.[20,21] To combat such infections, future approaches will necessitate novel anti-infectives delivered via advanced nanocarriers, acting as a reservoir at the site of infection. To study such anti-infective-loaded nanocarriers for topical administration, suitable disease models are required. The aforementioned approaches are not suitable for such studies. Considering the floating HF approach, which is already unsuitable for topical nanocarriers, the presence of bacteria in a liquid medium would result in rapid unphysiological bacterial growth. The human skin biopsies and the pig ear model are also not suitable due to the lack of access to the HFs and the missing method to determine the efficacy of anti-infectives against the bacteria inside the HF. Hence, we aimed to synergize approaches involving isolated human HFs and 3D matrices. We devised a 3D model encompassing a collagen matrix within a 3D printed polycaprolactone (PCL) scaffold, with isolated human HFs perpendicularly embedded/seeded. Hair growth kinetics were measured and compared to conventional floating follicle cultures. The application of fluorescent spheres (200 nm) on both approaches highlighted the pivotal role of the HFs' surrounding environment. Additionally, we established an infection of the matrix-embedded HFs via *S. aureus*. To demonstrate the advantage of nanocarriers for targeted antibacterial drug delivery, we employed antibiotic-loaded lipid-based nanoparticles, which recently have shown promising results for follicular targeting on pig ears but also human skin biopsies.[22,23] We prepared rifampicin-loaded lipid nanocapsules (LNCs) to compare their efficacy in both the infected 3D model and the conventional floating culture.

## 2. MATERIALS AND METHODS

**2.1. Bacterial Culture.** *S. aureus* Newman GFP (ATCC 25904-pCtuf-gfp) was selected as a model pathogen to infect the HFs. For overnight culture, *S. aureus* was grown in 20 mL of a brain heart infusion medium with chloramphenicol, shaking (180 rpm) at 37 °C. Overnight culture was prepared by inoculating a colony from BHI-agar plates with chloramphenicol, streaked from glycerol stocks.

**2.2. Hair Follicle Isolation.** HFs were isolated from facial and abdominal skin tissues obtained from cosmetic surgery. Ethical approval (BU/170/20 Ethikkommission Ärztekammer des Saarlandes) and patient consent were obtained. The skin tissues were cut into 1−2 $cm^2$ pieces and transferred to a Petri dish containing a washing buffer (phosphate-buffered saline (PBS), 5% fetal calf serum, 1000 U/mL penicillin, 1 mg/mL streptomycin, and 25 μg/mL amphotericin B, all from Life Technologies, UK). The epidermis and upper parts of the dermis were removed using a scalpel until the dermal-subcutis junction (grid pattern) was visible. HFs were gently pulled out under a stereomicroscope (Olympus, Germany) using fine tweezers. Anagen HFs, selected based on their morphology under the microscope, were collected in another Petri dish containing William's E medium (Life Technologies, UK) with 500 U/mL penicillin, 0.5 mg/mL streptomycin, and 12.5 μg/mL amphotericin B. Subsequently, the HFs were transferred individually into single wells of a 24-well plate with 1.5 mL of fully supplemented William's E medium (unless otherwise stated), with 10 μg/mL insulin (Sigma, Germany), 2 mM glutamine (Life Technologies, UK), and 10 ng/mL hydrocortisone (Sigma, Germany). The HFs were then incubated overnight before any experiments were performed.

**2.3. 3D Organ Culture of Hair Follicles.** First, a PCL scaffold was 3D printed in a six-well plate, creating three channels that were subsequently filled by 3D printing a 25% Pluronic−F127 hydrogel (in William's E medium and sterile-filtered before solidification) inside them (Figure 1A). The Pluronic serves as a sacrificial hydrogel to support the HFs to stay in position until the collagen is added. Accordingly, 1−3 HFs (specified for each experiment) were gently inserted into the tail (Corning, USA), composed of 80% (v/v) collagen, 10% (v/v) fully supplemented William's E medium, and 10% (v/v) neutralization solution (0.05 M NaOH, 2.2% $NaHCO_3$, and 200 mM HEPES in Milli-Q), and were added into the PCL scaffold, ensuring that the HF tips remained in contact with air. The incorporation of collagen to this model intended to surround the HFs with an environment resembling the dermis, where collagen is the main extracellular component. The plate was then incubated for 10 min at 37 °C, before adding 1.5 mL (unless otherwise stated) of fully supplemented William's E medium to cover the bottom of the model,

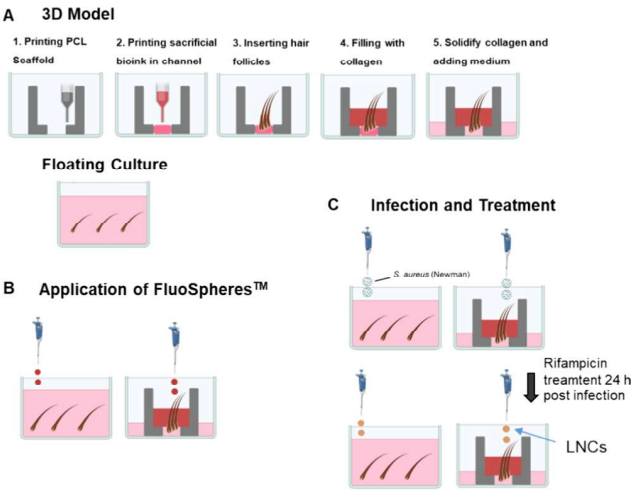


**Figure 1.** Scheme of procedures. (A) Scheme of the printing procedure for the 3D model and the HF insert. As control is the conventional floating culture of HFs. (B) Application of FluoSpheres for follicular transport on both culture types. (C) Infection of cultures via *S. aureus* Newman suspension drops with rifampicin treatment 24 h postinfection.


https://doi.org/10.1021/acsbiomaterials.4c00570
ACS Biomater. Sci. Eng. 2024, 10, 4947−4957

which also dissolved the Pluronic−F127 gradually. Additional technical details of the model are listed in Table S1.

**2.4. Hair Growth Evaluation.** Hair growth was assessed in the 3D model and the floating follicle approach. Due to limitations in the supply of skin tissues, only one HF was used in each culture. HFs were initially imaged under the stereomicroscope immediately after isolation. Only HFs that still exhibited the anagen phase after 1 day were used for the experiment. For the floating HFs, growth measurements were taken daily in the well plate. In the case of the 3D organ culture, each model was assigned to a specific day (with one HF per model) because the HFs were removed from the model for measurement under the stereomicroscope. The increase in hair length was evaluated using scale bar scale setting and line length measurement of ImageJ (NIH, USA).

**2.5. Follicular Transport.** To assess follicular transport, the floating culture and the 3D model were prepared as described previously. After 24 h, FluoSpheres carboxylate-modified microspheres (Thermo Fisher Scientific, Germany), red fluorescent spheres with a size of 200 nm, were diluted 1:10 in Milli-Q water. Then, 20 $\mu$L of the diluted solution was gently dropped on top of both cultures (Figure 1B). Follicular transport was assessed after 4 and 24 h. For this purpose, HFs were gently pulled using fine forceps and washed three times with 100 $\mu$L of PBS to remove all peripheral particles. Subsequently, the HFs were placed in a transparent 96-well plate (Black, Greiner Cellstar, Germany). Promptly, fluorescence imaging was performed using the live cell imaging system of a Spark Cyto (Tecan, Switzerland). Imaging was conducted with an LED intensity of 100% and an exposure time of 200 ms. Intensity profiles were generated by using the gray values of the received images. To do this, a region of interest was marked via ImageJ, covering only the HF, shown as a yellow rectangle. The intensity profile was then determined from the hair tip to the hair bulb, using the plot profile tool of ImageJ. To compare the floating culture with the 3D model, HFs of similar size were selected.

**2.6. Hair Follicle Infection.** To mimic an HF infection, the 3D models were infected with drops of *S. aureus* Newman (Figure 1C). The 3D model samples were prepared with three HFs. Accordingly, floating HFs were set up in a six-well plate with three follicles per well. An *S. aureus* overnight culture was adjusted to an $OD_{600}$ of 0.2. Subsequently, 2 $\mu$L of the bacterial suspension was dropped onto either the 3D model, ensuring contact with the HF tips, or onto the floating approach, by pipetting the drop directly into the medium. The models were then incubated overnight at 37 °C.

**2.7. Cytokine Release.** We assessed cytokine release for interleukin 6 (IL-6), interleukin 8 (IL-8), and TNF$\alpha$ using a BD cytometric bead array (BD Biosciences, Germany). We prepared 3D HF models and infected them as described previously. The medium volume was reduced to 1 mL for this experiment to avoid excessive dilution. Noninfected models served as the control, as well as infected and noninfected floating HFs. We collected medium samples (60 $\mu$L) at 4 and 24 h after infection and stored them at −80 °C before performing the assay. The assay was conducted following the manufacturer's protocol, using 50 $\mu$L of the samples for the measurements via a flow cytometer (BD LSRFortessa, BD Biosciences, Germany).

**2.8. Rifampicin-Loaded LNCs.** As a treatment option, LNCs were selectively loaded with rifampicin. These LNCs are composed of an oily core surrounded by layers of Span 80 and a PEGylated surfactant, based on the studies of Bastiat et al.[24] To load LNCs with rifampicin, we employed a micromixing method. Briefly, we weighed 600 mg of soybean oil (Fisher Scientific, Germany), 600 mg of Migylol 812 (Caelo, Germany), 600 mg of Kolliphor (Sigma, Germany), 200 mg of Span 80 (Sigma, Germany), and 6 mg of rifampicin (US Biological, USA) into a vial and heated the mixture to 40 °C until the lipids melted. The contents were then transferred to a syringe (5 mL, Braun, Germany) compatible with the micromixer (IDEX, USA). Another syringe (10 mL) was filled with 8000 mg of Milli-Q water. For the Milli-Q, we set the flow rate to 2.320 mL/min, and for the oil mix, it was set to 0.580 mL/min. Flow rates were based on preliminary establishment, assuring no adverse effects on particle size or polydispersity. The diameter of the capillaries was 0.2 mm, ended in a 0.5 mm T-shaped micromixer. We discarded the droplets from the first 15 s and collected the remainder in another vial. The particle concentration was 200 mg/mL, calculated from proportions of flow rates. This was validated experimentally by freeze-drying samples and measuring the mass of the remaining lipid phases during preliminary establishment, which was consistent with the calculated mass.

**2.9. Characterization of LNCs.** *2.9.1. Dynamic Light Scattering.* The size and PDI of the LNC formulation were investigated using dynamic light scattering. The measurements were carried out on a Malvern Zetasizer Nano ZSP (Malvern, Germany). The data were analyzed using Zetasizer software (Malvern, Germany). The measurements were performed with 12 different batches of the LNCs at 25 °C after 120 s equilibration in three repetitions, and then, the average value was determined. Before measurement, LNCs were diluted 1:400 in Milli-Q.

*2.9.2. Entrapment Efficiency and Drug Loading.* The entrapment efficiency (EE) and drug loading (DL) were investigated using an indirect method. A 4% LNC suspension was filtered through an Amicon filter tube (Amicon Ultra-4, UFC810024, Merck Millipore, Ireland) with a 100.000 kDa molecular weight cutoff membrane. These filter tubes consisted of two chambers and a filter membrane. For that, 2 mL of the LNC suspension was placed in the upper chamber and filtered through the membrane at 150 g for 15 min (Rotina 420R, Hettich, Germany). Afterward, the concentration of rifampicin in the supernatant (lower chamber) was quantified using absorption measurement at 472 nm (Tecan Infinite 200 Pro, Tecan, Germany). To ensure that no LNCs were present in the supernatant, a dynamic light scattering measurement was performed. The EE and DL was then calculated using the following equations:

$$\%\ \text{entrapment efficiency (EE)} = 1 - \frac{m_{\text{rifampicin}}\ \text{in the supernatant}}{m_{\text{rifampicin}}\ \text{in the formulation}} \times 100$$

$$\%\ \text{drug loading (DL)} = \frac{m_{\text{rifampicin}} \times \text{EE}}{m_{\text{LNC}}} \times 100$$

*2.9.3. Drug Release.* Finally, the release behavior was also analyzed. For that, 2 mL of freshly rifampicin-loaded LNCs was transferred into dialysis tubes (MWCO: 3.5 kDa, Repligen, USA) and clipped on both sites. Tubes were transferred into 250 mL of Milli-Q. Releases were conducted over 24 h with gentle magnetic stirring. Samples (200 $\mu$L) were withdrawn after 1, 2, 4, 6, 8, and 24 h and pipetted into vials. Quantification of rifampicin was conducted on a Thermo Scientific Dionex UltiMate 3000 RS system with an Accucore RP-MS (Thermo Fisher Scientific, Germany) column. The mobile phase consisted of eluent A $H_2O$ with 0.1% (v/v) formic acid and eluent B acetonitrile with 0.1% (v/v) formic acid with a flow rate of 0.3 mL/min. The column temperature was set at 30 °C, while a 3 $\mu$L sample volume was injected. Data acquisition and analysis were performed by Xcalibur software. Mass spectrometry analysis was carried out on a TSQ Quantum Access MAX triple-quadrupole mass spectrometer system fitted with an electrospray interface operated under selected reaction monitoring transitions. The $m/z$ transitions for rifampicin were 823.295 → 150.966 $m/z$ and 823.295 → 162.927. Analyst Xcalibur software was used for instrument control and quantitative data analysis.

**2.10. Treatment of Hair Follicle Cultures with LNCs.** As a proof of concept, infected HF cultures were treated with rifampicin-loaded LNCs. To achieve this, 3D cultures and floating HFs were prepared and infected as described previously, here with three HFs per culture. After 24 h, the cultures were treated with 20 $\mu$L of 1:40 diluted rifampicin-loaded LNCs (5 mg/mL, with 15 $\mu$g/mL rifampicin in accordance with DL), which were added on top of each culture (Figure 1C). In accordance with a release study (Figure 6A), a rifampicin concentration of ∼10 $\mu$g/mL can be expected. As controls, other cultures were treated with plain LNCs (not loaded


https://doi.org/10.1021/acsbiomaterials.4c00570
ACS Biomater. Sci. Eng. 2024, 10, 4947−4957

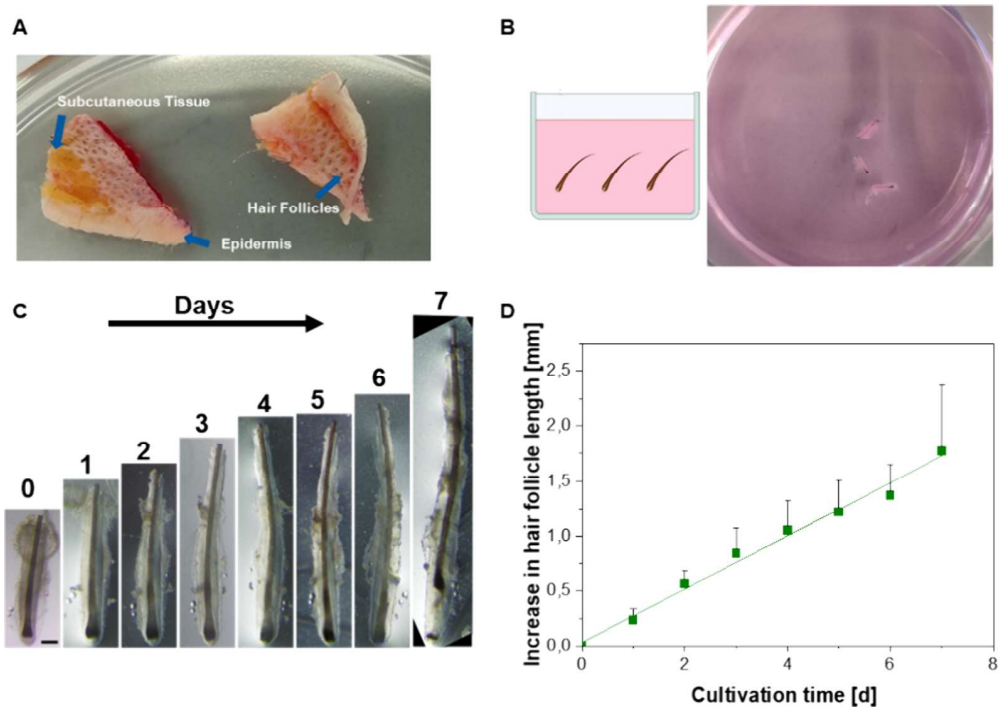


**Figure 2.** HF isolation and culture. (A) HF isolation from skin tissue via forceps. (B) Scheme and well of HF culture, floating within a medium. (C) Bright-field microscopy of a growing HF, cultured for a week. The scale bar equals 200 $\mu$m. (D) Quantification of HF growth over a week with $N = 4$; $n = 12$. Error bars represent standard deviation.

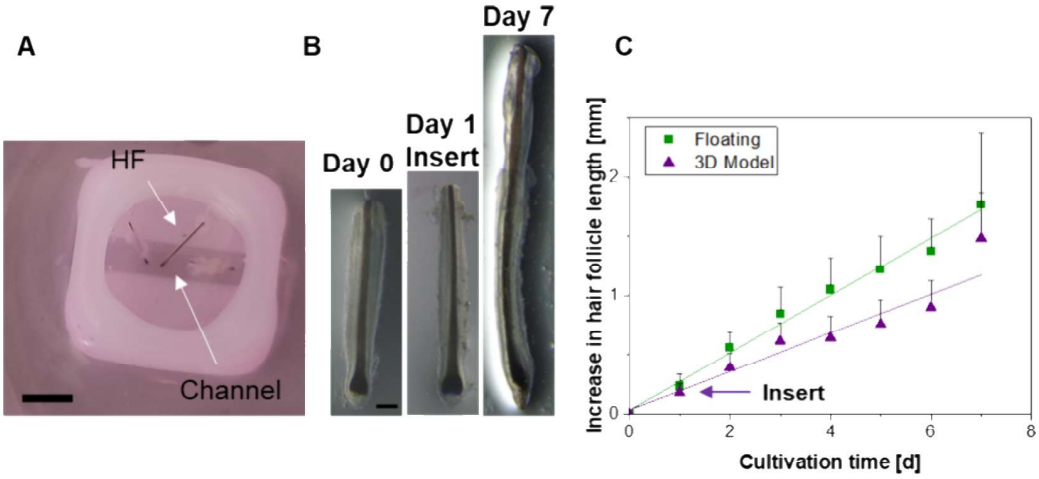


**Figure 3.** 3D culture of HFs. (A) Image of the 3D model with 3 HFs. The scale bar equals 2 mm. (B) Bright-field microscopy of HF cultured from day 1 to 7 in the model. Images of other days depicted in Figure S1. The scale bar equals 200 $\mu$m. (C) Quantification of growth for both the 3D model and floating follicles with $N = 2–4$; $n = 4–12$.

with rifampicin), as well as with 20 $\mu$L of free rifampicin (10 $\mu$g/mL). These treatments were conducted for 24 h at 37 °C. Subsequently, all three HFs of each culture approach were collected and individually transferred via sterile tweezers into 1 mL of PBS (1 HF in 1 mL) and vortexed at maximum speed for 15 min. To determine the colony-forming units per mL (CFU/mL), 20 $\mu$L of each sample was added to 180 $\mu$L of PBS in 96-well plates. Serial dilution was performed via 1:10 steps in PBS with an automatic multichannel pipet (Eppendorf, Germany). Three drops of 20 $\mu$L were then added on BHI-agar plates and incubated overnight at 30 °C. Then, the CFU was determined at the lowest possible dilution, where colonies could be clearly distinguished and counted accurately.

**2.11. Statistics.** All experiments were performed in independent biological triplicates, each with technical triplicates ($N = 3$; $n = 9$), unless otherwise stated. Significance was checked for cytokine release via *t*-tests and for the rifampicin-loaded LNC treatment via one-way ANOVA with Tukey's multiple-comparison tests. Statistical significance was defined as $*p < 0.05$, $**p < 0.01$, and $***p < 0.001$. Error bars indicate standard deviation.

## 3. RESULTS

**3.1. Culture of Floating Hair Follicles.** First, we isolated HFs from the skin tissue (Figure 2A) and assessed their cultivability by suspending them in a nutrient medium (Figure 2B). This was done to replicate a well-known cultivation method and provide a reference point for hair growth comparison. The HFs exhibited over 1 mm of growth within


https://doi.org/10.1021/acsbiomaterials.4c00570
ACS Biomater. Sci. Eng. 2024, 10, 4947−4957

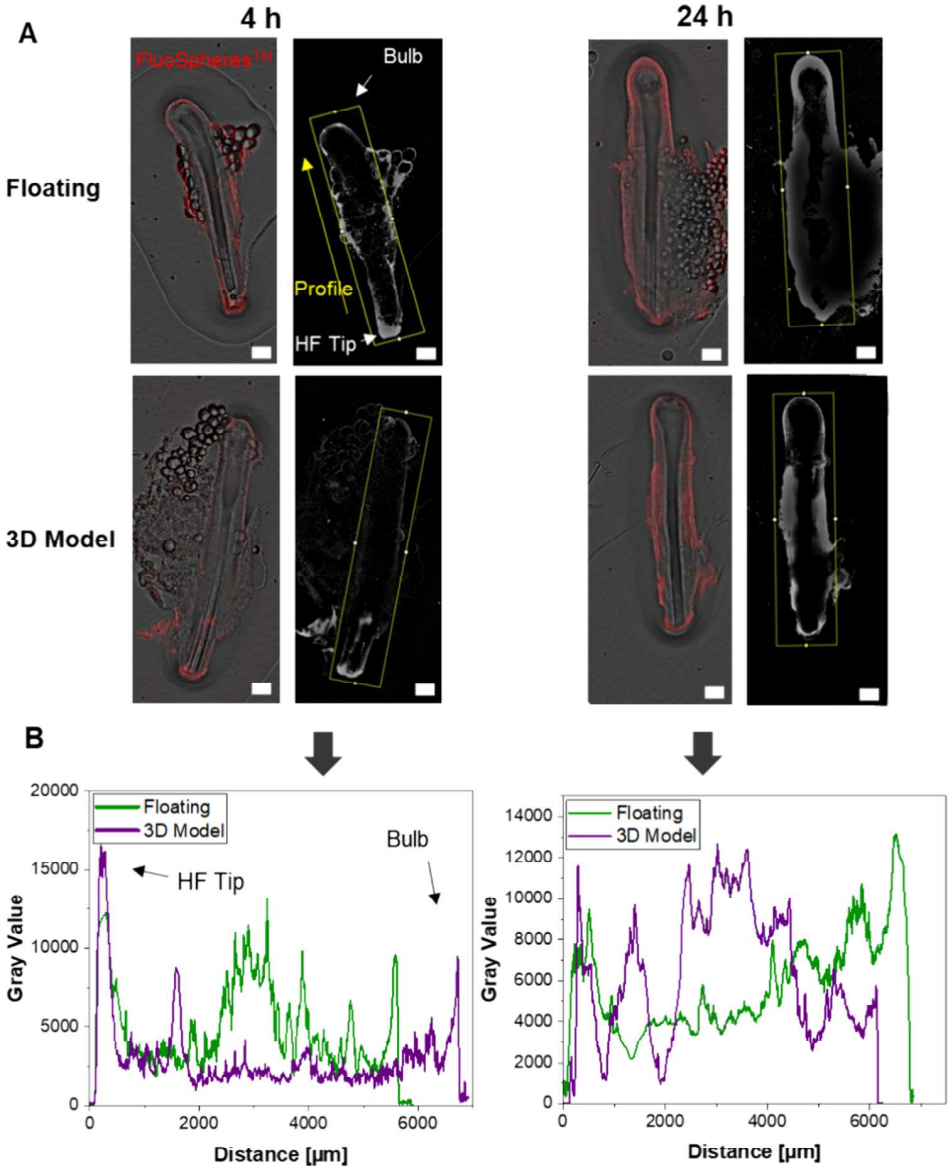


**Figure 4.** Follicular transport of FluoSpheres (200 nm). (A) Fluorescence imaging of spheres applied on top of the 3D model and floating HFs after 4 and 24 h (different HFs). The HF bulb is always upward and the HF tip is downward. The scale bars equal 100 $\mu$m. (B) Intensity profile of HFs after 4 and 24 h.

7 days, maintaining a healthy anagen morphology until day 7 (Figure 2C,D). On approximately day 7, we observed a change in the HF cycle, as evidenced by the detachment of the hair fiber from the papillae.

**3.2. 3D Printed Hair Follicle Model.** To replicate the growth behavior within a 3D matrix, we designed a model that includes a PCL scaffold and a medium channel at the level of the HFs' bulbs (Figures 1A and 3A). In preliminary experiments, we embedded HFs in collagen on commercially available Transwells but observed insufficient growth, probably due to poor nutrition supply. Therefore, we aimed to design a direct supply and optimized control via 3D printing. The increase of hair length in the 3D model closely resembled that of the floating HFs (Figure 3B,C). Due to limited availability of skin tissues, only one HF was used per model (instead of three). Daily growth images in the 3D model are provided in Figure S1. Hair fiber detachment occurred around day 7, indicating the success of the 3D culture within the surrounding matrix.

**3.3. Follicular Transport.** As described previously, nanocarriers in the submicrometer range show some accumulation in human HFs *in vivo*. Thus, we must postulate that this phenomenon should also be observed in a suitable *in vitro* model. For that, we assessed follicular transport using 200 nm fluorescent spheres. These spheres were applied to both the 3D model and floating HFs for 4 and 24 h (different HFs) (Figure 4A). Fluorescence imaging revealed that nanoparticles began to accumulate around the entire HF after just 4 h when the HFs were floating. In the 3D model, nanoparticles primarily gathered at the tip of the HF, suggesting that HF penetration occurs under such conditions, indeed, at least in most of the follicles. After 24 h, the 3D model exhibited deeper follicular penetration of nanoparticles, especially around the HFs, with some even detected inside the HF's inner sheath as observed through fluorescence imaging. Additional replicates


https://doi.org/10.1021/acsbiomaterials.4c00570
ACS Biomater. Sci. Eng. 2024, 10, 4947−4957

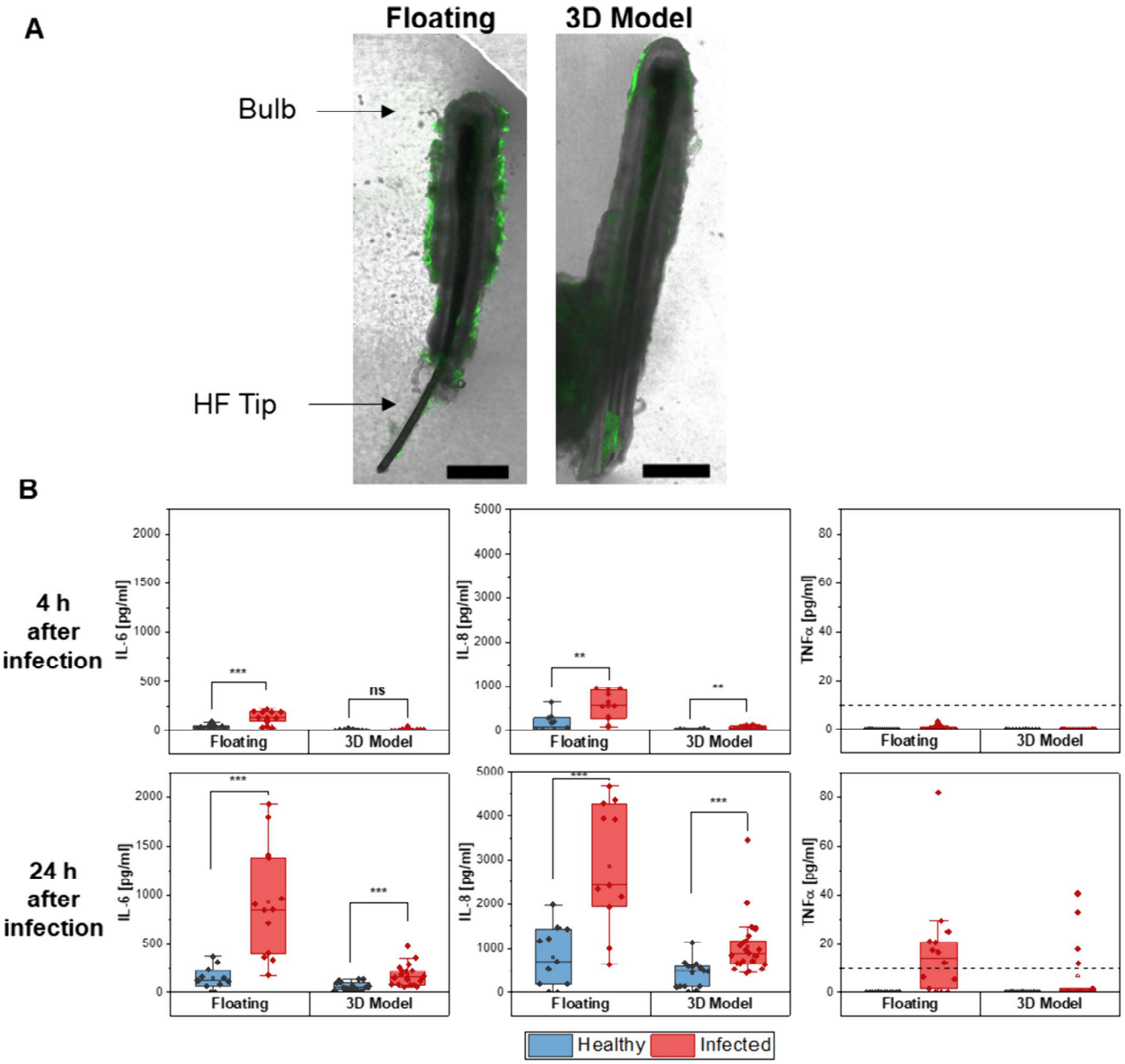


**Figure 5.** *S. aureus* infection of HF cultures. (A) Infection profile of HFs from both culture approaches via the GFP signal of bacteria. The scale bar equals 500 $\mu$m. (B) Cytokine release 2 and 4 h postinfection with $N = 5-8$ and $n = 11-22$ models (each with 3 HFs). Two-sample *t*-tests were performed for each condition; $^{**}p < 0.01$, $^{***}p < 0.001$. Error bars indicate standard deviation.

are displayed in Figure S2. Intensity profiles were generated from the gray value images, focusing on a region of interest within the yellow rectangle for HFs of similar size (Figure 4B). These profiles provide further insights, revealing a decrease in the gray value with an increasing distance from the hair tip in the 3D model, while the floating HFs exhibited a more consistent distribution over the entire follicle. After 24 h, the gray value remained higher over a longer distance before decreasing at the bulb level of the HF.

**3.4. Hair Follicle Infection with *S. aureus*.** To establish an infection model, we subjected the HFs to drop infection with *S. aureus* (Newman GFP). CLSM images taken after 24 h revealed that bacteria colonize the outer tissue surfaces, while some of the bacteria also appeared to enter the openings of the HF. This was, however, observed under floating conditions as well as in the 3D model (Figure 5A). As a measure of the HFs' condition at 4 and 24 h postinfection, we assessed cytokine release, including IL-6, IL-8, and TNF$\alpha$, using cytometric bead arrays in the surrounding medium. To determine the base level of cytokine release, noninfected HFs from the floating culture and the 3D model were also analyzed. After 4 h, a significant difference was already evident between the infected and noninfected conditions in the floating HFs, particularly for IL-6 and IL-8 (Figure 5B). In the 3D model, a slight but significant increase of IL-8 was observed. However, a baseline level of IL-6 and IL-8 release was already present in the noninfected conditions, indicating a stress response in the HFs, possibly due to the rigorous isolation procedure. At this time point, no TNF$\alpha$ was detected, likely due to the absence of immune cells postisolation. After 24 h, a strong, significant


https://doi.org/10.1021/acsbiomaterials.4c00570
ACS Biomater. Sci. Eng. 2024, 10, 4947−4957

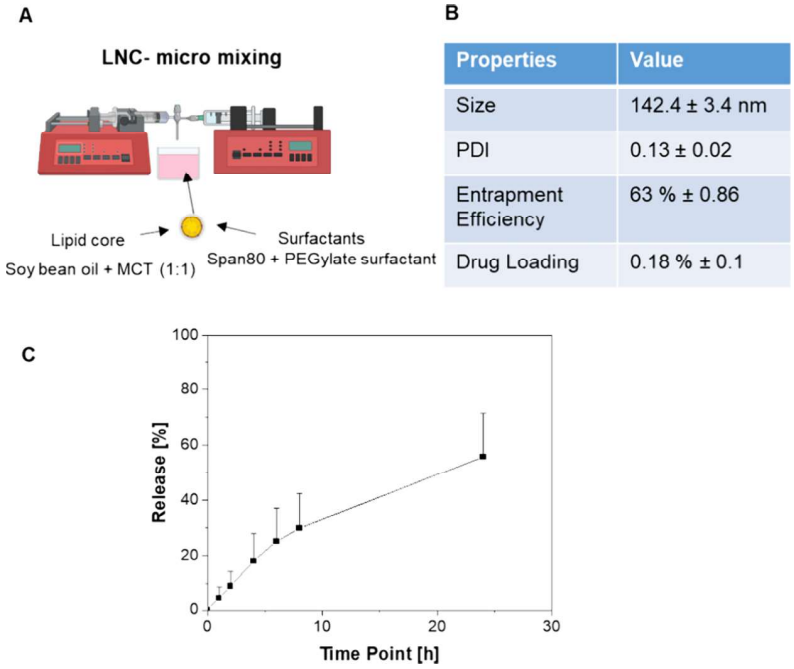


**Figure 6.** Characterization of LNCs. (A) Scheme of the micromixing process for LNC preparation. (B) Properties of LNCs with $n = 12$ for size and PDI and $n = 3$ for EE + DL. (C) Rifampicin release dynamics over 24 h, with $n = 9$.

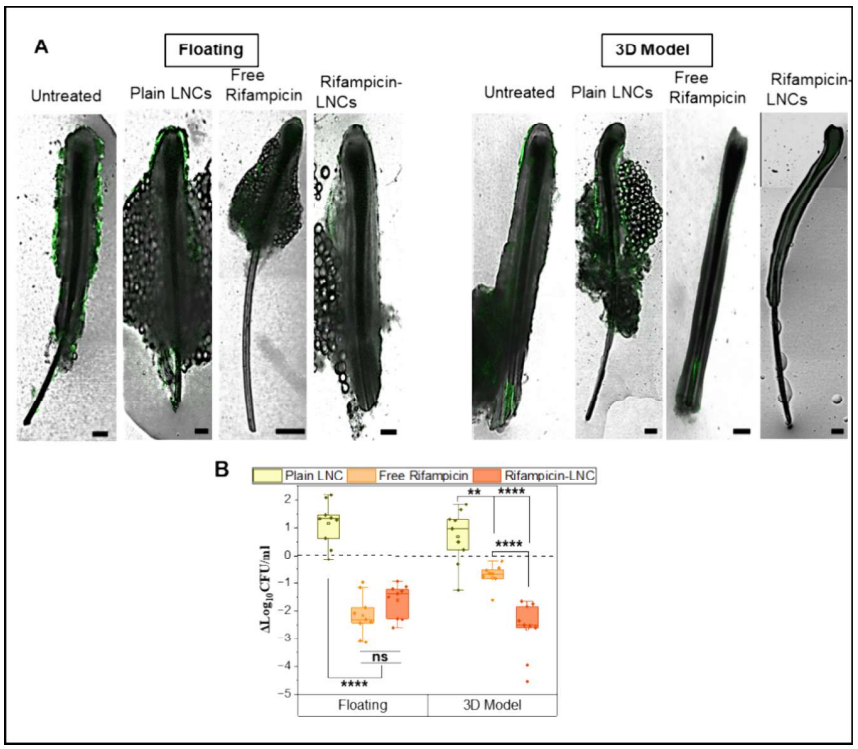


**Figure 7.** Rifampicin-loaded LNC treatment of infected HFs. (A) CLSM images of treated HFs via the GFP signal. Scale bars equal 200 $\mu$m. (B) Quantification of treatment via colony-forming units per mL of bacteria with $N = 3$; $n = 9$. Single-factor ANOVA with Tukey's multiple comparisons was performed; $^{**}p < 0.01$, $^{****}p < 0.0001$. Error bars indicate standard deviation.

difference in IL-6 and IL-8 release was observed between the infected and noninfected HFs, suggesting that the bacteria induced an elevated cytokine release from the cells. Similar findings were observed in the 3D model, although with a lower overall release. Once again, TNF$\alpha$ was not significantly detected.

**3.5. Rifampicin-Loaded Lipid Nanocapsules.** LNCs were prepared via micromixing and subsequently characterized (Figure 6A). The LNCs exhibited a size of 142.4 ± 3.4 nm (Figure 6B), with a PDI of 0.13 ± 0.02. The determined EE was at 63% ± 0.86 and the DL at 0.18% ± 0.001. The release of rifampicin was about 60% of the drug load after 24 h (Figure


https://doi.org/10.1021/acsbiomaterials.4c00570
ACS Biomater. Sci. Eng. 2024, 10, 4947−4957

6C), corresponding to a release rate of 3−4 μg/mL. The working concentration of 5 mg/mL exhibited no cytotoxic effects on HaCaT cells (Figure S3). More details can be found in the Supporting Information. HaCaT cells were chosen as the cell line for this study due to the significant presence of keratinocytes in HFs.[25]

### 3.6. Treatment of Hair Follicles with Rifampicin LNCs.

The goal was to investigate whether the 3D model would be able to demonstrate a difference in antimicrobial activity when an antibiotic was delivered to the HF by some nanocarrier rather than in the free (i.e., molecularly dispersed) form. Therefore, we applied rifampicin-loaded LNCs to both the 3D and conventional culture infection models. Plain LNCs and free rifampicin (concentration adjusted to release from LNCs) served as control groups. Three HFs were used per 3D model, while analogous experiments were also conducted on HFs in conventional floating culture. CLSM images, showing the location and indicating the amount of GFP-expressing *S. aureus*, revealed no observable impact from the plain LNCs vs the untreated infection sample (Figure 7A). In the floating culture, a reduced GFP signal was observed when the free drug was administered, but no difference was observed when the rifampicin LNCs were used. A similar pattern was observed in the 3D model, but the images showed a slightly enhanced reduction in GFP when rifampicin was delivered by LNCs. To assess such differences in efficacy more quantitatively, the change in bacterial colony-forming units per milliliter (ΔCFU/mL) was determined (Figure 7B). As expected, plain LNCs had no discernible effect on the bacteria. In the floating culture, there was no significant difference observed between free rifampicin and rifampicin-loaded LNCs. Only in the 3D model, however, rifampicin-loaded LNCs demonstrated significantly stronger effectiveness compared to the free drug. These results suggest a crucial role of the 3D environment, obviously reflecting the follicular penetration of the nanocarrier, which cannot be observed with the free drug or with the conventional floating culture.

## 4. DISCUSSION

Here, we report an innovative approach for culturing HFs within a 3D printed model to evaluate the effectiveness of nanoantibiotics against bacterial infections. Apart from a general lack of *in vitro* models addressing bacterial infections in HFs, the conventional HF cultures with floating follicles are not suitable for assessing the improved efficacy of anti-infective agents when delivered by nanocarriers. With our approach, we aimed to overcome these limitations. Initially, we conducted experiments using floating HFs to confirm the feasibility of culturing HFs after their isolation. When cultured over the course of 7 days *ex vivo*, the HFs exhibited a healthy anagen morphology. However, on the seventh day, we observed a change in the HF cycle, with the hair fibers detaching from the bulb. It is noteworthy that similar outcomes were previously documented by Philpott et al. in 1990, as well as by Khidhir et al. in 2013, and several other research groups.[9,26−28] Subsequently, we cultured the HFs in a perpendicular orientation within a 3D printed model embedded in a collagen matrix. This approach yielded similar hair growth behavior, confirming the success of our method.

To verify the phenomenon of follicular penetration by nanocarriers in the model, we applied commercially available FluoSpheres to both culture approaches. After 4 h, the particles accumulated on the entire follicle in the floating culture, while they gathered specially on the follicle opening in the 3D model. Internal follicular transport was observed on images, but not every time. After 24 h, the particles accumulate deeper around the HF, penetrating also the inner sheath in the 3D model. While it has been shown that the optimal size for deep follicle penetration is between 400 and 700 nm, 100−200 nm exhibits also follicular penetration and quicker accumulation.[2] Lademann et al. demonstrated that smaller particles perform more transfollicular transport, while optimal sized particles rather accumulate within the follicles.[5] A remaining limitation of the model is here the missing possibility to massage the skin substitute. Moving the HFs by massage can cause a ratchet effect, enhancing nanoparticle penetration.[5,29−31] Additionally, the HF isolation removed the upper part of the HF opening, removing an option for the particles to accumulate there as a reservoir. To solve that, HFs could possibly be isolated more gently and efficiently by using some dedicated follicular unit extraction (FUE) machines, which are also used for hair transplantations in the clinic[32] and may keep the complete HF opening intact. This would help to assess nanoparticle penetration much closer to the *in vivo* situation.

Another crucial aspect of our study was infecting the model and observing the response of the HFs. To achieve this, we inoculated the cultures with bacteria and monitored the infection using fluorescence microscopy, specifically by tracking the GFP signal. Additionally, we analyzed the release of cytokines. Our observations revealed that the bacteria colonized the entire HFs in all cultures, including the surrounding area, the outer sheath, and the HF opening. Thus far, only a limited number of studies have visualized infections within HFs. In histological sections of skin biopsies with inflamed follicles, Jahns et al. demonstrated the colonization of *S. aureus* both inside and at the opening of the HF.[33] Ten Broeke-Smits et al. confirmed that *S. aureus* has the capability to utilize HFs as colonization niches, both on the outer and inner portions of the follicles.[34] Animal experiments involving mice produced similar results, with bacteria colonizing HFs deeply through the follicle openings.[35,36] Following the infection, the HFs began to release increased amounts of cytokines, particularly IL-6 and IL-8, when compared to uninfected controls. This suggests that the HFs remain intact and respond to the infection. Keratinocytes and fibroblasts appear to be involved in this immune response.[37] Notably, we did not detect the release of TNFα, likely due to the absence of immune cells. However, when comparing the floating cultures to the 3D model, we observed higher total cytokine levels in the former. This could be attributed to the different environments in which the cultures are exposed. In the case of floating HFs, they are in direct contact with bacteria to a greater extent than the follicles within the 3D model, where bacteria are applied on top. The collagen matrix within the 3D model serves as a barrier, potentially delaying bacterial colonization. However, there is no complete blocking between the collagen and the HF, allowing the bacteria also to colonize this area. Essentially, the 3D model provides a suitable readout via cytokine release when an infection is induced. Nevertheless, the model at this stage is limited by the lack of immune cell recruiting. Also, experiments may be performed to record the cytokine release after infection or inflammation and its treatment by therapeutic nanocarriers.

To evaluate our model in some specific application of follicular targeting, we designed rifampicin-loaded LNCs at a size of 142.4 nm, coming close to the size of applied


https://doi.org/10.1021/acsbiomaterials.4c00570
ACS Biomater. Sci. Eng. 2024, 10, 4947−4957

FluoSpheres. Lipid-based nanosystems have already shown promising outcomes for follicle-targeted drug delivery applications on *ex vivo* human and porcine skin.[38−40] Recently, Angelo et al. showed enhanced follicular deposition of lipid nanocarriers of similar size.[41] While the EE and DL were not exceptionally high, they fall within an effective range. Essentially, the rifampicin release of 3−4 μg/mL after 24 h is above the minimum inhibitory concentration for *S. aureus*.[42]

As a final proof of concept, we treated the infected HF cultures with the well-known antibiotic rifampicin. In conventional floating cultures, there was no difference in efficacy between free rifampicin and rifampicin-loaded LNCs. However, in the 3D model, we observed a significant difference between the two treatments in the ΔLog10CFU/mL. The loaded LNCs appeared to be more efficient than the free drug, indeed, but were only observed in the 3D model and not on floating follicles. This difference can be attributed to the distinct environments in these two models. In the floating HFs, both the free drug and the drug-loaded LNCs can equally access the entire HF. In the 3D model, however, the LNCs have a better ability to enter the HF and penetrate the collagen, the same as it is known to occur *in vivo*, thus providing more efficient antibiotic drug delivery to the site of infection. Considering that *in vivo*, the HFs are not exposed to the drug in the same way as the floating follicles, our model obviously provides a more physiological and thus relevant approach.

Obviously, floating HF models are not very suitable for studying anti-infectives and in particular nanoantibiotics against bacterial infections, whereas the here described 3D model with implanted HFs allows to address some of these challenges and moreover allows to use human tissues. Nevertheless, this technique is not meant to entirely replace but to complement, e.g., the pig ear model, which is still suitable for visualizing and quantifying particle and drug accumulation in hair follicles. Considering the advantages of our method, this approach could be further optimized by using HFs with complete openings, possibly using "FUE machines" to better mimic the *in vivo* situation. Implementing an epidermis substitute with better mechanical properties, whether created artificially using polymers or through cellular methods, could further improve such a model by allowing also the application of massage. In the long term, increasing complexity by incorporating additional cell types such as fibroblasts and immune cells could make the model even more representative of the human situation. These aspects were already realized in modern skin equivalents.[43,44] A complex model of this nature would provide valuable insights into nanoantibiotic targeting, HF viability, and pathogen behavior, ultimately improving the predictiveness of drug efficacy and safety assessments.

## 5. CONCLUSIONS

We have pioneered a 3D HF model, utilizing state-of-the-art 3D printing technology. By embedding isolated human HFs into a collagen matrix with a nutrient channel, our model successfully showed growth behavior comparable to simple floating HF cultures. Our study elucidates the critical role of the HF culture environment for follicular transport and underscores the potential of nanoparticulate formulations for targeted drug delivery. Importantly, the 3D HF model demonstrates susceptibility to infection and exhibits a cytokine response when exposed to *S. aureus*, highlighting its physiological relevance. With its innovative design and implications for advancing healthcare materials, our approach represents a promising platform for investigating nanoantibiotics against HF infections, offering significant potential for future therapeutic developments in this domain.

## ■ ASSOCIATED CONTENT

### Data Availability Statement

The data that support the findings of this study are available upon reasonable request from the authors.

### Supporting Information

The Supporting Information is available free of charge at https://pubs.acs.org/doi/10.1021/acsbiomaterials.4c00570.

Additional experimental details including images of HF growth in a 3D model of each respective day (Figure S1), follicular transport (Figure S2), toxicity characterization of rifampicin-loaded nanocapsules on HaCaT cells via a PrestoBlue assay (Figure S3), and more technical details of the printed 3D model in Table S1 (PDF)

## ■ AUTHOR INFORMATION


### Corresponding Author

**Claus-Michael Lehr** − *Department of Drug Delivery, Helmholtz Center for Infection Research, Helmholtz-Institute for Pharmaceutical Research Saarland, Saarbrücken 66123, Germany; Saarland University, Saarbrücken 66123, Germany;* orcid.org/0000-0002-5864-8462; Email: claus-michael.lehr@helmholtz-hips.de

### Authors

**Samy Aliyazdi** − *Department of Drug Delivery, Helmholtz Center for Infection Research, Helmholtz-Institute for Pharmaceutical Research Saarland, Saarbrücken 66123, Germany; Saarland University, Saarbrücken 66123, Germany*

**Sarah Frisch** − *Department of Drug Delivery, Helmholtz Center for Infection Research, Helmholtz-Institute for Pharmaceutical Research Saarland, Saarbrücken 66123, Germany; Saarland University, Saarbrücken 66123, Germany*

**Tobias Neu** − *Department of Drug Delivery, Helmholtz Center for Infection Research, Helmholtz-Institute for Pharmaceutical Research Saarland, Saarbrücken 66123, Germany; Saarland University, Saarbrücken 66123, Germany*

**Barbara Veldung** − *Specialist in Plastic and Aesthetic Surgery, Saarbrücken 66111, Germany*

**Pankaj Karande** − *Chemical and Biological Engineering, Rensselaer Polytechnic Institute, Troy, New York 12180, United States*

**Ulrich F Schaefer** − *Saarland University, Saarbrücken 66123, Germany*

**Brigitta Loretz** − *Department of Drug Delivery, Helmholtz Center for Infection Research, Helmholtz-Institute for Pharmaceutical Research Saarland, Saarbrücken 66123, Germany*

**Thomas Vogt** − *Clinic for Dermatology, University Clinic Homburg, Homburg 66424, Germany*

Complete contact information is available at: https://pubs.acs.org/10.1021/acsbiomaterials.4c00570

### Author Contributions

[#]S.A. and S.F. contributed equally. S.A., S.F., C.-M.L., B.L., U.F.S., T.V., and P.K. performed conceptualization; S.A., S.F., and T.N. performed data curation; C.-M.L., B.L., U.F.S., and T.V. performed supervision; B.V. and P.K. performed resources acquisition; S.A. performed writing of the original draft; S.A., S.F., C.-M.L., B.L., U.F.S., T.V., T.N., B.V., and P.K. performed review and editing of the mannuscript. The manuscript was written through contributions of all authors. All authors have given approval to the final version of the manuscript.

### Notes

The authors declare no competing financial interest.
Ethical approval (BU/170/20 Ethikkommission Ärztekammer des Saarlandes) and patient consent were obtained for all human tissues used in this study.

## ■ ACKNOWLEDGMENTS

Pascal Paul and Clémentine Richter are thanked for technical support. Judith Emminghaus is thanked for coordinating skin tissue donation from patients. All schemes were created using www.biorender.com.

## ■ ABBREVIATIONS

HF:hair follicle; PLGA:poly(DL-lactide-*co*-glycolide); PCL:polycaprolactone; LNCs:lipid nanocapsules; PBS:phosphate-buffered saline; IL-6:interleukin 6; IL-8:interleukin 8; EE:entrapment efficiency; DL:drug loading; FUE:follicular unit extraction

## ■ REFERENCES

(1) Lademann, J.; Richter, H.; Schaefer, U. F.; Blume-Peytavi, U.; Teichmann, A.; Otberg, N.; Sterry, W. Hair follicles - a long-term reservoir for drug delivery. *Skin pharmacology and physiology* **2006**, *19* (4), 232−236.

(2) Gu, Y.; Bian, Q.; Zhou, Y.; Huang, Q.; Gao, J. Hair follicle-targeting drug delivery strategies for the management of hair follicle-associated disorders. *Asian journal of pharmaceutical sciences* **2022**, *17* (3), 333−352.

(3) Pelikh, O.; Eckert, R. W.; Pinnapireddy, S. R.; Keck, C. M. Hair follicle targeting with curcumin nanocrystals: Influence of the formulation properties on the penetration efficacy. *Journal of controlled release: official journal of the Controlled Release Society* **2021**, *329*, 598−613.

(4) Krishnan, V.; Mitragotri, S. Nanoparticles for topical drug delivery: Potential for skin cancer treatment. *Advanced drug delivery reviews* **2020**, *153*, 87−108.

(5) Lademann, J.; Richter, H.; Teichmann, A.; Otberg, N.; Blume-Peytavi, U.; Luengo, J.; Weiß, B.; Schaefer, U. F.; Lehr, C. M.; Wepf, R. Nanoparticles–an efficient carrier for drug delivery into the hair follicles. *Eur. J. Pharm. Biopharm.* **2007**, *66* (2), 159−164.

(6) Raber, A. S.; Mittal, A.; Schäfer, J.; Bakowsky, U.; Reichrath, J.; Vogt, T.; Schaefer, U. F.; Hansen, S.; Lehr, C.-M. Quantification of nanoparticle uptake into hair follicles in pig ear and human forearm. *Journal of controlled release: official journal of the Controlled Release Society* **2014**, *179*, 25−32.

(7) Zambrano, A.; Klein, A. L.; Patzelt, A. Analysis of the morphometric parameters of pig ear hair follicles. *Skin research and technology: official journal of International Society for Bioengineering and the Skin (ISBS) [and] International Society for Digital Imaging of Skin (ISDIS) [and] International Society for Skin Imaging (ISSI)* **2021**, *27* (5), 730−738.

(8) Christmann, R.; Thomas, C.; Jager, N.; Raber, A. S.; Loretz, B.; Schaefer, U. F.; Tschernig, T.; Vogt, T.; Lehr, C.-M. Nanoparticle Targeting to Scalp Hair Follicles: New Perspectives for a Topical Therapy for Alopecia Areata. *J. Invest. Dermatol.* **2020**, *140* (1), 243−246.e5.

(9) Philpott, M. P.; Green, M. R.; Kealey, T. Human hair growth in vitro. *J. Cell Sci.* **1990**, *97* (Pt 3), 463−471.

(10) Langan, E. A.; Philpott, M. P.; Kloepper, J. E.; Paus, R. Human hair follicle organ culture: theory, application and perspectives. *Experimental dermatology* **2015**, *24* (12), 903−911.

(11) Abaci, H. E.; Coffman, A.; Doucet, Y.; Chen, J.; Jacków, J.; Wang, E.; Guo, Z.; Shin, J. U.; Jahoda, C. A.; Christiano, A. M. Tissue engineering of human hair follicles using a biomimetic developmental approach. *Nat. Commun.* **2018**, *9* (1), 5301.

(12) Otberg, N.; Kang, H.; Alzolibani, A. A.; Shapiro, J. Folliculitis decalvans. *Dermatologic therapy* **2008**, *21* (4), 238−244.

(13) Alessandrini, A.; Bruni, F.; Piraccini, B. M.; Starace, M. Common causes of hair loss - clinical manifestations, trichoscopy and therapy. *Journal of the European Academy of Dermatology and Venereology: JEADV* **2021**, *35* (3), 629−640.

(14) Vinkel, C.; Thomsen, S. F. Hidradenitis Suppurativa: Causes, Features, and Current Treatments. *J. Clin. aesthetic Dermatol.* **2018**, *11* (10), 17−23.

(15) Nikolakis, G.; Liakou, A. I.; Bonovas, S.; Seltmann, H.; Bonitsis, N.; Join-Lambert, O.; Wild, T.; Karagiannidis, I.; Zolke-Fischer, S.; Langner, K.; Zouboulis, C. C. Bacterial Colonization in Hidradenitis Suppurativa/Acne Inversa: A Cross-sectional Study of 50 Patients and Review of the Literature. *Acta dermato-venereologica* **2017**, *97* (4), 493−498.

(16) Alotaibi, H. M. Incidence, Risk Factors, and Prognosis of Hidradenitis Suppurativa Across the Globe: Insights from the Literature. *Clinical, cosmetic and investigational dermatology* **2023**, *16*, 545−552.

(17) Vañó-Galván, S.; Molina-Ruiz, A. M.; Fernández-Crehuet, P.; Rodrigues-Barata, A. R.; Arias-Santiago, S.; Serrano-Falcón, C.; Martorell-Calatayud, A.; Barco, D.; Pérez, B.; Serrano, S.; Requena, L.; Grimalt, R.; Paoli, J.; Jaén, P.; Camacho, F. M. Folliculitis decalvans: a multicentre review of 82 patients. *Journal of the European Academy of Dermatology and Venereology: JEADV* **2015**, *29* (9), 1750−1757.

(18) Sillani, C.; Bin, Z.; Ying, Z.; Zeming, C.; Jian, Y.; Xingqi, Z. Effective treatment of folliculitis decalvans using selected antimicrobial agents. *International journal of trichology* **2010**, *2* (1), 20−23.

(19) Orenstein, L. A. V.; Nguyen, T. V.; Damiani, G.; Sayed, C.; Jemec, G. B. E.; Hamzavi, I. Medical and Surgical Management of Hidradenitis Suppurativa: A Review of International Treatment Guidelines and Implementation in General Dermatology Practice. *Dermatology (Basel, Switzerland)* **2020**, *236* (5), 393−412.

(20) Matard, B.; Meylheuc, T.; Briandet, R.; Casin, I.; Assouly, P.; Cavelier-balloy, B.; Reygagne, P. First evidence of bacterial biofilms in the anaerobe part of scalp hair follicles: a pilot comparative study in folliculitis decalvans. *Journal of the European Academy of Dermatology and Venereology: JEADV* **2013**, *27* (7), 853−860.

(21) Asfour, L.; Trautt, E.; Harries, M. J. Folliculitis Decalvans in the Era of Antibiotic Resistance: Microbiology and Antibiotic Sensitivities in a Tertiary Hair Clinic. *International journal of trichology* **2020**, *12* (4), 193−194.

(22) Pereira, M. N.; Tolentino, S.; Pires, F. Q.; Anjos, J. L. V.; Alonso, A.; Gratieri, T.; Cunha-Filho, M.; Gelfuso, G. M. Nanostructured lipid carriers for hair follicle-targeted delivery of clindamycin and rifampicin to hidradenitis suppurativa treatment. *Colloids and surfaces. B, Biointerfaces* **2021**, *197*, No. 111448.

(23) Caverzan, J.; de Jesus, M.; Durán, N. Nanostructured Lipid Carriers Loaded with 17-α-Estradiol Accumulate into Hair Follicles. *J. Braz. Chem. Soc.* **2020**, *31*, 1345 DOI: 10.21577/0103-5053.20200018.

(24) Bastiat, G.; Pritz, C. O.; Roider, C.; Fouchet, F.; Lignières, E.; Jesacher, A.; Glueckert, R.; Ritsch-Marte, M.; Schrott-Fischer, A.; Saulnier, P.; Benoit, J.-P. A new tool to ensure the fluorescent dye labeling stability of nanocarriers: a real challenge for fluorescence imaging. *Journal of controlled release: official journal of the Controlled Release Society* **2013**, *170* (3), 334−342.



https://doi.org/10.1021/acsbiomaterials.4c00570
*ACS Biomater. Sci. Eng.* 2024, 10, 4947−4957

(25) Kiani, M. T.; Higgins, C. A.; Almquist, B. D. The Hair Follicle: An Underutilized Source of Cells and Materials for Regenerative Medicine. *ACS biomaterials science & engineering* **2018**, *4* (4), 1193−1207.
(26) Philpott, M. P.; Sanders, D. A.; Kealey, T. WHOLE HAIR FOLLICLE CULTURE. *Dermatologic Clinics* **1999**, *17* (2), 315−329.
(27) Khidhir, K. G.; Woodward, D. F.; Farjo, N. P.; Farjo, B. K.; Tang, E. S.; Wang, J. W.; Picksley, S. M.; Randall, V. A. The prostamide-related glaucoma therapy, bimatoprost, offers a novel approach for treating scalp alopecias. *FASEB journal: official publication of the Federation of American Societies for Experimental Biology* **2013**, *27* (2), 557−567.
(28) Kloepper, J. E.; Sugawara, K.; Al-Nuaimi, Y.; Gáspár, E.; van Beek, N.; Paus, R. Methods in hair research: how to objectively distinguish between anagen and catagen in human hair follicle organ culture. *Experimental dermatology* **2010**, *19* (3), 305−312.
(29) Busch, L.; Keziban, Y.; Dähne, L.; Keck, C. M.; Meinke, M. C.; Lademann, J.; Patzelt, A. The impact of skin massage frequency on the intrafollicular transport of silica nanoparticles: Validation of the ratchet effect on an ex vivo porcine skin model. *European journal of pharmaceutics and biopharmaceutics: official journal of Arbeitsgemeinschaft fur Pharmazeutische Verfahrenstechnik e.V* **2021**, *158*, 266−272.
(30) Radtke, M.; Patzelt, A.; Knorr, F.; Lademann, J.; Netz, R. R. Ratchet effect for nanoparticle transport in hair follicles. *European journal of pharmaceutics and biopharmaceutics: official journal of Arbeitsgemeinschaft fur Pharmazeutische Verfahrenstechnik e.V* **2017**, *116*, 125−130.
(31) Robertson, T. A.; Sanchez, W. Y.; Roberts, M. S. Are commercially available nanoparticles safe when applied to the skin? *Journal of biomedical nanotechnology* **2010**, *6* (5), 452−468.
(32) Dua, A.; Dua, K. Follicular unit extraction hair transplant. *Journal of cutaneous and aesthetic surgery* **2010**, *3* (2), 76−81.
(33) Jahns, A. C.; Lundskog, B.; Berg, J.; Jonsson, R.; McDowell, A.; Patrick, S.; Golovleva, I.; Palmer, R. H.; Alexeyev, O. A. Microbiology of folliculitis: a histological study of 39 cases. *APMIS: acta pathologica, microbiologica, et immunologica Scandinavica* **2014**, *122* (1), 25−32.
(34) ten Broeke-Smits, N. J. P.; Kummer, J. A.; Bleys, R. L. A. W.; Fluit, A. C.; Boel, C. H. E. Hair follicles as a niche of Staphylococcus aureus in the nose; is a more effective decolonisation strategy needed? *J. Hosp. Infect.* **2010**, *76* (3), 211−214.
(35) Nakamura, K.; Williams, M. R.; Kwiecinski, J. M.; Horswill, A. R.; Gallo, R. L. Staphylococcus aureus Enters Hair Follicles Using Triacylglycerol Lipases Preserved through the Genus Staphylococcus. *Journal of investigative dermatology* **2021**, *141* (8), 2094−2097.
(36) Onunkwo, C. C.; Hahn, B. L.; Sohnle, P. G. Clearance of experimental cutaneous Staphylococcus aureus infections in mice. *Archives of dermatological research* **2010**, *302* (5), 375−382.
(37) Rahmani, W.; Sinha, S.; Biernaskie, J. Immune modulation of hair follicle regeneration. *NPJ Regen. Med.* **2020**, *5*, 9 DOI: 10.1038/s41536-020-0095-2.
(38) Friedrich, R. B.; Kann, B.; Coradini, K.; Offerhaus, H. L.; Beck, R. C. R.; Windbergs, M. Skin penetration behavior of lipid-core nanocapsules for simultaneous delivery of resveratrol and curcumin. *European journal of pharmaceutical sciences: official journal of the European Federation for Pharmaceutical Sciences* **2015**, *78*, 204−213.
(39) Kalvodová, A.; Zbytovská, J. Lipid nanocapsules enhance the transdermal delivery of drugs regardless of their physico-chemical properties. *International journal of pharmaceutics* **2022**, *628*, No. 122264.
(40) Vidlářová, L.; Hanuš, J.; Veselý, M.; Ulbrich, P.; Štěpánek, F.; Zbytovská, J. Effect of lipid nanoparticle formulations on skin delivery of a lipophilic substance. *European journal of pharmaceutics and biopharmaceutics: official journal of Arbeitsgemeinschaft fur Pharmazeutische Verfahrenstechnik e.V* **2016**, *108*, 289−296.
(41) Angelo, T.; El-Sayed, N.; Jurisic, M.; Koenneke, A.; Gelfuso, G. M.; Cunha-Filho, M.; Taveira, S. F.; Lemor, R.; Schneider, M.; Gratieri, T. Effect of physical stimuli on hair follicle deposition of clobetasol-loaded Lipid Nanocarriers. *Sci. Rep.* **2020**, *10* (1), 176.
(42) Yang, H.; Xu, S.; Huang, K.; Xu, X.; Hu, F.; He, C.; Shu, W.; Wang, Z.; Gong, F.; Zhang, C.; Liu, Q. Anti-staphylococcus Antibiotics Interfere With the Transcription of Leucocidin ED Gene in Staphylococcus aureus Strain Newman. *Frontiers in microbiology* **2020**, *11*, 265.
(43) Stanton, D. N.; Ganguli-Indra, G.; Indra, A. K.; Karande, P.Bioengineered Efficacy Models of Skin Disease: Advances in the Last 10 Years. *Pharmaceutics***2022**, *14* (2). DOI: 319.
(44) Choi, K. Y.; Ajiteru, O.; Hong, H.; Suh, Y. J.; Sultan, M. T.; Lee, H.; Lee, J. S.; Lee, Y. J.; Lee, O. J.; Kim, S. H.; Park, C. H. A digital light processing 3D-printed artificial skin model and full-thickness wound models using silk fibroin bioink. *Acta biomaterialia* **2023**, *164*, 159−174.


https://doi.org/10.1021/acsbiomaterials.4c00570
*ACS Biomater. Sci. Eng.* 2024, 10, 4947−4957

## Acknowledgment

Ich möchte meine aufrichtige Dankbarkeit all jenen ausdrücken, die mich während meiner Dissertation unterstützt haben. Dieses Projekt hätte ohne die Unterstützung und Ermutigung vieler Menschen nicht realisiert werden können.

Ein besonderer Dank geht an meinen Betreuer und Doktorvater Prof. Dr. Claus-Michael Lehr, der mich mit seinem Fachwissen, seiner Leidenschaft und seinem Ehrgeiz inspiriert und durch alle Phasen dieser Forschungsarbeit geführt hat. Seine fachliche Kompetenz und sein Engagement haben dazu beigetragen, dass meine Dissertation auf einem soliden Fundament steht.

Auch an Dr. Brigitta Loretz geht ein besonderer Dank. Ihre Geduld, Erfahrung, Präsenz und Unterstützung zu jeder Tageszeit waren essenziell und unverzichtbar für den Erfolg dieser Arbeit. Zusätzlich möchte ich mich bei Prof. Dr. Ulrich F. Schäfer, dessen langjährige Erfahrung maßgeblich entscheidend für den Erfolg war. Nicht vergessen werde ich auch Prof. Dr. Thomas Vogt, dessen klinische Erfahrung und Ressourcen maßgebend wichtig waren.

Ein weiteres großes Dankschön geht an Sarah Frisch. Als Forschungspartnerin hat sie einen entscheidenden Beitrag für den Erfolg dieser Arbeit geleistet. Sie war nicht nur eine große fachliche Hilfe, sondern auch meine mentale Stütze.

Nicht zu vergessen auch Frau Dr. Barbara Veldung, ohne die wir kein Hautgewebe erhalten hätten, die zu dem Erfolg der Arbeit unverzichtbar war.

Mein Dank gilt auch meinen Kollegen, die stets bereit waren, Ideen zu teilen, Ratschläge zu geben und gemeinsam Herausforderungen zu überwinden. Dabei geht ein besonderer Dank an Dr. Alberto Hidalgo und Dr. Patrick Carius, deren Kompetenz und menschlicher Umgang mich entscheidend prägten. Nicht vergessen werde ich auch Dr. Lena Kliesch. Als Bürokollegin hatte sie immer ein offenes Ohr während all der Höhen und Tiefen dieses Projektes. Hervorheben möchte ich auch Pascal Paul, dessen technische Expertise einen wichtigen Einfluss auf diese Arbeit hatte.

Ein herzliches Dankeschön geht an meine Familie und Freunde, die mich mit ihrer bedingungslosen Unterstützung und ihrem Verständnis während des gesamten

Forschungsprozesses begleitet haben. Ihr Glaube an mich hat mir die nötige Motivation gegeben, auch in schwierigen Momenten nicht aufzugeben.

Abschließend möchte ich mich bei allen Personen bedanken, die indirekt zum Gelingen dieser Dissertation beigetragen haben. Jeder Beitrag, sei er groß oder klein, hat dazu beigetragen, dieses Projekt zu einem erfolgreichen Abschluss zu bringen.

## References

1. Fan, D.; Li, Y.; Wang, X.; Zhu, T.; Wang, Q.; Cai, H.; Li, W.; Tian, Y.; Liu, Z. Progressive 3D Printing Technology and Its Application in Medical Materials. *Frontiers in pharmacology* **2020,** *11*, 122. DOI: 10.3389/fphar.2020.00122.
2. Bozkurt, Y.; Karayel, E. 3D printing technology; methods, biomedical applications, future opportunities and trends. *Journal of Materials Research and Technology* **2021,** *14*, 1430–1450. DOI: 10.1016/j.jmrt.2021.07.050.
3. Iqbal, H.; Fernandes, Q.; Idoudi, S.; Basineni, R.; Billa, N. Status of Polymer Fused Deposition Modeling (FDM)-Based Three-Dimensional Printing (3DP) in the Pharmaceutical Industry. *Polymers* **2024,** *16* (3). DOI: 10.3390/polym16030386.
4. Kaza, A.; Rembalsky, J.; Roma, N.; Yellapu, V.; Delong, W.; Stawicki, S. Medical applications of stereolithography: An overview. *Int J Acad Med* **2018,** *4* (3), 252. DOI: 10.4103/IJAM.IJAM_54_18.
5. Song, Y.; Ghafari, Y.; Asefnejad, A.; Toghraie, D. An overview of selective laser sintering 3D printing technology for biomedical and sports device applications: Processes, materials, and applications. *Optics & Laser Technology* **2024,** *171*, 110459. DOI: 10.1016/j.optlastec.2023.110459.
6. Weng, T.; Zhang, W.; Xia, Y.; Wu, P.; Yang, M.; Jin, R.; Xia, S.; Wang, J.; You, C.; Han, C.; Wang, X. 3D bioprinting for skin tissue engineering: Current status and perspectives. *Journal of tissue engineering* **2021,** *12*, 20417314211028574. DOI: 10.1177/20417314211028574.
7. Huang, Y.; Zhang, X.-F.; Gao, G.; Yonezawa, T.; Cui, X. 3D bioprinting and the current applications in tissue engineering. *Biotechnology journal* **2017,** *12* (8). DOI: 10.1002/biot.201600734.
8. Xiang, Y.; Miller, K.; Guan, J.; Kiratitanaporn, W.; Tang, M.; Chen, S. 3D bioprinting of complex tissues in vitro: state-of-the-art and future perspectives. *Archives of toxicology* **2022,** *96* (3), 691–710. DOI: 10.1007/s00204-021-03212-y.
9. Noor, N.; Shapira, A.; Edri, R.; Gal, I.; Wertheim, L.; Dvir, T. 3D Printing of Personalized Thick and Perfusable Cardiac Patches and Hearts. *Advanced*

*science (Weinheim, Baden-Wurttemberg, Germany)* **2019,** *6* (11), 1900344. DOI: 10.1002/advs.201900344.

10. Mirdamadi, E.; Tashman, J. W.; Shiwarski, D. J.; Palchesko, R. N.; Feinberg, A. W. FRESH 3D Bioprinting a Full-Size Model of the Human Heart. *ACS biomaterials science & engineering* **2020,** *6* (11), 6453–6459. DOI: 10.1021/acsbiomaterials.0c01133.
11. Hiller, T.; Berg, J.; Elomaa, L.; Röhrs, V.; Ullah, I.; Schaar, K.; Dietrich, A.-C.; Al-Zeer, M. A.; Kurtz, A.; Hocke, A. C.; Hippenstiel, S.; Fechner, H.; Weinhart, M.; Kurreck, J. Generation of a 3D Liver Model Comprising Human Extracellular Matrix in an Alginate/Gelatin-Based Bioink by Extrusion Bioprinting for Infection and Transduction Studies. *International journal of molecular sciences* **2018,** *19* (10). DOI: 10.3390/ijms19103129.
12. Kang, D.; Hong, G.; An, S.; Jang, I.; Yun, W.-S.; Shim, J.-H.; Jin, S. Bioprinting of Multiscaled Hepatic Lobules within a Highly Vascularized Construct. *Small (Weinheim an der Bergstrasse, Germany)* **2020,** *16* (13), e1905505. DOI: 10.1002/smll.201905505.
13. Aveic, S.; Janßen, S.; Nasehi, R.; Seidelmann, M.; Vogt, M.; Pantile, M.; Rütten, S.; Fischer, H. A 3D printed in vitro bone model for the assessment of molecular and cellular cues in metastatic neuroblastoma. *Biomaterials science* **2021,** *9* (5), 1716–1727. DOI: 10.1039/D0BM00921K.
14. Zhang, Q.; Zhou, J.; Zhi, P.; Liu, L.; Liu, C.; Fang, A.; Zhang, Q. 3D printing method for bone tissue engineering scaffold. *Medicine in novel technology and devices* **2023,** *17*, None. DOI: 10.1016/j.medntd.2022.100205.
15. Bejoy, A. M.; Makkithaya, K. N.; Hunakunti, B. B.; Hegde, A.; Krishnamurthy, K.; Sarkar, A.; Lobo, C. F.; Keshav, D.; G, D.; S, D. D.; Mascarenhas, S.; Chakrabarti, S.; Kalepu, S. R. R. D.; Paul, B.; Mazumder, N. An insight on advances and applications of 3d bioprinting: A review. *Bioprinting* **2021,** *24*, e00176. DOI: 10.1016/j.bprint.2021.e00176.
16. Vanderburgh, J.; Sterling, J. A.; Guelcher, S. A. 3D Printing of Tissue Engineered Constructs for In Vitro Modeling of Disease Progression and Drug Screening. *Annals of biomedical engineering* **2017,** *45* (1), 164–179. DOI: 10.1007/s10439-016-1640-4.
17. Ashammakhi, N.; Ahadian, S.; Xu, C.; Montazerian, H.; Ko, H.; Nasiri, R.; Barros, N.; Khademhosseini, A. Bioinks and bioprinting technologies to make heterogeneous and biomimetic tissue constructs. *Materials today. Bio* **2019,** *1*, 100008. DOI: 10.1016/j.mtbio.2019.100008.
18. Weygant, J.; Koch, F.; Adam, K.; Tröndle, K.; Zengerle, R.; Finkenzeller, G.; Kartmann, S.; Koltay, P.; Zimmermann, S. A Drop-on-Demand Bioprinting Approach to Spatially Arrange Multiple Cell Types and Monitor Their Cell-Cell Interactions towards Vascularization Based on Endothelial Cells and Mesenchymal Stem Cells. *Cells* **2023,** *12* (4), 646. DOI: 10.3390/cells12040646.

19. Papaioannou, T. G.; Manolesou, D.; Dimakakos, E.; Tsoucalas, G.; Vavuranakis, M.; Tousoulis, D. 3D Bioprinting Methods and Techniques: Applications on Artificial Blood Vessel Fabrication. *Acta Cardiologica Sinica* **2019,** *35* (3), 284–289. DOI: 10.6515/ACS.201905_35(3).20181115A.

20. World Health Organization. Cardiovascular diseases (CVDs). https://www.who.int/health-topics/cardiovascular-diseases.

21. Guo, Y.; Pu, W. T. Cardiomyocyte Maturation: New Phase in Development. *Circulation research* **2020,** *126* (8), 1086–1106. DOI: 10.1161/CIRCRESAHA.119.315862.

22. Wang, Z.; Wang, L.; Li, T.; Liu, S.; Guo, B.; Huang, W.; Wu, Y. 3D bioprinting in cardiac tissue engineering. *Theranostics* **2021,** *11* (16), 7948–7969. DOI: 10.7150/THNO.61621.

23. Grix, T.; Ruppelt, A.; Thomas, A.; Amler, A.-K.; Noichl, B. P.; Lauster, R.; Kloke, L. Bioprinting Perfusion-Enabled Liver Equivalents for Advanced Organ-on-a-Chip Applications. *Genes* **2018,** *9* (4). DOI: 10.3390/genes9040176.

24. Gori, M.; Giannitelli, S. M.; Torre, M.; Mozetic, P.; Abbruzzese, F.; Trombetta, M.; Traversa, E.; Moroni, L.; Rainer, A. Biofabrication of Hepatic Constructs by 3D Bioprinting of a Cell-Laden Thermogel: An Effective Tool to Assess Drug-Induced Hepatotoxic Response. *Advanced healthcare materials* **2020,** *9* (21), e2001163. DOI: 10.1002/adhm.202001163.

25. Parodi, I.; Di Lisa, D.; Pastorino, L.; Scaglione, S.; Fato, M. M. 3D Bioprinting as a Powerful Technique for Recreating the Tumor Microenvironment. *Gels (Basel, Switzerland)* **2023,** *9* (6). DOI: 10.3390/gels9060482.

26. Fernando, K.; Kwang, L. G.; Lim, J. T. C.; Fong, E. L. S. Hydrogels to engineer tumor microenvironments in vitro. *Biomaterials science* **2021,** *9* (7), 2362–2383. DOI: 10.1039/D0BM01943G.

27. Neufeld, L.; Yeini, E.; Pozzi, S.; Satchi-Fainaro, R. 3D bioprinted cancer models: from basic biology to drug development. *Nature reviews. Cancer* **2022,** *22* (12), 679–692. DOI: 10.1038/s41568-022-00514-w.

28. Sztankovics, D.; Moldvai, D.; Petővári, G.; Gelencsér, R.; Krencz, I.; Raffay, R.; Dankó, T.; Sebestyén, A. 3D bioprinting and the revolution in experimental cancer model systems-A review of developing new models and experiences with in vitro 3D bioprinted breast cancer tissue-mimetic structures. *Pathology oncology research : POR* **2023,** *29*, 1610996. DOI: 10.3389/pore.2023.1610996.

29. Horváth, L.; Umehara, Y.; Jud, C.; Blank, F.; Petri-Fink, A.; Rothen-Rutishauser, B. Engineering an in vitro air-blood barrier by 3D bioprinting. *Scientific reports* **2015,** *5*, 7974. DOI: 10.1038/srep07974.

30. Da Rosa, N. N.; Appel, J. M.; Irioda, A. C.; Mogharbel, B. F.; Oliveira, N. B. de; Perussolo, M. C.; Stricker, P. E. F.; Rosa-Fernandes, L.; Marinho, C. R. F.; Carvalho, K. A. T. de. Three-Dimensional Bioprinting of an In Vitro Lung Model. *International journal of molecular sciences* **2023,** *24* (6). DOI: 10.3390/ijms24065852.

31. Berg, J.; Hiller, T.; Kissner, M. S.; Qazi, T. H.; Duda, G. N.; Hocke, A. C.; Hippenstiel, S.; Elomaa, L.; Weinhart, M.; Fahrenson, C.; Kurreck, J. Optimization of cell-laden bioinks for 3D bioprinting and efficient infection with influenza A virus. *Scientific reports* **2018,** *8* (1), 13877. DOI: 10.1038/s41598-018-31880-x.

32. Kang, M. S.; Jang, J.; Jo, H. J.; Kim, W.-H.; Kim, B.; Chun, H.-J.; Lim, D.; Han, D.-W. Advances and Innovations of 3D Bioprinting Skin. *Biomolecules* **2022,** *13* (1). DOI: 10.3390/biom13010055.

33. Yang, Y.; Xu, R.; Wang, C.; Guo, Y.; Sun, W.; Ouyang, L. Recombinant Human Collagen-Based Bioinks for the 3D Bioprinting of Full-thickness Human Skin Equivalent. *International journal of bioprinting* **2022,** *8* (4), 611. DOI: 10.18063/ijb.v8i4.611.

34. Lee, V.; Singh, G.; Trasatti, J. P.; Bjornsson, C.; Xu, X.; Tran, T. N.; Yoo, S.-S.; Dai, G.; Karande, P. Design and fabrication of human skin by three-dimensional bioprinting. *Tissue engineering. Part C, Methods* **2014,** *20* (6), 473–484. DOI: 10.1089/ten.tec.2013.0335.

35. Liu, J.; Zhou, Z.; Zhang, M.; Song, F.; Feng, C.; Liu, H. Simple and robust 3D bioprinting of full-thickness human skin tissue. *Bioengineered* **2022,** *13* (4), 10087–10097. DOI: 10.1080/21655979.2022.2063651.

36. Ramasamy, S.; Davoodi, P.; Vijayavenkataraman, S.; Teoh, J. H.; Thamizhchelvan, A. M.; Robinson, K. S.; Wu, B.; Fuh, J. Y.; DiColandrea, T.; Zhao, H.; Lane, E. B.; Wang, C.-H. Optimized construction of a full thickness human skin equivalent using 3D bioprinting and a PCL/collagen dermal scaffold. *Bioprinting* **2021,** *21*, e00123. DOI: 10.1016/j.bprint.2020.e00123.

37. Kim, B. S.; Lee, J.-S.; Gao, G.; Cho, D.-W. Direct 3D cell-printing of human skin with functional transwell system. *Biofabrication* **2017,** *9* (2), 25034. DOI: 10.1088/1758-5090/aa71c8.

38. Abaci, H. E.; Coffman, A.; Doucet, Y.; Chen, J.; Jacków, J.; Wang, E.; Guo, Z.; Shin, J. U.; Jahoda, C. A.; Christiano, A. M. Tissue engineering of human hair follicles using a biomimetic developmental approach. *Nature communications* **2018,** *9* (1), 5301. DOI: 10.1038/s41467-018-07579-y.

39. Motter Catarino, C.; Cigaran Schuck, D.; Dechiario, L.; Karande, P. Incorporation of hair follicles in 3D bioprinted models of human skin. *Science advances* **2023,** *9* (41), eadg0297. DOI: 10.1126/sciadv.adg0297.

40. Kyle, S. 3D Printing of Bacteria: The Next Frontier in Biofabrication. *Trends in biotechnology* **2018,** *36* (4), 340–341. DOI: 10.1016/j.tibtech.2018.01.010.

41. Schaffner, M.; Rühs, P. A.; Coulter, F.; Kilcher, S.; Studart, A. R. 3D printing of bacteria into functional complex materials. *Science advances* **2017,** *3* (12), eaao6804. DOI: 10.1126/sciadv.aao6804.

42. Spiesz, E. M.; Yu, K.; Lehner, B. A. E.; Schmieden, D. T.; Aubin-Tam, M.-E.; Meyer, A. S. Three-dimensional Patterning of Engineered Biofilms with a Do-it-

yourself Bioprinter. *Journal of visualized experiments : JoVE* **2019,** No. 147. DOI: 10.3791/59477.

43. Balasubramanian, S.; Yu, K.; Cardenas, D. V.; Aubin-Tam, M.-E.; Meyer, A. S. Emergent Biological Endurance Depends on Extracellular Matrix Composition of Three-Dimensionally Printed Escherichia coli Biofilms. *ACS synthetic biology* **2021,** *10* (11), 2997–3008. DOI: 10.1021/acssynbio.1c00290.
44. Ning, E.; Turnbull, G.; Clarke, J.; Picard, F.; Riches, P.; Vendrell, M.; Graham, D.; Wark, A. W.; Faulds, K.; Shu, W. 3D bioprinting of mature bacterial biofilms for antimicrobial resistance drug testing. *Biofabrication* **2019,** *11* (4), 45018. DOI: 10.1088/1758-5090/ab37a0.
45. Brinkman, C. L.; Schmidt-Malan, S. M.; Karau, M. J.; Greenwood-Quaintance, K.; Hassett, D. J.; Mandrekar, J. N.; Patel, R. Exposure of Bacterial Biofilms to Electrical Current Leads to Cell Death Mediated in Part by Reactive Oxygen Species. *PloS one* **2016,** *11* (12), e0168595. DOI: 10.1371/journal.pone.0168595.
46. Wolcott, R. D.; Rhoads, D. D.; Bennett, M. E.; Wolcott, B. M.; Gogokhia, L.; Costerton, J. W.; Dowd, S. E. Chronic wounds and the medical biofilm paradigm. *Journal of wound care* **2010,** *19* (2), 45-6, 48-50, 52-3. DOI: 10.12968/jowc.2010.19.2.46966.
47. Gondil, V. S.; Subhadra, B. Biofilms and their role on diseases. *BMC microbiology* **2023,** *23* (1), 203. DOI: 10.1186/s12866-023-02954-2.
48. Kolpen, M.; Kragh, K. N.; Enciso, J. B.; Faurholt-Jepsen, D.; Lindegaard, B.; Egelund, G. B.; Jensen, A. V.; Ravn, P.; Mathiesen, I. H. M.; Gheorge, A. G.; Hertz, F. B.; Qvist, T.; Whiteley, M.; Jensen, P. Ø.; Bjarnsholt, T. Bacterial biofilms predominate in both acute and chronic human lung infections. *Thorax* **2022,** *77* (10), 1015–1022. DOI: 10.1136/thoraxjnl-2021-217576.
49. Sharma, D.; Misba, L.; Khan, A. U. Antibiotics versus biofilm: an emerging battleground in microbial communities. *Antimicrobial resistance and infection control* **2019,** *8*, 76. DOI: 10.1186/s13756-019-0533-3.
50. Singh, A.; Amod, A.; Pandey, P.; Bose, P.; Pingali, M. S.; Shivalkar, S.; Varadwaj, P. K.; Sahoo, A. K.; Samanta, S. K. Bacterial biofilm infections, their resistance to antibiotics therapy and current treatment strategies. *Biomedical materials (Bristol, England)* **2022,** *17* (2). DOI: 10.1088/1748-605X/ac50f6.
51. Singh, R.; Sahore, S.; Kaur, P.; Rani, A.; Ray, P. Penetration barrier contributes to bacterial biofilm-associated resistance against only select antibiotics, and exhibits genus-, strain- and antibiotic-specific differences. *Pathogens and disease* **2016,** *74* (6). DOI: 10.1093/femspd/ftw056.
52. Høiby, N.; Bjarnsholt, T.; Moser, C.; Jensen, P. Ø.; Kolpen, M.; Qvist, T.; Aanaes, K.; Pressler, T.; Skov, M.; Ciofu, O. Diagnosis of biofilm infections in cystic fibrosis patients. *APMIS : acta pathologica, microbiologica, et immunologica Scandinavica* **2017,** *125* (4), 339–343. DOI: 10.1111/apm.12689.

53. Jennings, L. K.; Dreifus, J. E.; Reichhardt, C.; Storek, K. M.; Secor, P. R.; Wozniak, D. J.; Hisert, K. B.; Parsek, M. R. Pseudomonas aeruginosa aggregates in cystic fibrosis sputum produce exopolysaccharides that likely impede current therapies. *Cell reports* **2021,** *34* (8), 108782. DOI: 10.1016/j.celrep.2021.108782.

54. Martin, I.; Waters, V.; Grasemann, H. Approaches to Targeting Bacterial Biofilms in Cystic Fibrosis Airways. *International journal of molecular sciences* **2021,** *22* (4). DOI: 10.3390/ijms22042155.

55. Guillaume, O.; Butnarasu, C.; Visentin, S.; Reimhult, E. Interplay between biofilm microenvironment and pathogenicity of Pseudomonas aeruginosa in cystic fibrosis lung chronic infection. *Biofilm* **2022,** *4*, 100089. DOI: 10.1016/j.bioflm.2022.100089.

56. Wouters, O. J.; McKee, M.; Luyten, J. Estimated Research and Development Investment Needed to Bring a New Medicine to Market, 2009-2018. *JAMA* **2020,** *323* (9), 844. DOI: 10.1001/jama.2020.1166.

57. Hoffmann, N. Animal models of chronic Pseudomonas aeruginosa lung infection in cystic fibrosis. *Drug Discovery Today: Disease Models* **2007,** *4* (3), 99–104. DOI: 10.1016/j.ddmod.2007.11.008.

58. Lebeaux, D.; Chauhan, A.; Rendueles, O.; Beloin, C. From in vitro to in vivo Models of Bacterial Biofilm-Related Infections. *Pathogens (Basel, Switzerland)* **2013,** *2* (2), 288–356. DOI: 10.3390/pathogens2020288.

59. Crivello, G.; Fracchia, L.; Ciardelli, G.; Boffito, M.; Mattu, C. In Vitro Models of Bacterial Biofilms: Innovative Tools to Improve Understanding and Treatment of Infections. *Nanomaterials (Basel, Switzerland)* **2023,** *13* (5). DOI: 10.3390/nano13050904.

60. Anderson, G. G.; Moreau-Marquis, S.; Stanton, B. A.; O'Toole, G. A. In vitro analysis of tobramycin-treated Pseudomonas aeruginosa biofilms on cystic fibrosis-derived airway epithelial cells. *Infection and immunity* **2008,** *76* (4), 1423–1433. DOI: 10.1128/iai.01373-07.

61. Woodworth, B. A.; Tamashiro, E.; Bhargave, G.; Cohen, N. A.; Palmer, J. N. An in vitro model of Pseudomonas aeruginosa biofilms on viable airway epithelial cell monolayers. *American journal of rhinology* **2008,** *22* (3), 235–238. DOI: 10.2500/ajr.2008.22.3178.

62. Bowler, L. L.; Ball, T. B.; Saward, L. L. A novel in vitro co-culture system allows the concurrent analysis of mature biofilm and planktonic bacteria with human lung epithelia. *Journal of microbiological methods* **2014,** *101*, 49–55. DOI: 10.1016/j.mimet.2014.03.018.

63. Lichtenberg, M.; Kragh, K. N.; Fritz, B.; Kirkegaard, J. B.; Tolker-Nielsen, T.; Bjarnsholt, T. Cyclic-di-GMP signaling controls metabolic activity in Pseudomonas aeruginosa. *Cell reports* **2022,** *41* (3), 111515. DOI: 10.1016/j.celrep.2022.111515.

64. Montefusco-Pereira, C. V.; Horstmann, J. C.; Ebensen, T.; Beisswenger, C.; Bals, R.; Guzmán, C. A.; Schneider-Daum, N.; Carvalho-Wodarz, C. d. S.; Lehr, C.-M. P. aeruginosa Infected 3D Co-Culture of Bronchial Epithelial Cells and Macrophages at Air-Liquid Interface for Preclinical Evaluation of Anti-Infectives. *Journal of visualized experiments : JoVE* **2020,** No. 160. DOI: 10.3791/61069.

65. Juntke, J.; Murgia, X.; Günday Türeli, N.; Türeli, A. E.; Thorn, C. R.; Schneider, M.; Schneider-Daum, N.; Souza Carvalho-Wodarz, C. de; Lehr, C.-M. Testing of aerosolized ciprofloxacin nanocarriers on cystic fibrosis airway cells infected with P. aeruginosa biofilms. *Drug delivery and translational research* **2021,** *11* (4), 1752–1765. DOI: 10.1007/s13346-021-01002-8.

66. Horstmann, J. C.; Laric, A.; Boese, A.; Yildiz, D.; Röhrig, T.; Empting, M.; Frank, N.; Krug, D.; Müller, R.; Schneider-Daum, N.; Souza Carvalho-Wodarz, C. de; Lehr, C.-M. Transferring Microclusters of P. aeruginosa Biofilms to the Air-Liquid Interface of Bronchial Epithelial Cells for Repeated Deposition of Aerosolized Tobramycin. *ACS infectious diseases* **2022,** *8* (1), 137–149. DOI: 10.1021/acsinfecdis.1c00444.

67. Xue, Y.; Zhou, J.; Xu, B.-N.; Li, Y.; Bao, W.; Cheng, X. L.; He, Y.; Xu, C. P.; Ren, J.; Zheng, Y. R.; Jia, C. Y. Global Burden of Bacterial Skin Diseases: A Systematic Analysis Combined With Sociodemographic Index, 1990-2019. *Frontiers in medicine* **2022,** *9*, 861115. DOI: 10.3389/fmed.2022.861115.

68. Otberg, N.; Kang, H.; Alzolibani, A. A.; Shapiro, J. Folliculitis decalvans. *Dermatologic therapy* **2008,** *21* (4), 238–244. DOI: 10.1111/j.1529-8019.2008.00204.x.

69. Alessandrini, A.; Bruni, F.; Piraccini, B. M.; Starace, M. Common causes of hair loss - clinical manifestations, trichoscopy and therapy. *Journal of the European Academy of Dermatology and Venereology : JEADV* **2021,** *35* (3), 629–640. DOI: 10.1111/jdv.17079.

70. Vinkel, C.; Thomsen, S. F. Hidradenitis Suppurativa: Causes, Features, and Current Treatments. *The Journal of clinical and aesthetic dermatology* **2018,** *11* (10), 17–23. DOI:

71. Montero-Vilchez, T.; Diaz-Calvillo, P.; Rodriguez-Pozo, J.-A.; Cuenca-Barrales, C.; Martinez-Lopez, A.; Arias-Santiago, S.; Molina-Leyva, A. The Burden of Hidradenitis Suppurativa Signs and Symptoms in Quality of Life: Systematic Review and Meta-Analysis. *International journal of environmental research and public health* **2021,** *18* (13). DOI: 10.3390/ijerph18136709.

72. Phan, K.; Charlton, O.; Smith, S. D. Global prevalence of hidradenitis suppurativa and geographical variation—systematic review and meta-analysis. *biomed dermatol* **2020,** *4* (1). DOI: 10.1186/s41702-019-0052-0.

73. Nikolakis, G.; Liakou, A. I.; Bonovas, S.; Seltmann, H.; Bonitsis, N.; Join-Lambert, O.; Wild, T.; Karagiannidis, I.; Zolke-Fischer, S.; Langner, K.; Zouboulis, C. C. Bacterial Colonization in Hidradenitis Suppurativa/Acne Inversa: A Cross-sectional Study of 50 Patients and Review of the Literature. *Acta dermato-venereologica* **2017,** *97* (4), 493–498. DOI: 10.2340/00015555-2591.

74. Alotaibi, H. M. Incidence, Risk Factors, and Prognosis of Hidradenitis Suppurativa Across the Globe: Insights from the Literature. *Clinical, cosmetic and investigational dermatology* **2023,** *16*, 545–552. DOI: 10.2147/CCID.S402453.

75. Vañó-Galván, S.; Molina-Ruiz, A. M.; Fernández-Crehuet, P.; Rodrigues-Barata, A. R.; Arias-Santiago, S.; Serrano-Falcón, C.; Martorell-Calatayud, A.; Barco, D.; Pérez, B.; Serrano, S.; Requena, L.; Grimalt, R.; Paoli, J.; Jaén, P.; Camacho, F. M. Folliculitis decalvans: a multicentre review of 82 patients. *Journal of the European Academy of Dermatology and Venereology : JEADV* **2015,** *29* (9), 1750–1757. DOI: 10.1111/jdv.12993.

76. Sillani, C.; Bin, Z.; Ying, Z.; Zeming, C.; Jian, Y.; Xingqi, Z. Effective treatment of folliculitis decalvans using selected antimicrobial agents. *International journal of trichology* **2010,** *2* (1), 20–23. DOI: 10.4103/0974-7753.66908.

77. Orenstein, L. A. V.; Nguyen, T. V.; Damiani, G.; Sayed, C.; Jemec, G. B. E.; Hamzavi, I. Medical and Surgical Management of Hidradenitis Suppurativa: A Review of International Treatment Guidelines and Implementation in General Dermatology Practice. *Dermatology (Basel, Switzerland)* **2020,** *236* (5), 393–412. DOI: 10.1159/000507323.

78. Matard, B.; Meylheuc, T.; Briandet, R.; Casin, I.; Assouly, P.; Cavelier-balloy, B.; Reygagne, P. First evidence of bacterial biofilms in the anaerobe part of scalp hair follicles: a pilot comparative study in folliculitis decalvans. *Journal of the European Academy of Dermatology and Venereology : JEADV* **2013,** *27* (7), 853–860. DOI: 10.1111/j.1468-3083.2012.04591.x.

79. Asfour, L.; Trautt, E.; Harries, M. J. Folliculitis Decalvans in the Era of Antibiotic Resistance: Microbiology and Antibiotic Sensitivities in a Tertiary Hair Clinic. *International journal of trichology* **2020,** *12* (4), 193–194. DOI: 10.4103/ijt.ijt_98_20.

80. Lademann, J.; Richter, H.; Schaefer, U. F.; Blume-Peytavi, U.; Teichmann, A.; Otberg, N.; Sterry, W. Hair follicles - a long-term reservoir for drug delivery. *Skin pharmacology and physiology* **2006,** *19* (4), 232–236. DOI: 10.1159/000093119.

81. Gu, Y.; Bian, Q.; Zhou, Y.; Huang, Q.; Gao, J. Hair follicle-targeting drug delivery strategies for the management of hair follicle-associated disorders. *Asian journal of pharmaceutical sciences* **2022,** *17* (3), 333–352. DOI: 10.1016/j.ajps.2022.04.003.

82. Pelikh, O.; Eckert, R. W.; Pinnapireddy, S. R.; Keck, C. M. Hair follicle targeting with curcumin nanocrystals: Influence of the formulation properties on the penetration efficacy. *Journal of controlled release : official journal of the Controlled Release Society* **2021,** *329*, 598–613. DOI: 10.1016/j.jconrel.2020.09.053.

83. Krishnan, V.; Mitragotri, S. Nanoparticles for topical drug delivery: Potential for skin cancer treatment. *Advanced drug delivery reviews* **2020,** *153*, 87–108. DOI: 10.1016/j.addr.2020.05.011.

84. Lademann, J.; Richter, H.; Teichmann, A.; Otberg, N.; Blume-Peytavi, U.; Luengo, J.; Weiss, B.; Schaefer, U. F.; Lehr, C.-M.; Wepf, R.; Sterry, W. Nanoparticles--an efficient carrier for drug delivery into the hair follicles. *European journal of pharmaceutics and biopharmaceutics : official journal of Arbeitsgemeinschaft fur Pharmazeutische Verfahrenstechnik e.V* **2007,** *66* (2), 159–164. DOI: 10.1016/j.ejpb.2006.10.019.

85. Raber, A. S.; Mittal, A.; Schäfer, J.; Bakowsky, U.; Reichrath, J.; Vogt, T.; Schaefer, U. F.; Hansen, S.; Lehr, C.-M. Quantification of nanoparticle uptake into hair follicles in pig ear and human forearm. *Journal of controlled release : official journal of the Controlled Release Society* **2014,** *179*, 25–32. DOI: 10.1016/j.jconrel.2014.01.018.

86. Zambrano, A.; Klein, A. L.; Patzelt, A. Analysis of the morphometric parameters of pig ear hair follicles. *Skin research and technology : official journal of International Society for Bioengineering and the Skin (ISBS) [and] International Society for Digital Imaging of Skin (ISDIS) [and] International Society for Skin Imaging (ISSI)* **2021,** *27* (5), 730–738. DOI: 10.1111/srt.13008.

87. Christmann, R.; Thomas, C.; Jager, N.; Raber, A. S.; Loretz, B.; Schaefer, U. F.; Tschernig, T.; Vogt, T.; Lehr, C.-M. Nanoparticle Targeting to Scalp Hair Follicles: New Perspectives for a Topical Therapy for Alopecia Areata. *The Journal of investigative dermatology* **2020,** *140* (1), 243-246.e5. DOI: 10.1016/j.jid.2019.05.028.

88. Philpott, M. P.; Green, M. R.; Kealey, T. Human hair growth in vitro. *Journal of cell science* **1990,** *97 (Pt 3)*, 463–471. DOI: 10.1242/jcs.97.3.463.

89. Langan, E. A.; Philpott, M. P.; Kloepper, J. E.; Paus, R. Human hair follicle organ culture: theory, application and perspectives. *Experimental dermatology* **2015,** *24* (12), 903–911. DOI: 10.1111/exd.12836.

90. Nasrollahzadeh, M.; Sajadi, S. M.; Sajjadi, M.; Issaabadi, Z. An Introduction to Nanotechnology. *An Introduction to Green Nanotechnology*; Interface Science and Technology; Elsevier, 2019; pp 1–27. DOI: 10.1016/B978-0-12-813586-0.00001-8.

91. Yusuf, A.; Almotairy, A. R. Z.; Henidi, H.; Alshehri, O. Y.; Aldughaim, M. S. Nanoparticles as Drug Delivery Systems: A Review of the Implication of Nanoparticles' Physicochemical Properties on Responses in Biological Systems. *Polymers* **2023,** *15* (7). DOI: 10.3390/polym15071596.

92. Cheng, X.; Xie, Q.; Sun, Y. Advances in nanomaterial-based targeted drug delivery systems. *Frontiers in bioengineering and biotechnology* **2023,** *11*, 1177151. DOI: 10.3389/fbioe.2023.1177151.

93. Di Stefano, A. Nanotechnology in Targeted Drug Delivery. *International journal of molecular sciences* **2023,** *24* (9). DOI: 10.3390/ijms24098194.

94. Berini, F.; Orlandi, V.; Gornati, R.; Bernardini, G.; Marinelli, F. Nanoantibiotics to fight multidrug resistant infections by Gram-positive bacteria: hope or reality?

*Biotechnology advances* **2022,** *57*, 107948. DOI: 10.1016/j.biotechadv.2022.107948.

95. Le, H.; Karakasyan, C.; Jouenne, T.; Le Cerf, D.; Dé, E. Application of Polymeric Nanocarriers for Enhancing the Bioavailability of Antibiotics at the Target Site and Overcoming Antimicrobial Resistance. *Applied Sciences* **2021,** *11* (22), 10695. DOI: 10.3390/app112210695.
96. Tucker, A. N.; Carlson, T. J.; Sarkar, A. Challenges in Drug Discovery for Intracellular Bacteria. *Pathogens (Basel, Switzerland)* **2021,** *10* (9). DOI: 10.3390/pathogens10091172.
97. Yılmaz, G. E.; Göktürk, I.; Ovezova, M.; Yılmaz, F.; Kılıç, S.; Denizli, A. Antimicrobial Nanomaterials: A Review. *Hygiene* **2023,** *3* (3), 269–290. DOI: 10.3390/hygiene3030020.
98. Makabenta, J. M. V.; Nabawy, A.; Li, C.-H.; Schmidt-Malan, S.; Patel, R.; Rotello, V. M. Nanomaterial-based therapeutics for antibiotic-resistant bacterial infections. *Nature reviews. Microbiology* **2021,** *19* (1), 23–36. DOI: 10.1038/s41579-020-0420-1.
99. Chakraborty, N.; Jha, D.; Roy, I.; Kumar, P.; Gaurav, S. S.; Marimuthu, K.; Ng, O.-T.; Lakshminarayanan, R.; Verma, N. K.; Gautam, H. K. Nanobiotics against antimicrobial resistance: harnessing the power of nanoscale materials and technologies. *Journal of nanobiotechnology* **2022,** *20* (1), 375. DOI: 10.1186/s12951-022-01573-9.
100. Lemire, J. A.; Harrison, J. J.; Turner, R. J. Antimicrobial activity of metals: mechanisms, molecular targets and applications. *Nature reviews. Microbiology* **2013,** *11* (6), 371–384. DOI: 10.1038/nrmicro3028.
101. Mammari, N.; Lamouroux, E.; Boudier, A.; Duval, R. E. Current Knowledge on the Oxidative-Stress-Mediated Antimicrobial Properties of Metal-Based Nanoparticles. *Microorganisms* **2022,** *10* (2). DOI: 10.3390/microorganisms10020437.
102. Zhang, Y.; Lin, S.; Fu, J.; Zhang, W.; Shu, G.; Lin, J.; Li, H.; Xu, F.; Tang, H.; Peng, G.; Zhao, L.; Chen, S.; Fu, H. Nanocarriers for combating biofilms: Advantages and challenges. *Journal of applied microbiology* **2022,** *133* (3), 1273–1287. DOI: 10.1111/jam.15640.
103. Yeh, Y.-C.; Huang, T.-H.; Yang, S.-C.; Chen, C.-C.; Fang, J.-Y. Nano-Based Drug Delivery or Targeting to Eradicate Bacteria for Infection Mitigation: A Review of Recent Advances. *Frontiers in chemistry* **2020,** *8*, 286. DOI: 10.3389/fchem.2020.00286.
104. Forier, K.; Messiaen, A.-S.; Raemdonck, K.; Nelis, H.; Smedt, S. de; Demeester, J.; Coenye, T.; Braeckmans, K. Probing the size limit for nanomedicine penetration into Burkholderia multivorans and Pseudomonas aeruginosa biofilms. *Journal of controlled release : official journal of the Controlled Release Society* **2014,** *195*, 21–28. DOI: 10.1016/j.jconrel.2014.07.061.

105. Mamun, M. M.; Sorinolu, A. J.; Munir, M.; Vejerano, E. P. Nanoantibiotics: Functions and Properties at the Nanoscale to Combat Antibiotic Resistance. *Frontiers in chemistry* **2021,** *9*, 687660. DOI: 10.3389/fchem.2021.687660.

106. Yu, Q.; Li, J.; Zhang, Y.; Wang, Y.; Liu, L.; Li, M. Inhibition of gold nanoparticles (AuNPs) on pathogenic biofilm formation and invasion to host cells. *Scientific reports* **2016,** *6*, 26667. DOI: 10.1038/srep26667.

107. Sahli, C.; Moya, S. E.; Lomas, J. S.; Gravier-Pelletier, C.; Briandet, R.; Hémadi, M. Recent advances in nanotechnology for eradicating bacterial biofilm. *Theranostics* **2022,** *12* (5), 2383–2405. DOI: 10.7150/thno.67296.

108. Cheng, X.; Pei, X.; Xie, W.; Chen, J.; Li, Y.; Wang, J.; Gao, H.; Wan, Q. pH-Triggered Size-Tunable Silver Nanoparticles: Targeted Aggregation for Effective Bacterial Infection Therapy. *Small (Weinheim an der Bergstrasse, Germany)* **2022,** *18* (22), e2200915. DOI: 10.1002/smll.202200915.

109. Gurunathan, S.; Han, J. W.; Kwon, D.-N.; Kim, J.-H. Enhanced antibacterial and anti-biofilm activities of silver nanoparticles against Gram-negative and Gram-positive bacteria. *Nanoscale research letters* **2014,** *9* (1), 373. DOI: 10.1186/1556-276X-9-373.

110. Wang, Y. Liposome as a delivery system for the treatment of biofilm-mediated infections. *Journal of applied microbiology* **2021,** *131* (6), 2626–2639. DOI: 10.1111/jam.15053.

111. Eloy, J. O.; Petrilli, R.; Trevizan, L. N. F.; Chorilli, M. Immunoliposomes: A review on functionalization strategies and targets for drug delivery. *Colloids and surfaces. B, Biointerfaces* **2017,** *159*, 454–467. DOI: 10.1016/j.colsurfb.2017.07.085.

112. Zhang, Y.; Chen, J.; Shi, L.; Ma, F. Polymeric nanoparticle-based nanovaccines for cancer immunotherapy. *Materials horizons* **2023,** *10* (2), 361–392. DOI: 10.1039/D2MH01358D.

113. Kumar, L.; Bisen, M.; Harjai, K.; Chhibber, S.; Azizov, S.; Lalhlenmawia, H.; Kumar, D. Advances in Nanotechnology for Biofilm Inhibition. *ACS omega* **2023,** *8* (24), 21391–21409. DOI: 10.1021/acsomega.3c02239.

114. Flockton, T. R.; Schnorbus, L.; Araujo, A.; Adams, J.; Hammel, M.; Perez, L. J. Inhibition of Pseudomonas aeruginosa Biofilm Formation with Surface Modified Polymeric Nanoparticles. *Pathogens (Basel, Switzerland)* **2019,** *8* (2). DOI: 10.3390/pathogens8020055.

115. Kumar, S.; Shukla, M. K.; Sharma, A. K.; Jayaprakash, G. K.; Tonk, R. K.; Chellappan, D. K.; Singh, S. K.; Dua, K.; Ahmed, F.; Bhattacharyya, S.; Kumar, D. Metal-based nanomaterials and nanocomposites as promising frontier in cancer chemotherapy. *MedComm* **2023,** *4* (2), e253. DOI: 10.1002/mco2.253.

116. Negi, A.; Kesari, K. K. Chitosan Nanoparticle Encapsulation of Antibacterial Essential Oils. *Micromachines* **2022,** *13* (8). DOI: 10.3390/mi13081265.

117. Kasza, K.; Gurnani, P.; Hardie, K. R.; Cámara, M.; Alexander, C. Challenges and solutions in polymer drug delivery for bacterial biofilm treatment: A tissue-by-

tissue account. *Advanced drug delivery reviews* **2021,** *178*, 113973. DOI: 10.1016/j.addr.2021.113973.

118. Celebioglu, A.; Umu, O. C. O.; Tekinay, T.; Uyar, T. Antibacterial electrospun nanofibers from triclosan/cyclodextrin inclusion complexes. *Colloids and surfaces. B, Biointerfaces* **2014,** *116*, 612–619. DOI: 10.1016/j.colsurfb.2013.10.029.

119. Dhumal, D.; Maron, B.; Malach, E.; Lyu, Z.; Ding, L.; Marson, D.; Laurini, E.; Tintaru, A.; Ralahy, B.; Giorgio, S.; Pricl, S.; Hayouka, Z.; Peng, L. Dynamic self-assembling supramolecular dendrimer nanosystems as potent antibacterial candidates against drug-resistant bacteria and biofilms. *Nanoscale* **2022,** *14* (26), 9286–9296. DOI: 10.1039/D2NR02305A.

120. Naik, S. S.; Anusha, G.; Leela, K. V.; Ravi, S. Promising Approaches in Drug Delivery Against Resistant Bacteria. In *Advances in Novel Formulations for Drug Delivery*; Keservani, R. K., Kesharwani, R. K., Sharma, A. K., Eds.; Wiley, 2023; pp 219–229.

121. Velusamy, P.; Su, C.-H.; Kannan, K.; Kumar, G. V.; Anbu, P.; Gopinath, S. C. B. Surface engineered iron oxide nanoparticles as efficient materials for antibiofilm application. *Biotechnology and applied biochemistry* **2022,** *69* (2), 714–725. DOI: 10.1002/bab.2146.

122. Ning, E. *Data for: "3D Bioprinting of mature bacterial biofilms for antimicrobial resistance drug testing"*, 2019.

123. Friedrich, R. B.; Kann, B.; Coradini, K.; Offerhaus, H. L.; Beck, R. C. R.; Windbergs, M. Skin penetration behavior of lipid-core nanocapsules for simultaneous delivery of resveratrol and curcumin. *European journal of pharmaceutical sciences : official journal of the European Federation for Pharmaceutical Sciences* **2015,** *78*, 204–213. DOI: 10.1016/j.ejps.2015.07.018.

124. Kalvodová, A.; Zbytovská, J. Lipid nanocapsules enhance the transdermal delivery of drugs regardless of their physico-chemical properties. *International journal of pharmaceutics* **2022,** *628*, 122264. DOI: 10.1016/j.ijpharm.2022.122264.

125. Vidlářová, L.; Hanuš, J.; Veselý, M.; Ulbrich, P.; Štěpánek, F.; Zbytovská, J. Effect of lipid nanoparticle formulations on skin delivery of a lipophilic substance. *European journal of pharmaceutics and biopharmaceutics : official journal of Arbeitsgemeinschaft fur Pharmazeutische Verfahrenstechnik e.V* **2016,** *108*, 289–296. DOI: 10.1016/j.ejpb.2016.07.016.

126. Filaire, E.; Nachat-Kappes, R.; Laporte, C.; Harmand, M.-F.; Simon, M.; Poinsot, C. Alternative in vitro models used in the main safety tests of cosmetic products and new challenges. *International journal of cosmetic science* **2022,** *44* (6), 604–613. DOI: 10.1111/ics.12803.

127. Hofmann, E.; Schwarz, A.; Fink, J.; Kamolz, L.-P.; Kotzbeck, P. Modelling the Complexity of Human Skin In Vitro. *Biomedicines* **2023,** *11* (3). DOI: 10.3390/biomedicines11030794.